Nanoscale Advances

ROYAL SOCIETY OF CHEMISTRY

REVIEW

View Article Online
View Journal | View Issue

Cite this: *Nanoscale Adv.*, 2023, **5**, 5214

Recent advancements in the fabrication and photocatalytic applications of graphitic carbon nitride-tungsten oxide nanocomposites

Muhammad Ikram Nabeel,[a] Dilshad Hussain, *[a] Naseer Ahmad,[a]
Muhammad Najam-ul-Haq[b] and Syed Ghulam Musharraf *[a]

Received 14th March 2023
Accepted 18th August 2023

DOI: 10.1039/d3na00159h

rsc.li/nanoscale-advances

The present review focuses on the widely used graphitic carbon nitride (g-C_3N_4)-tungsten oxide (WO_3) nanocomposite in photocatalytic applications. These catalysts are widely employed due to their easy preparation, high physicochemical stability, nontoxicity, electron-rich properties, electronic band structure, chemical stability, low cost, earth-abundance, high surface area, and strong absorption capacity in the visible range. These sustainable properties make them predominantly attractive and unique from other photocatalysts. In addition, graphitic carbon nitride (g-C_3N_4) is synthesized from nitrogen-rich precursors; therefore, it is stable in strong acid solutions and has good thermal stability up to 600 °C. This review covers the historical background, crystalline phases, density-functional theory (DFT) study, synthesis method, 0-D, 1-D, 2-D, and 3-D materials, oxides/transition/nontransition metal-doped, characterization, and photocatalytic applications of WO_3/g-C_3N_4. Enhancing the catalytic performance strategies such as composite formation, element-doping, heterojunction construction, and nanostructure design are also summarized. Finally, the future perspectives and challenges for WO_3/g-C_3N_4 composite materials are discussed to motivate young researchers and scientists interested in developing environment-friendly and efficient catalysts.

Introduction

In the last few years, with the rapid growth in population, textile, pharmaceutical, food, paper, agriculture, pulp, and cosmetic industries have grown more rapidly, and the use of synthetic chemicals to fulfill the population demands have also increased considerably.[1–3] Petroleum product consumption has also increased since all these industries directly or indirectly rely on fossil fuels to produce electricity.[4] Moreover, marine oil spill pollution risk has also increased due to rapid maritime oil drilling. These petroleum hydrocarbons are toxic to marine biodiversity and indirectly affect human health.[3,5] Similarly, pharmaceuticals' active compound consumption is increasing daily, and many expired, unused, and residual drugs are discharged into the aquatic environment.[6–8] The situation has become severe, and drug residues have been detected in significant amounts in soil, wastewater, and even in drinking water globally.[9,10] Several projects worldwide are looking for strategies to limit this ecotoxicological risk of pharmaceutical products.[7,11]

Dyes and pigments are aromatic, nondegradable, toxic, and widely used in pharmaceuticals, textile industries, food colorants, cosmetics products, plastics farms, photographic film, and paper.[12,13] During the finishing and dyeing operations, approximately 0.2 million tons of dyes are released into the environment each year from textile industries.[12–14] Dye removal from water bodies is significant for the environment since a minute quantity (<1 mg L^{-1}) can be highly toxic for aquatic life, decreasing the photosynthetic activity, hindering sunlight passage, affecting the symbiotic process, and reducing water oxygenation.[15]

Since the world is facing pollution problems, several methods (ion exchange, aerobic process, membrane separation, coagulation, sorption, photocatalysis, sonolysis, ozonation, electrocatalysis, electro-Fenton, photo-Fenton, *etc.*) have been used to purify wastewater.[16,17] However, these techniques are complicated, expensive, time-consuming, and require additional operational costs.[15,18,19] Among these, advanced oxidation processes (AOPs) are fast, most favorable, ecofriendly, and efficient for effectively removing pollutants.

AOPs are chemical methods used to remove various organic and inorganic contaminants from wastewater and are employed as alternatives to conventional treatment methods (filtration or biological treatment) to meet the required water quality standards.[20] AOPs involve generating and utilizing hydroxyl radicals (·OH) by radiation in the presence of a catalyst. UV irradiation,

---

[a] *HEJ Research Institute of Chemistry, International Center for Chemical and Biological Sciences, University of Karachi, Karachi-75270, Pakistan. E-mail: dilshadhussain@iccs.edu; musharraf1977@yahoo.com*

[b] *Institute of Chemical Sciences, Bahauddin Zakariya University, Multan 60800, Pakistan*

ozone, and H_2O_2 improve advanced oxidation processes for photodegradation and nonselectively react with most organic pollutants due to the *in situ* production of highly reactive hydroxyl radicals ($\cdot$OH). The advantages of AOPs are as follows: (1) AOPs are highly effective in degrading and removing a wide range of pollutants (organic, inorganic, pesticides, pharmaceuticals, dyes, and certain types of metals). They break down these pollutants into simple compounds that are not easily treatable by other methods.[20] (2) AOPs have high oxidation potential, which allows them to oxidize and mineralize pollutants into nontoxic substances (carbon dioxide, water), promoting the complete degradation of contaminants and reducing their toxicity.[21] (3) They generate highly reactive OH radicals, which attack and breakdown a broad spectrum of dyes, drugs, and other related pollutants, making them versatile and applicable to various contaminants. Besides, they can be applied to different water sources (municipal, industrial effluents, groundwater, and contaminated surface waters).[22] (4) AOPs operate under mild conditions and achieve high treatment efficiencies in a relatively short time, which makes them suitable for practical applications.

AOPs include both homogeneous and heterogeneous photocatalysis. Fenton's reagent is a type of homogeneous photocatalyst that includes a mixture of Fe^{2+} salt (using $FeSO_4$ as an iron source) and hydrogen peroxide that produces hydroxyl radicals ($\cdot$OH) under ultraviolet (UV) irradiation (<320 nm). Heterogeneous photocatalysts include semiconductor materials such as g-C_3N_4, CdS ZnO, TiO_2, SnO_2, WO_x, Fe_2O_3, ZnS, and BiOI.[18,23,24] In heterogeneous photocatalysis, the contaminants are in a different phase (*e.g.*, dissolved in water or adsorbed on the surface) and come in contact with the photocatalyst, where the oxidation reactions occur. (1) The photocatalyst absorbs light energy and creates electron–hole pairs, generating reactive species capable of initiating oxidation reactions.[25] (2) Photocatalysis exhibits selectivity toward organic pollutants, targeting their chemical structures and functional groups, and efficiently degrading the pollutants.[26] (3) Photocatalysts are widely available and relatively inexpensive compared to other AOPs, and this accessibility makes them a practical option for water treatment.[27] (4) The optimization and customization of the process parameters are essential for photocatalysis.[28] Photocatalysis can occur at mild reaction conditions, making it energy efficient and suitable for water treatment. Factors such as the choice of catalyst, pH, temperature, light source, and contaminants' nature can influence the catalytic efficiency.

There are various photocatalysts used in AOPs. The most frequently studied materials are g-C_3N_4, TiO_2, ZnO, CdS, SnO_2, WO_x, Fe_2O_3, and ZnS. Due to the strong oxidation potential of these nanomaterials, they have a high activity of ($\cdot$OH) radical generation. Photocatalysis based on AOP involves the generation of reactive species through the interaction of a photocatalyst with light energy and reactive species, such as hydroxyl radicals (OH$\cdot$), superoxide radicals ($O_2^{\cdot-}$), and singlet oxygen ($^1O_2$), possesses high oxidation potentials, and plays a crucial role in the degradation of the pollutant. The mechanism of photocatalysis using AOP is shown in Fig. 1. The photocatalyst absorbs photons from a light source, usually ultraviolet (UV) or visible light. Electrons in the valence band (VB) gain sufficient energy for transition to the conduction band, leaving behind positively charged holes in the valence band and generating electron–hole pairs (e^-/h^+). The photogenerated electrons and holes participate in the redox reactions with adsorbed species on the surface of the photocatalyst or in the surrounding environment, and holes have a strong oxidizing power and can directly react with organic compounds, while the electrons can reduce oxidants or other species. The photogenerated h^+ reacts with water molecules adsorbed on the photocatalyst surface, producing OH radicals. These hydroxyl radicals are highly reactive and can initiate the degradation of organic pollutants. The organic compounds are broken down into smaller, less harmful molecules, such as water, carbon dioxide, and other byproducts. The electrons from the conduction band recombine with the holes from the valence band, restoring the catalyst's initial state and allowing the photocatalytic process. The drawback of photocatalysis is that the fast recombination of photogenerated electron/hole (e^-/h^+) reduces the catalytic efficiency of the catalyst and ($\cdot$OH) radical generation. Various surface modifications and structural changes have improved the activities of TiO_2, ZnO, CdS, SnO_2, WO_x, Fe_2O_3, ZnS, and BiOI-based photocatalysts.[29–35]

G-C_3N_4 has been a widely used nanocatalyst due to its easy preparation, nontoxicity, electron-rich properties, chemical stability, cost efficiency, and narrow bandgap (2.7 eV).[24,36] In addition, g-C_3N_4 can easily be synthesized from urea, thiourea, melamine, cyanamide, and dicyandiamide, and it is stable in strong acid solutions and up to 600 °C in air.[37,38] These sustainable properties of g-C_3N_4 make it predominantly elegant for solar energy utilization.[39,40] However, the limitation of pristine g-C_3N_4 is the fast recombination of photogenerated electron/hole (e^-/h^+) that reduces the photocatalytic efficiency and hydroxyl radical ($\cdot$OH) generation.[38,41] The efficiency of pristine g-C_3N_4 photocatalysts can be improved by various surface modifications and structural changes.[23,24,40,41] Similarly, the yield of g-C_3N_4 is very low. Hence, using g-C_3N_4 as the support material is preferred over using it alone.[40,42]

Metal oxide (MO_x) materials improve the photocatalytic and electronic device efficiency. The role of tungsten oxide (WO_x) is very prominent among many metal oxides.[43,44] WO_x is a semiconductor transition metal oxide with a bandgap of 2.4–2.8 eV, which can absorb the blue region of the solar spectrum; thus, it has attracted the interest of researchers due to its wide applications in several fields, such as semiconductors, solar energy devices, gas sensors, and photocatalysts.[45,46] WO_3/gC_3N_4, Ag_2WO_4@g-C_3N_4, $BaWO_4$/g-C_3N_4, WO_3/TiO_2/g-C_3N_4, g-C_3N_4/WO_3/ZnO, gC_3N_4/Bi_2WO_6, and graphene-WO_3/TiO_2 have been reported for various applications and perspective of MWO/g-C_3N_4 doped with various elements shown below in Fig. 2.[40,43,45,47–51] Combining metal WO_x and g-C_3N_4 has resulted in higher photocatalytic activity than WO_x and pure g-C_3N_4.[43] Recently, there has been significant progress in developing g-C_3N_4 and WO_3 materials due to their unique features for various applications, including photocatalytic water splitting, pollutant degradation, energy conversion, and remarkable photochemical stability.

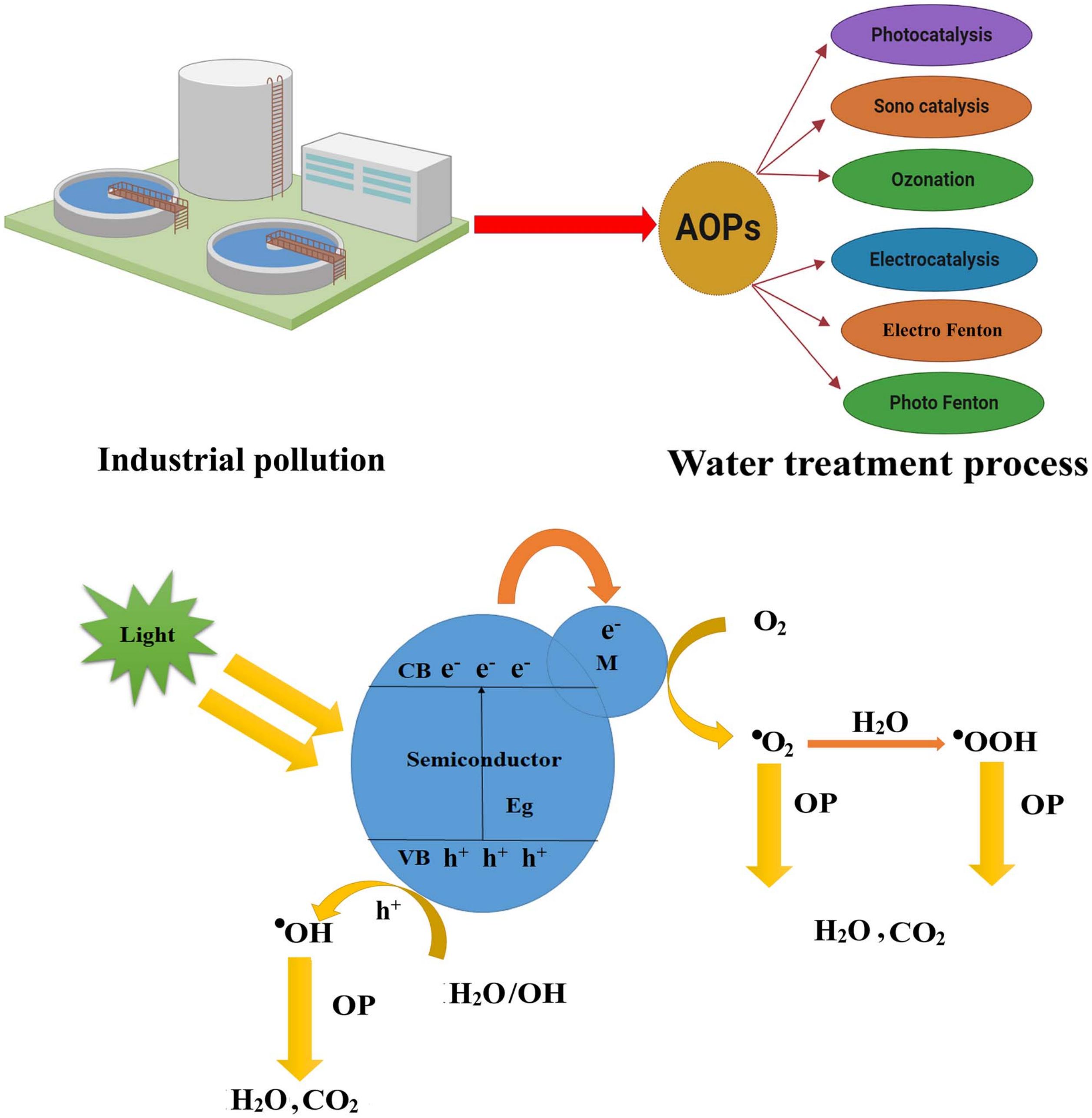

Fig. 1 The water treatment method and photocatalysis (schematic diagram of the photoredox mechanism of different water pollutants).

Tungsten trioxide has excellent photocatalytic activity in the visible light region. By integrating WO_x and g-C_3N_4, the composite can leverage the advantages of both materials, leading to enhanced photocatalytic efficiency and a broader light absorption range. Similarly, after composite formation, the bandgap reduces to 2.5 eV.

Numerous reviews exist on the synthesis, modification, and applications of g-C_3N_4 and WO_3 for photocatalysis and environmental application. For example, Jiang *et al.*[52] wrote a review on doped g-C_3N_4 for photocatalysis, including metal doping, nonmetal doping, codoping, and heterojunction formation using g-C_3N_4.[53] Similarly, WO_3-based catalysts have been reported for the photocatalytic and photoelectrocatalytic removal of organic pollutants from water.[54] This article comprehensively reviews WO_3 and focuses on its properties, various synthesis and preparation methods, and strategies to enhance its performance. Similarly, a WO_3-based photocatalyst for environmental remediation has been reported,[55] presenting a comprehensive analysis of low-cost and environment-friendly methods for the synthesis of WO_3 and investigating the correlation between morphology control and key strategies to enhance the photocatalytic performance, including elemental doping, cocatalyst hybridization, and heterojunction formation. Previous reviews focused only on either WO_3 single materials or g-C_3N_4. In this review, we briefly discuss all the graphitic carbon nitride (g-C_3N_4)-tungsten oxide (WO_3)-based nanocomposites,

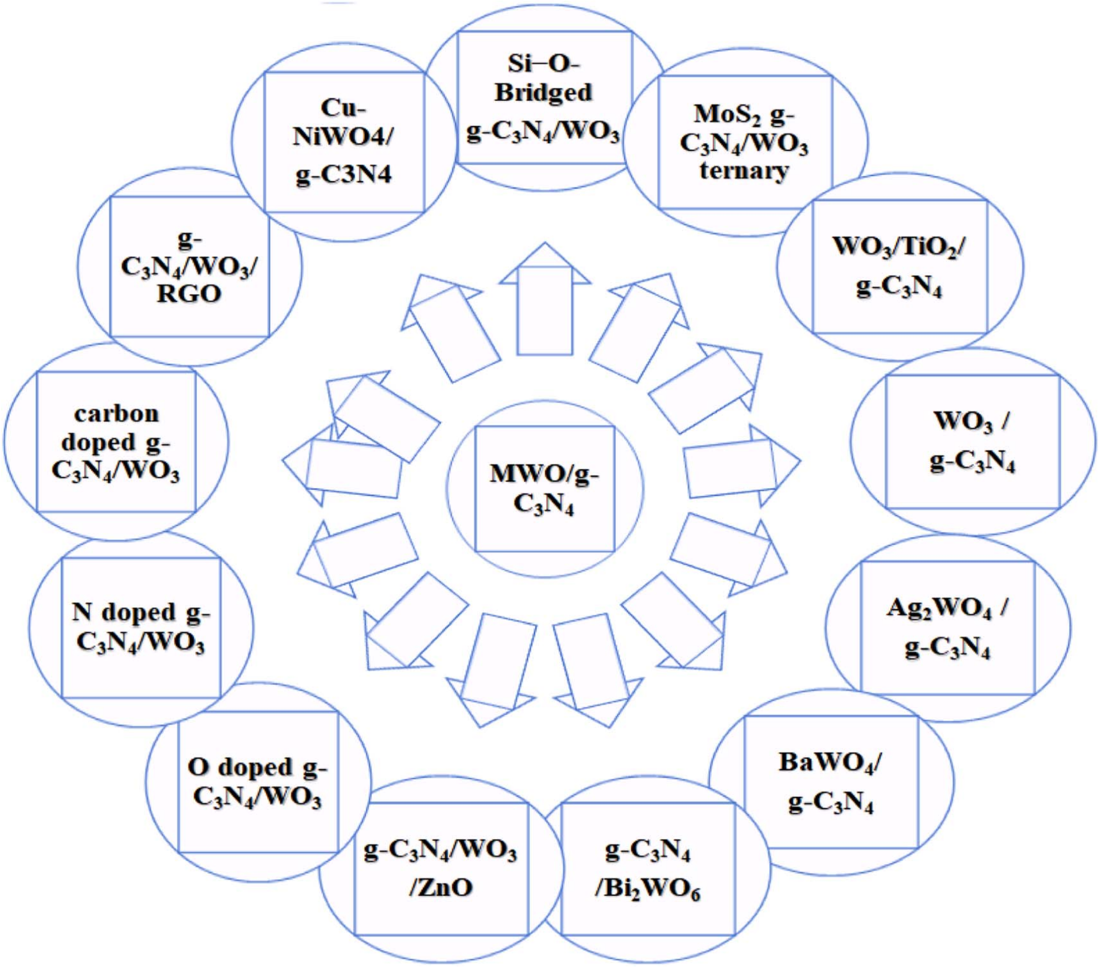

Fig. 2 Doping of MWO_x/g-C_3N_4 with various metals, nonmetals, and metalloids.

their derivatives (0D, 1D, 2D, 3D, transition metal/nonmetal doping, and ternary composite) and their photocatalytic applications. We have specifically focused on the versatile properties and rational design to precisely adjust the optical, electronic, luminescent, structural morphology, Z-scheme, and other physical properties of graphitic carbon nitride (g-C_3N_4)-tungsten oxide (WO_3)-based nanocomposite. In photocatalysis, incorporating metals, transition metals, non metals, oxides, and their codoping has shown excellent potential for bandgap engineering and nanocomposite formation, leading to enhanced light absorption and redox band potentials tailored for specific photocatalytic applications. Moreover, this review also provides a summary of recent progress in the development of efficient and cost-effective graphitic carbon nitride (g-C_3N_4)-tungsten oxide (WO_3)-based nanocomposite in photocatalysis and the removal of contaminants from the environment.

Graphitic carbon nitride-tungsten oxide composites have shown promising properties and applications in photocatalysis. However, some disadvantages are associated with their fabrication and use. Fabricating g-C_3N_4/WO_3 nanocomposites is challenging, and achieving a uniform distribution and strong interaction between WO_3 and g-C_3N_4 requires precise control over the synthesis conditions (temperature, time, precursor ratios). Large-scale synthesis with consistent properties requires complex and costly fabrication processes. The stability of g-C_3N_4/WO_3 is another concern, especially under harsh photocatalytic conditions, and can lead to aggregation during prolonged use, resulting in a decline in the photocatalytic activity over time. This review highlights the composite's physical and chemical properties, shape, DFT structure, optical bandgap, and photocatalytic properties under UV/visible light. This review also focuses on the methods for composite formation to enhance the photocatalytic properties of MWO_x/g-C_3N_4 by reducing the bandgap. Our survey shows that no previous review has been written on fabricated graphitic carbon nitride-based tungstate nanostructured materials (MWO_x/g-C_3N_4) and their photocatalytic applications. Therefore, we hope that this review will provide the researcher with ideas to construct new materials and elaborate their multifunctional applications.

Applications of WO_3/g-C_3N_4

Nanotechnology is a growing field of research due to its properties linked with small particle sizes. Many properties of nanomaterials, such as electrical, optical, and mechanical, can be explained as a function of composition, size, and structural order. The synthesis of nanostructured materials is a complicated process since a small change in the parameters can affect the properties of the end products. However, the nanostructured materials synthesized by various methods under controlled conditions have a high surface-to-volume ratio and more atoms at the grain boundary. These nanostructured materials are used for many applications such as biomedical research, engineering applications, drug delivery, cancer therapy, environment-related application, sensing (biomolecules, pesticides, gas molecules, inorganic anions, and organic molecules), and cell imaging. Nanotechnology replaced old studies and technology to improve the lifestyle and environment for life, resolving many issues and miniaturizing the devices. Tungsten oxide-based graphitic carbon nitride nanostructured materials are semiconductors synthesized by numerous methods. Doping with other materials can adjust their electrical, magnetic, and optical properties. WO_3/g-C_3N_4-based doped materials can be designed in dimensions such as 0D, 1D, 2D, and 3D. WO_3/g-C_3N_4-based pure and doped materials are multifunctional due to their inherent properties.

Below is a short view of the overall applications of doped WO_3/g-C_3N_4 (Fig. 3) and photocatalytic applications against organic pollutants.

WO_3/g-C_3N_4 materials purify air and water and efficiently degrade pollutants and harmful gases. This application can contribute to cleaner air and water resources.[56]

These materials are used in energy storage devices such as batteries, supercapacitors, and electrochemical performance. Their unique properties and high surface area make them suitable for energy storage and sensitive and selective sensing applications.[57]

These materials are also applied to produce chemicals through selective catalytic reactions. For example, the selective oxidation of alcohol into a carboxylic acid can enable environment-friendly synthesis routes throughout photocatalysis.[58]

WO_3/g-C_3N_4 make them suitable for harnessing solar energy and are utilized in solar fuel production systems (photocatalytic water splitting) to generate clean energy. These materials can also produce solar fuels such as methane, methanol, or even hydrocarbon and are used as alternatives to traditional fossil fuels.[59]

Structure of graphitic carbon nitride and its different phases

Historical background. Graphitic carbon nitride is an n-type semiconductor with a 2D conjugated polymer structure. g-C_3N_4 is an artificial oldest documented polymer reported in 1834, with the general formula of $(C_3N_3H)_n$, although typically with nonzero amounts of hydrogen. Based on the literature, carbon nitride (CN) was first studied by Berzelius and Liebig in 1834,[60]

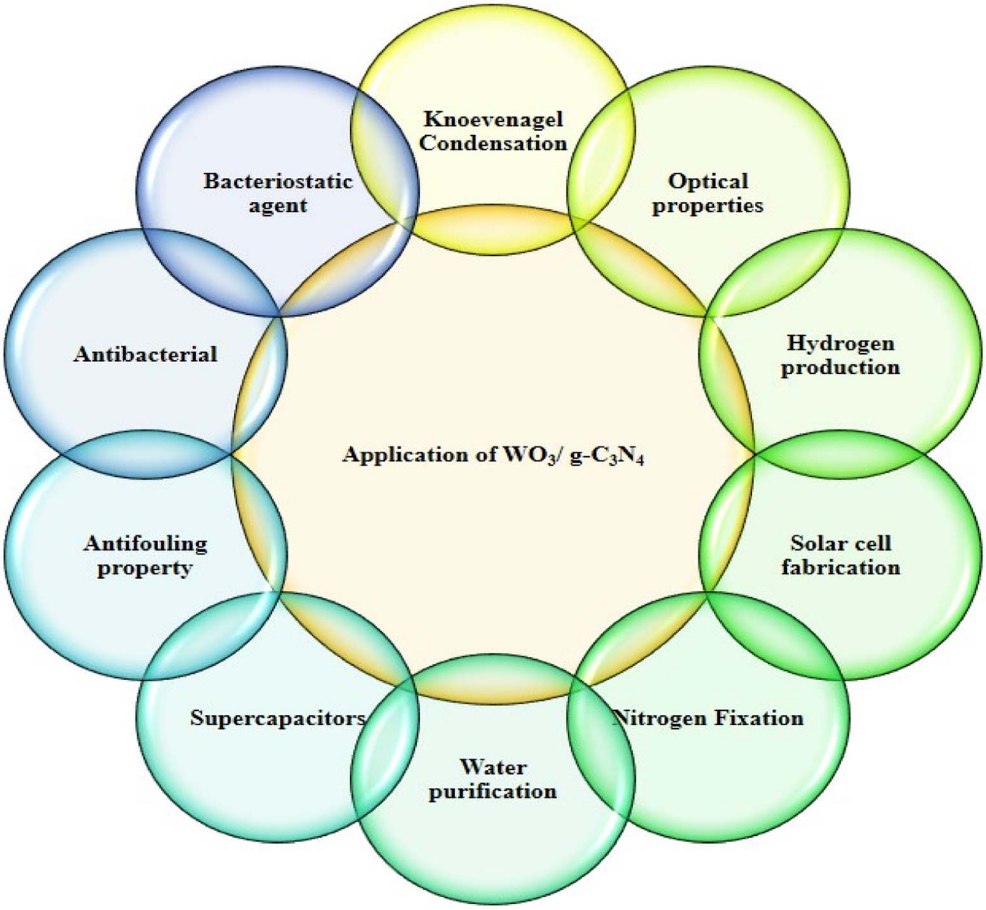

Fig. 3 Different applications of WO_3/g-C_3N_4-based materials.

when he obtained the "melon" linear polymer of carbon nitride (CN). Then, Franklin 1922 prepared g-C_3N_4 from mercuric thiocyanate by thermal decomposition.[61]

There are seven allotropes of graphitic carbon nitride, including α-C_3N_4 (bandgap 5.5 eV), β-C_3N_4 (bandgap 4.85 eV), pseudocubic-C_3N_4 (bandgap 4.13 eV), cubic-C_3N_4 (bandgap 4.3 eV), g-*o*-triazine (bandgap 0.93 eV), g-h-triazine (bandgap 2.97 eV), and g-h-heptazine (bandgap 2.88 eV) and g-C_3N_4, predicted by Teter and Hemley in 1996, as shown in Fig. 2a.[62–66] All these are hard crystalline forms of carbon nitride except g-C_3N_4. Among these, beta carbon nitride (β-C_3N_4) is a super hard material (pure carbon nitride bulk modulus 4.27 ± 0.15 Mbar) predicted to be harder than diamond (bulk modulus 4.43 Mbar). It has the same crystal structure as β-Si_3N_4.[62,67] Corkill and Cohen calculated the bandgap of β-C_3N_4 to be 6.4 ± 0.5 eV in 1993.[68]

In 1993, Chen *et al.* synthesized thin C_3N_4 films (by magnetron snorting) on Si medium and polycrystalline zirconium substrate in purely nitrogen medium and investigated the structure of C_3N_4 using electron microscopy and Raman spectroscopy.[67] Except for g-C_3N_4, all other phases of CN are super hard.[70] In 2009, Wang and their coworker first reported applying g-C_3N_4 in photocatalysis. These carbon materials (g-C_3N_4) gained importance in the scientific area when breakthrough

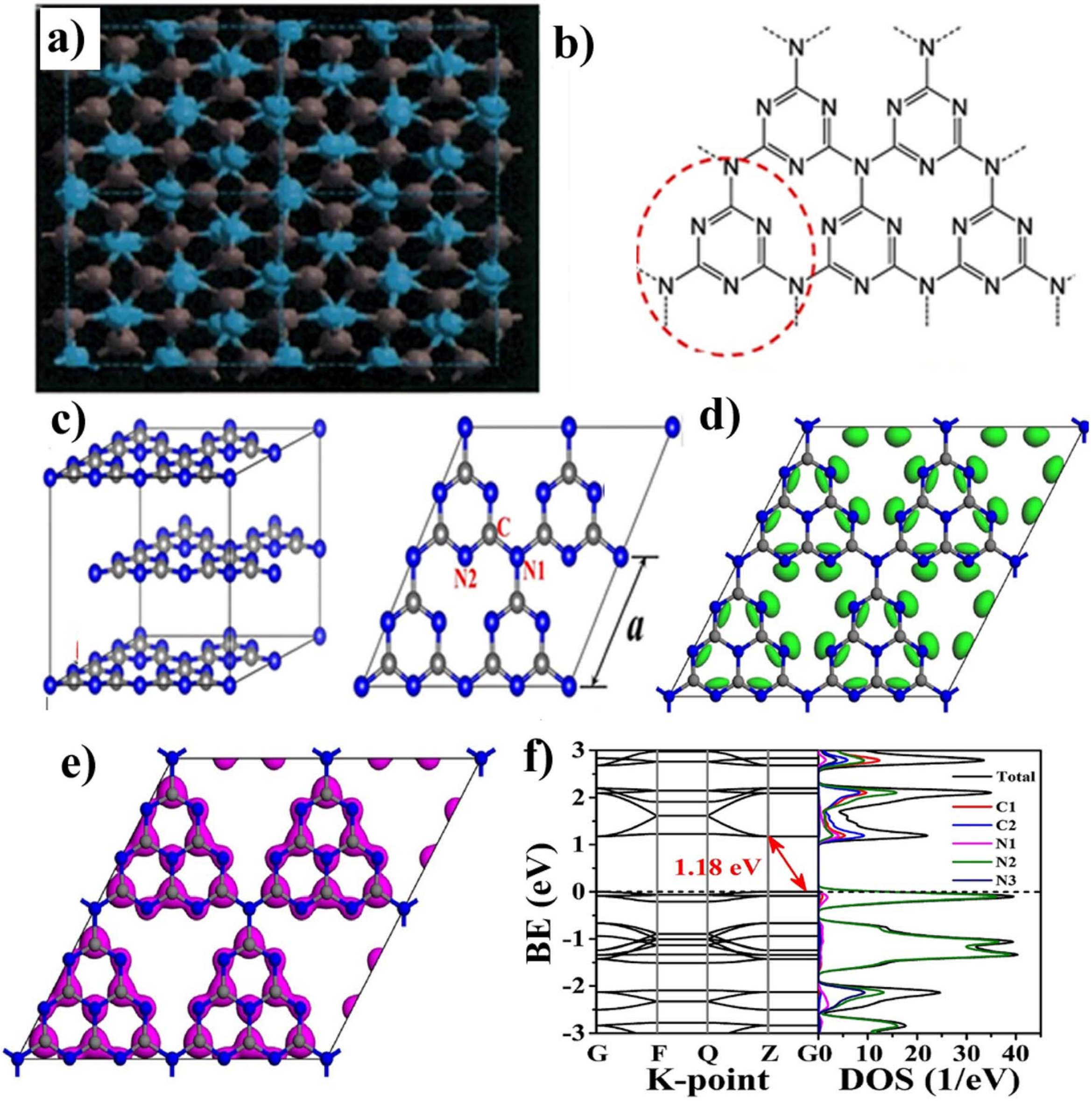

Fig. 4 (a) Cubic-C_3N_4 structures down the [00*l*] axis, showing grey spheres (C atoms) and blue (N atoms), (b) *s*-triazine, heptazine structures of g-C_3N_4 (reproduced with permission from ref. 66 Copyright 2017, Springer Nature). (c) Geometric structures of g-C_3N_4 bulk and g-C_3N_4 monolayer, DFT structure (reproduced with permission from ref. 75 Copyright 2019, Wiley Online Library). (d) Calculated HOMO, (e) LUMO, (f) band structure and corresponding DOS of monolayer g-C_3N_4 (G, F, Q, and Z are high symmetry points in the reciprocal space) (reproduced with permission from ref. 76 Copyright 2017, Elsevier).

research was published in 2009, describing the water splitting to hydrogen gas.[71]

Moreover, g-C_3N_4 can be obtained from cheap precursors such as nitrogen-rich compounds cyanamide, dicyandiamide, thiourea, guanidinium chloride, guanidine thiocyanate urea, and melamine, and its large-scale production is easy by low-cost synthesis.[66,67] It is easy to modify the structures and morphology of the g-C_3N_4; thus, it has become a hot topic for researchers.[72]

Crystalline structure and DFT calculations of graphitic carbon nitride. Heptazine units (hexatomic ring) polymerize to form the graphitic phase (g-C_3N_4); its geometry matches with graphite in which a nitrogen atom replaces a carbon atom. Due to this, replacing graphite (crystalline) is 97% less dense than g-C_3N_4 (crystalline).[64] Heptazine units (hexatomic ring) are composed of triazine units, which have two chemical structures, *s*-triazine (C_3N_3) and tri-*s*-triazine (C_6N_7) units (Fig. 4(b)), belonging to *R*3*m* space group. At ambient conditions, tri-*s*-triazine-based activity favors a stable phase of g-C_3N_4.[62,64,66,73] In g-C_3N_4 carbon, hydrogen atoms are interconnected through sp^2 hybridization, attached by a sigma bond-forming hexagonal layer geometry connected by van der Waals forces (π–π interaction).[66] The experimental results revealed by the XRD patterns suggest that the unit cell of tri-*s*-triazine-based g-C_3N_4 is a layered structure having an interlayer distance of 0.319 nm (Fig. 4(c)). The lone pair electrons on N and self-linkage property of C in each layer, tri-*s*-triazine repeated N atoms engage units, and the calculated distance is 0.712 nm between two N pores. The six-fold cavity is formed by encircling 3 adjacent heptazin units. Based on the symmetry of the tri-*s*-triazine structure, 3 nonequivalent N atoms and 2 nonequivalent C atoms are present, indicated by (N1–N2–N3/C1–C2, respectively) with N1–C1, C1–N2, N2–C2, and N2–C3 bond lengths of 0.147 nm, 0.134 nm, 0.133 nm, and 0.139 nm, respectively.[69,74,75]

Moreover, the bulk structure of g-C_3N_4 is formed through multilayer stacking, known as 'AB-stacking'. The interaction energy between adjacent layers measures 0.036 eV Å^{-2}, indicating the presence of van der Waals forces (weak π–π interactions) between the layers. The semiconductors' energy bandgap (E_g) was calculated using the GGA-PBE (generalized gradient approximation Perdew–Burke–Ernzerhof) function, predicting an E_g of 1.2 eV for monolayer g-C_3N_4 lower than the experimental value of 2.7 eV. The HSE06 functional provides a more accurate prediction, suggesting an E_g of 2.7 eV. In both cases, g-C_3N_4 exhibits an indirect bandgap, with the valence band maximum (VBM) and conduction band minimum (CBM) located at different K points in the Brillouin zone. The calculated band structure and corresponding DOS of monolayer g-C_3N_4 (G, F, Q, and Z are high symmetry points in the reciprocal space).[77] The lowest unoccupied molecular orbital (LUMO) and highest occupied molecular orbital (HOMO) of monolayer g-C_3N_4 were calculated, as shown in Fig. 4(d–f). Following the electronic density of states (DOS), the HOMO covers all N2 atoms, while the LUMO is primarily found on C1 and C2 atoms with some N1 and N2 atoms. The tri-coordinated bridge N (N3) atoms do not contribute to the VB or CB edge, and in essence, N3 atoms do not produce excited electrons when exposed to light, and they do not allow electron migration through N3 atoms or transfer between heptazine (C_6N_7) units. Consequently, the photogenerated electron–hole pairs remain localized within each heptazine unit, resulting in inefficient separation and poor photocatalytic performance.

Crystalline structure and DFT calculation of tungsten oxide. Robert Oxland 1841 reported the first preparation method of sodium tungstate (Na_2WO_4) and tungsten trioxide (WO_3). Soon after, he was considered the founder of systematic tungsten chemistry after they were granted a patent for their work. The density of tungsten, equal to that of gold (19.3 g cm^{-3}), is among the highest of all metals. Due to its high melting point, it is used as a refractory metal. Tungsten's applications include water splitting, gas sensing, solar cells, disinfection, and degradation of pollutants *via* photocatalysis and photoelectrocatalysis.[45,78] WO_3 is an ideal candidate out of the many visible active photocatalysts due to the ideal bandgap (2.4–2.8 eV), covering a large range of the solar spectrum. It has high oxidation power (valence band holes +3.1–3.2 V NHE), stability, and nontoxicity.[79] WO_3 exists in different crystalline phase at different temperatures (−180 and 900 °C), displaying several phase transitions such as monoclinic epsilon (ε-WO_3 phase <−43 °C), triclinic delta (δ WO_3 phase −43 to 17 °C), monoclinic gamma (γ-WO_3 phase 17 to 330 °C), orthorhombic beta (β-WO_3 phase 330–740 °C), and tetragonal alpha (α-WO_3 phase above 740 °C). In addition, other orthorhombic and hexagonal crystalline phases have been reported (Fig. 5(a)). Among these, monoclinic γ-WO_3 phase (space group $P2_1/n$, 17 to 330 °C) is the most stable, with a bandgap of 2.4–2.8 eV.[79,80] The band structure and the DOS of monoclinic WO_3 were calculated using DFT, Perdew–Wang (PW91), and hybrid functionals. All three functional types predict a direct bandgap for monoclinic WO_3 at room temperature, contradicting experimental results and previous revised Perdue Burke Ernzerhof (PBE) calculations. However, a generalized gradient approximation (GGA) study also reported a direct bandgap and argued that the discrepancy observed in the experimental data could be artificial. Under specific conditions, a direct bandgap may manifest experimental properties that can be mistakenly interpreted as originating from an indirect bandgap. All three hybrid functionals yield a significantly larger bandgap than the standard GGA, at the same time maintaining the same nature of the bandgap (direct or indirect). Among them, the HSE06 hybrid functional with a plane wave basis achieved the best agreement with the experimental value, yielding a bandgap of 2.80 eV. The B3LYP hybrid functional with a localized basis set follows closely with a bandgap of 3.13 eV. The PBE_0 functional overestimates the bandgap, yielding a value of 3.67 eV,[81] as shown in Fig. 5(b–d). Fu *et al.*[82] performed DFT computational calculations to investigate further interfacial charge transfer (for WO_3 and g-C_3N_4). The electrostatic potentials and work functions for WO_3 (001) and g-C_3N_4 (001) were calculated to be 6.23 and 4.18 eV, respectively. The difference in the work function diagram exhibits the charge transfer (at the interface of WO_3 and g-C_3N_4). WO_3 has a greater work function, requiring more energy to remove an electron from its surface than g-C_3N_4. As a result, there is a tendency for electrons to transfer from g-C_3N_4 to WO_3 until the Fermi level equilibrium is reached. This charge

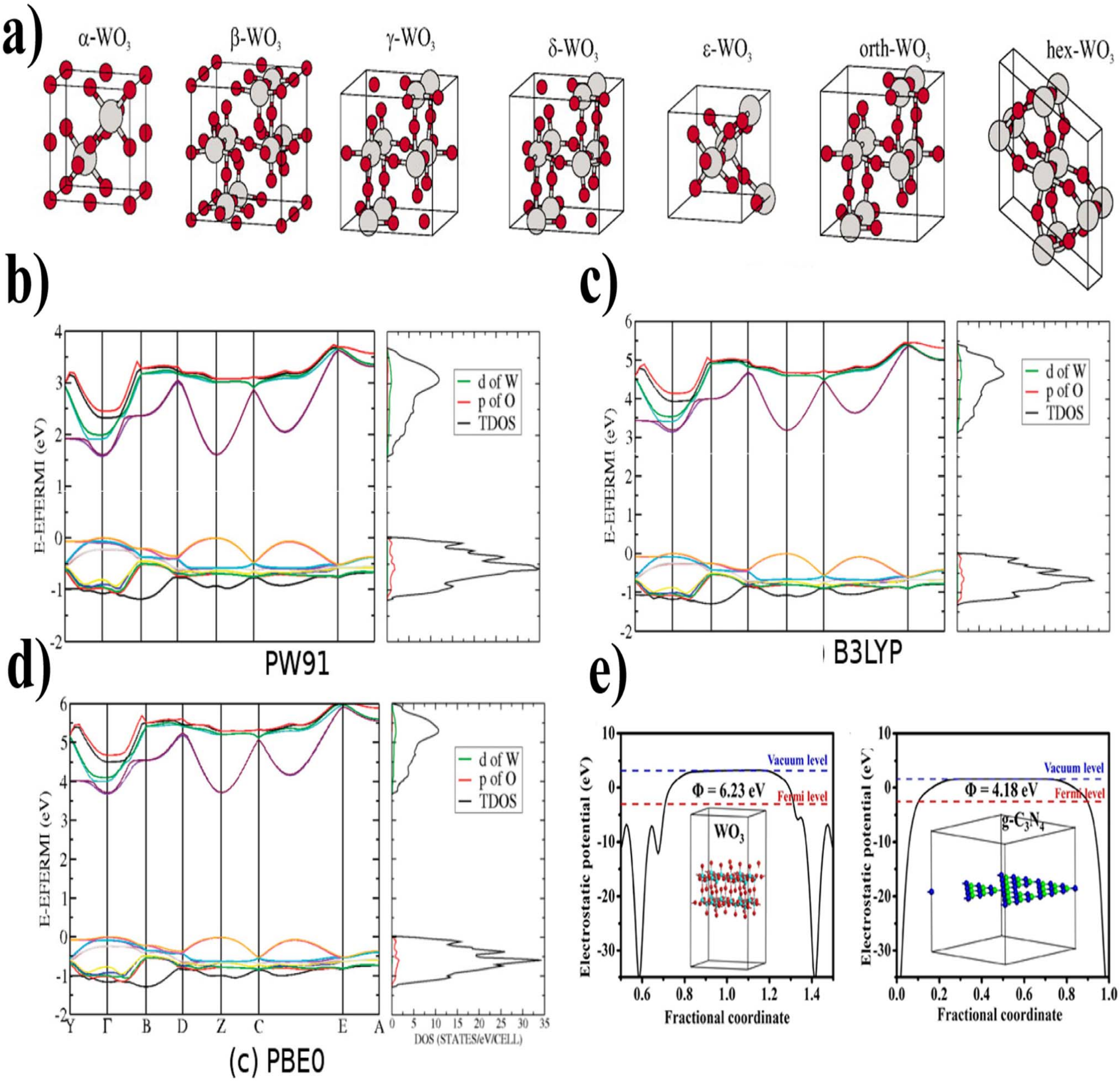

Fig. 5 (a) The unit cells of WO3 at different temperatures show different phases (reproduced with permission from ref. 79 Copyright 2010, AIP Publishing). (b) PW91, (c) B3LYP, (d) PBE_0 (band structure and density of states (DOS) of room-temperature monoclinic WO_3 by different kinds of functionals) (reproduced with permission from ref. 81 Copyright 2011, American Chemical Society). (e) Electrostatic potentials WO_3 (001) surface and g-C_3N_4 (001) surface (reproduced with permission from ref. 82 Copyright 2018, Elsevier).

transfer occurs to equalize the Fermi levels of two materials. The charge transfer process forms an interfacial built-in electric field from the charge separation between the WO_3 and g-C_3N_4 interface. At the interface, the WO_3 surface is −ve while the surface of g-C_3N_4 is +ve, as shown in Fig. 5(e). The intensity of the built-in electric field is significantly enhanced due to the thin layered structures (g-C_3N_4, WO_3) as well as strong Coulomb force, which is beneficial for the transfer and separation of interfacial charge carriers than the bulk counterparts. When materials are in thin layers or have a high surface area, the interfacial contact between them increases, allowing for more efficient charge transfer and separation. In addition, the strong Coulomb force between the charged particles (electrons and holes) within the thin layered structures further enhances the built-in electric field.

Fabrication strategies for graphitic carbon nitride–tungsten oxide

Various techniques, such as *in situ* growth, impregnation, thermal treatment, precipitation, ultrasonication, and calcination, have been explored to combine the two components effectively. The design principles of fabrication and strategies involve the meticulous control of synthesis parameters, interfacial engineering, morphology and composition control, and performance optimization through various strategies. By advancing these design principles and strategies, nanocomposites hold great promise for applications in photocatalysis, environmental remediation, and other fields where efficient and sustainable materials are required. Here, we describe a few methods of synthesis and fabrication of WO_3/g-C_3N_4 and their doped composites.

Fu and coworkers[82] designed 2D–2D ultrathin WO_3/g-C_3N_4 from electrostatic-assisted ultrasonic exfoliation of WO_3 and two-step thermal etching of g-C_3N_4 (Fig. 6(a)). Fig. 6(b) indicates the zeta potentials at pH 4 of bulk WO_3 (−9.7 mV) and WO_3 nanosheets (−22.8 mV), indicating that the higher zeta potential value for WO_3 nanosheets relative to the bulk WO_3 and nanosheet of g-C_3N_4 show positive zeta potential (+10.3 mV) at the same pH. The opposite value of zeta potential results in strong electrostatic attraction, which is beneficial for charge transfer in WO_3 and g-C_3N_4. The work function of WO_3 is greater than the g-C_3N_4 value, inducing a charge transfer from g-C_3N_4 to WO_3. Three factors, namely, Coulomb interaction, band edges, and internal electric field, play a major role in stopping the recombination of electrons from the conduction band of WO_3 and holes (h^+) from the valence band (VB) of g-C_3N_4. These factors also stop the recombination power of electrons from the conduction band of the g-C_3N_4 and holes (h^+) from the valence band of WO_3. Praus *et al.*[83] first synthesized the WO_3/g-C_3N_4 using zeta potential values by dispersing both components (exfoliated g-C_3N_4 and WO_3) in an aqueous solution at pH = 2. In the pH range of 1.4–4.0, WO_3 shows negative zeta potentials, while exfoliated g-C_3N_4 exhibited positive zeta potential. X. Han *et al.*[84] developed the WO_3/g-C_3N_4 (2D) named CNW composite through the hydrothermal process for H_2 generation using the following precursors: melamine, CTAB, hexadecyl-trimethyl-ammonium-bromide, and WCl_6. 2D WO_3/g-C_3N_4 (10 wt% WO_3) caused 1853 (mmol h^{-1} g^{-1}) H_2 generation, and the BET of CNW-10 was 86 m^2 g^{-1}. This value is 20 and 2.5 times greater than that of pristine WO_3 and g-C_3N_4 NSs, respectively. Similarly, the average pore diameter and volumes for g-C_3N_4 NSs (2.0 nm, 0.24 cm^3 g^{-1}), CNW-10 (2.0 nm, 0.44 cm^3 g^{-1}), and WO_3 (8.1 nm, 0.02 cm^3 g^{-1}) were determined. Similarly, Zhuang *et al.*[85] synthesized the 2D–2D-WO_3/g-C_3N_4 2D–2D heterostructure by an *in situ* preparation strategy from dicyandiamide, $Na_2WO_4 \cdot 2H_2O$, and NH_4F for RhB degradation. Sample CNW-13 (13%, WO_3) completely degraded RhB within 40 min. The photocatalyst showed efficient photocatalytic properties and good stability after several cycles. However, synthesizing 2D–2D WO_3/g-C_3N_4 can be complex and challenging. Achieving the desired morphology, composition control, and interfacial properties in these hybrid structures requires precise synthesis techniques. This complexity can limit these materials' scalability and real-life implementation. Similarly, 2D–2D structures may have time-limited light absorption capabilities (particularly in certain range wavelengths). Thus, they might not efficiently utilize the whole solar spectrum of visible light, leading to lower photocatalytic efficiency.

The elegant WO_3/g-C_3N_4 composite hollow microspheres (CHMs), inorganic–organic 2D–2DWO_3/g-C_3N_4 nanosheets (NS), and WO_3 nanosheets NS/g-C_3N_4 nanosheets (NS) were synthesized by various researchers (Fig. 7(a–e)).[86] A strategy was developed to enhance the heterostructure system by modulating the electronic and surface properties. A thin 2D/2D WO_3/g-C_3N_4 heterojunction with carbon doping and the bridge were constructed with anionic polyacrylamide (APAM act as functions as the assistant template and carbon source). WO_3 and APAM were inserted into the g-C_3N_4 nanosheet, as shown in Fig. 7(a). APAM is a hydrophilic polymer used for its carbonization potential, and the amide group forms hydrogen bonds on the g-C_3N_4 surface. In the above study, APAM was utilized as a template to fabricate a carbon-decorated 2D/2D WO_3/g-C_3N_4 heterostructure based on Z-scheme photocatalysts and compared to individual WO_3, g-C_3N_4, and their binary composites. The synthesized composite demonstrated significantly enhanced the degradation activity for tetracycline under

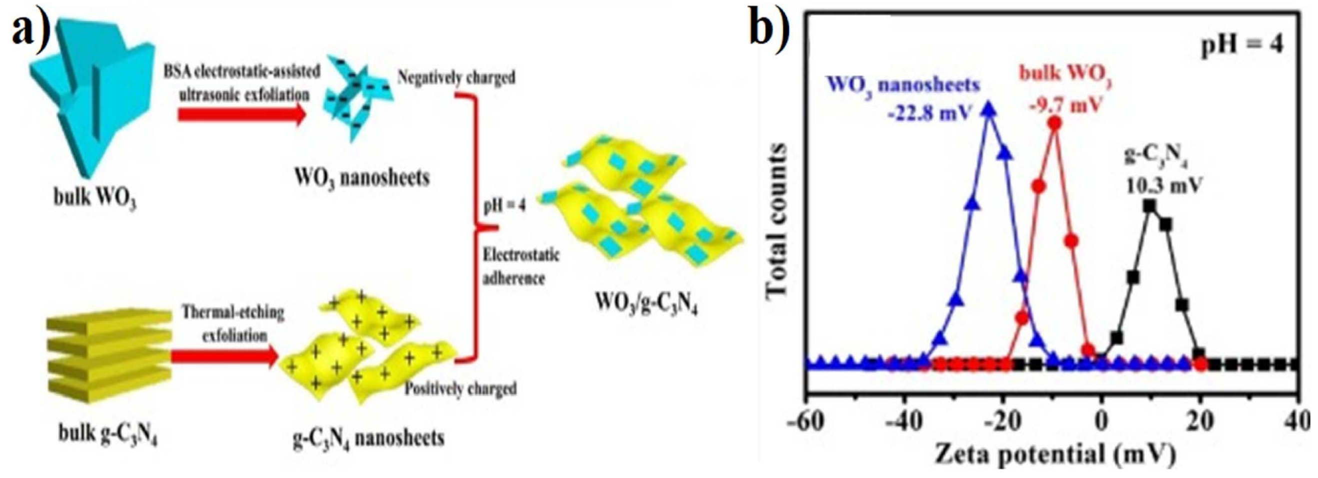

Fig. 6 (a) Systematic synthesis scheme of 2D–2D heterojunction WO_3/g-C_3N_4 through electrostatic interaction (Coulomb interaction), (b) pH = 4 value of zeta potentials of bulk and nanoscale sheets of WO_3 and g-C_3N_4 (reproduced with permission from ref. 82 Copyright 2018, Elsevier).

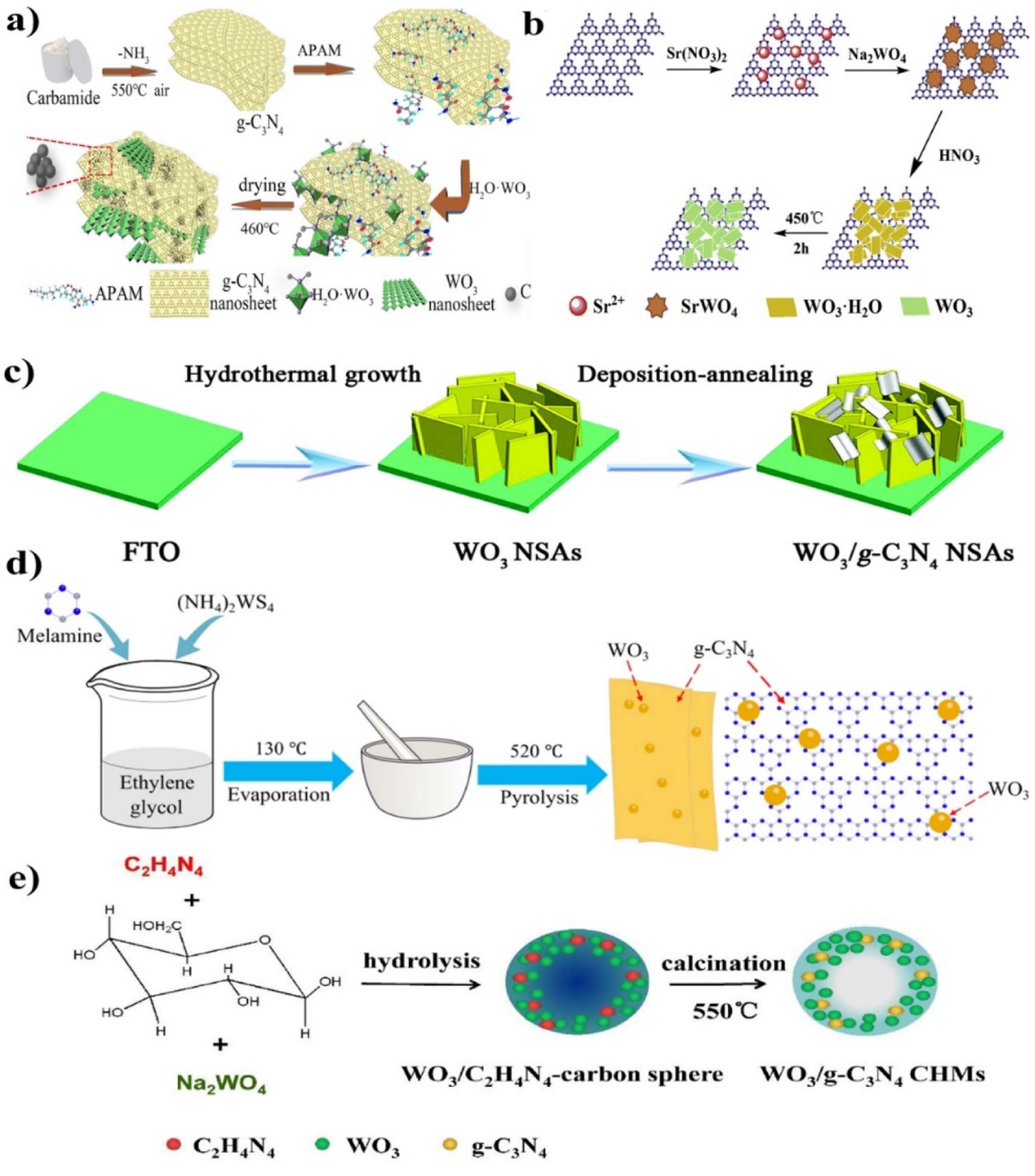

Fig. 7 (a–e) Synthesis processes for the 2D–2D$WO_3/g\text{-}C_3N_4$ heterojunction through different methods ((a) reproduced with permission from ref. 86 Copyright 2020, Elsevier, (b) reproduced with permission from ref. 87 Copyright 2018, Elsevier, (c) reproduced with permission from ref. 88 Copyright 2018, Royal Society of Chemistry, (d) reproduced with permission from ref. 89 Copyright 2017, IOP Publishing Ltd (e) reproduced with permission from ref. 90 Copyright 2017, Elsevier).

visible light irradiation, attributed to the reduced bandgap, fast charge transfer rate, and enhanced quantum efficiency.

Chen *et al.*[87] synthesized a novel hierarchical sheet-on-sheet composite, successfully fabricated by a simple calcination method using acid-treated $SrWO_4/g\text{-}C_3N_4$ as the precursors, as shown in Fig. 7(b). The synthesized WOCN composites demonstrated significantly enhanced photocatalytic activity in RhB degradation under simulated sunlight irradiation. The improved photocatalytic performance was attributed to forming a hierarchical heterostructure, which provided a larger specific surface area, improved visible-light absorption capability, reduced recombination of electron–hole pairs, and enhanced charge carrier separation efficiency. Li *et al.*[88] synthesized the WO_3 nanosheet arrays (NSAs) using a hydrothermal growth method, and g-C_3N_4 NSAs on an FTO substrate were prepared through a deposition–annealing process. Specifically, the WO_3 NSAs grown on FTO were immersed in g-C_3N_4 NS dispersions for 1 h and then dried using a nitrogen stream. After repeating this cycle three times, the resulting sample was annealed at 400 °C for 1 h to enhance the adhesion between g-C_3N_4 NS and WO_3 NSAs, facilitating the formation of WO_3/g-C_3N_4 heterojunction arrays (Fig. 7(c)).

Cheng *et al.*[89] synthesized the WO_4/g-C_3N_4 by the one-pot pyrolysis method (Fig. 7(d)). The resulting product was labeled as WO_4/g-C_3N_4. During the high-temperature synthesis, the interaction between WO_3 and g-C_3N_4 modified the composite textural structures, thus improving the photocatalytic activity.[90] The elegant Z-scheme hollow microspheres WO_3/g-C_3N_4 composite was synthesized by precisely controlling the *in situ* hydrolysis, followed by the polymerization process consecutively, and the synthesis mechanism is shown in Fig. 7(e). The hollow structure gained significant attention due to its unique structural, physical, and chemical properties. These structures possessed characteristics such as low density, high specific surface area, and efficient mass transfer and photon utilization, and were used for photocatalytic reduction purposes. Also, the specific hollow structure enabled prolonged light trapping and enhanced photon utilization efficiency.[91,92]

Similarly, a few methods reported to synthesize transition metal-doped WO_4/g-C_3N_4 are given in Fig. 8(a–c) to fabricate

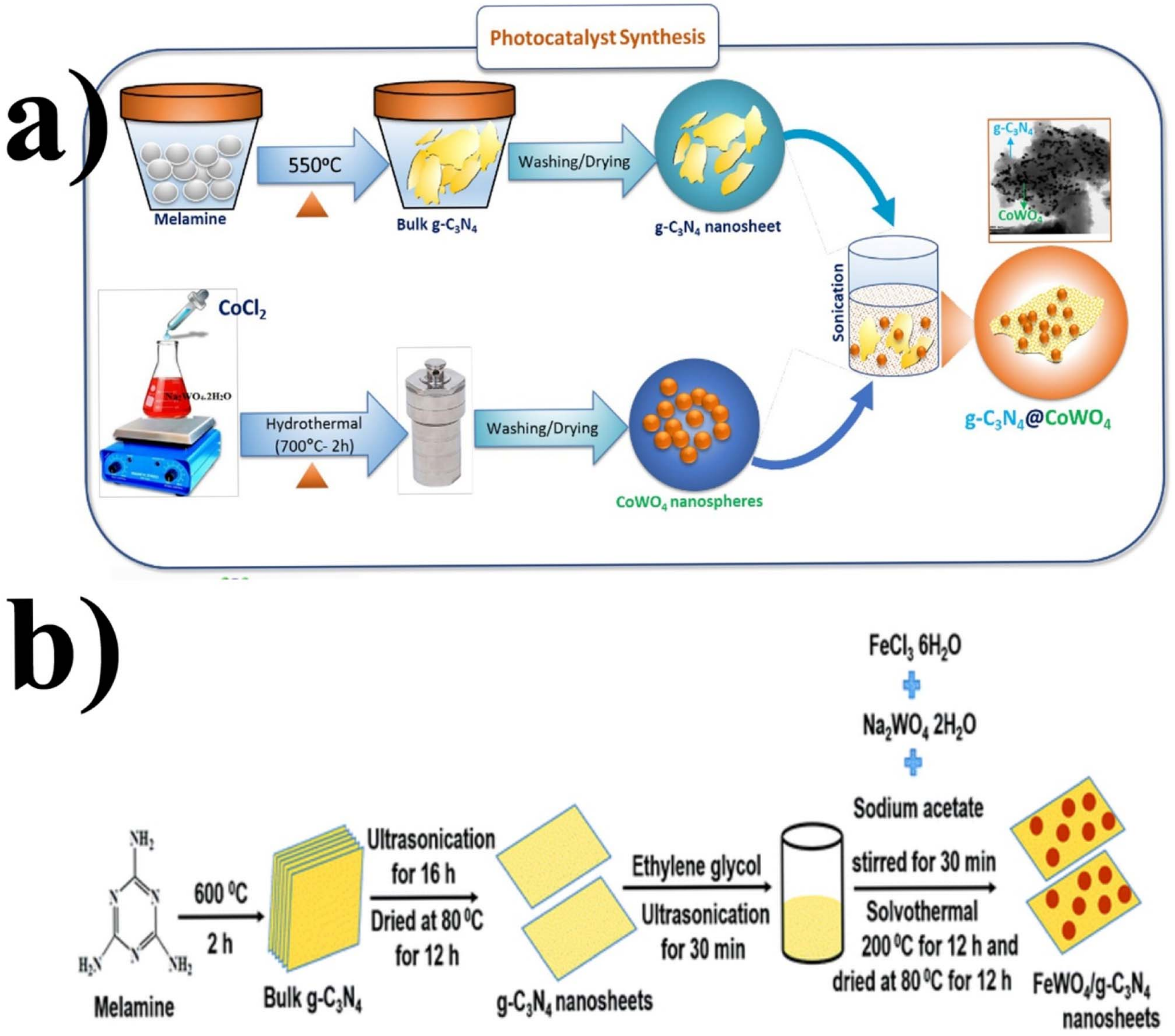

Fig. 8 (a) Fabrication of codoped WO_4/g-C_3N_4-based photocatalytic material (reproduced with permission from ref. 93 Copyright 2019, Elsevier). Schematic representation (b) of the $FeWO_4$/g-C_3N_4 nanosheet composites preparation (reproduced with permission from ref. 97. Copyright 2018, Royal Society of Chemistry).

codoped WO_4/g-C_3N_4, flowerlike $MnWO_4$ loading g-C_3N_4 surface, and $FeWO_4$/g-C_3N_4 nanosheet composites, respectively. Prabavathi *et al.*[93] successfully synthesized $CoWO_4$ nanoparticles assembled on g-C_3N_4 nanosheets by the hydrothermal method, followed by ultrasonication. The photocatalytic activity of fabricated $CoWO_4$/g-C_3N_4 was investigated by the degradation of norfloxacin under visible light, demonstrating higher photocatalytic activity than pristine materials (Fig. 8(a)). The excellent photocatalytic activity of these materials was due to a bivalent metal tungstate semiconductor with excellent thermal and chemical stability; combining this metal tungstate with g-C_3N_4 showed enhanced photocatalytic activity. The binary metal oxide cobalt tungstate ($CoWO_4$) demonstrated remarkable catalytic performance due to its feasible redox couple states (Co^{2+}/Co^{3+}) and high electrical conductivity ranging from 10^{-7} to 10^{-3} S cm^{-2}. Incorporating tungsten (W) atoms in cobalt oxide significantly improved its conductivity compared to pristine cobalt oxide materials.[94] Liu *et al.*[95] reported the direct Z-scheme $MnWO_4$/g-C_3N_4 composite fabricated by a facile hydrothermal method. Forming a direct Z-scheme photocatalytic system is a promising and effective approach to minimize the recombination of photogenerated electrons and holes while maintaining the redox ability of each component.[96] The energy level and band structure of $MnWO_4$ (narrow bandgap (2.7 eV)) were well-matched with those of g-C_3N_4, making it suitable for the formation of $MnWO_4$/g-C_3N_4 heterojunction with excellent photocatalytic activity under visible light.

Dadigala *et al.*[97] synthesized a novel, stable, highly efficient, and visible light active hybrid photocatalytic system for $FeWO_4$/g-C_3N_4 nanosheets by the *in situ* self-assembly solvothermal approach. These photocatalysts exhibited superior photocatalytic activity for RhB and TC compared with the pure $FeWO_4$, g-C_3N_4 nanosheets (Fig. 8(b)). The $FeWO_4$/g-C_3N_4 composite showed excellent photocatalytic activity because the band level alignment between $FeWO_4$ and g-C_3N_4 allowed the formation of a direct Z-scheme photocatalytic system, enabling the efficient separation and transfer of photogenerated electron–hole pairs. Besides, $FeWO_4$ and g-C_3N_4 are visible light-driven photocatalysts, and their combination as the $FeWO_4$/g-C_3N_4 composite holds promise for achieving high photocatalytic activity.

The design of graphitic carbon nitride–tungsten oxide involves the careful consideration of several key factors. Firstly, the choice of synthesis method is crucial in achieving a well-controlled and homogeneous dispersion of tungsten species. Another important design principle is the tuning of the interface and the interfacial interactions. The interface facilitates efficient charge transfer and promotes synergistic effects between the two materials. Surface modification, functionalization, and heterojunction formation can enhance the interfacial contact and optimize the interfacial charge transfer kinetics. Bandgap engineering to expand the light absorption range, surface modification to enhance the catalytic activity, and cocatalyst deposition to improve charge separation and transfer. The morphology and composition composites are essential to design aspects and can be tailored by controlling the reaction conditions and precursor compositions to obtain desired structures, such as nanoparticles, nanosheets, or hierarchical architectures. Furthermore, efforts can be directed toward optimizing the composition ratios, improving the crystallinity, and exploring novel hybridization to unlock additional functionalities and applications.

The fabrication and photocatalytic applications of g-C_3N_4/WO_3 pose several scientific challenges. One of the challenges is the effective synthesis of well-defined nanocomposite structures with controlled morphology and composition of g-C_3N_4/WO_3. Achieving a uniform dispersion of WO_3 on g-C_3N_4 and maintaining their intimate contact is crucial for maximizing the synergistic effects between the two materials.[56,59] Strategies such as metal doping, nonmetal doping, codoping, and heterojunction formation have been explored to modulate the crystallographic, textural, and electronic properties of nanocomposites to enhance their photocatalytic efficiency. However, the cost of these metals is very high; thus, they are not used on a larger scale.[98,99] Developing efficient catalysts for the degradation of pollutants, H_2 evolution, and CO_2 using g-C_3N_4/WO_3 requires a comprehensive understanding of photocatalytic mechanisms and reaction pathways. Exploring the fundamental principles governing the photocatalytic mechanism and elucidating the roles of each component is essential for designing and optimizing a photocatalyst. The fabrication and photocatalytic applications of g-C_3N_4/WO_3 nanocomposites face synthesis, performance optimization, and mechanistic understanding challenges. Addressing these challenges will contribute to advancing g-C_3N_4/WO_3 nanocomposites for various environmental applications.

Graphitic carbon nitride-tungsten oxide (MWO_x/g-C_3N_4) composites. A photocatalyst should have a special characteristic requirement. The most prominent is narrow bandgap energy that helps establish coupling hybridization in visible light and a suitable band position to carry out the redox reaction. Similarly, the potential chemical difference offers the band-bending junction interface between the coupled semiconductors. Single semiconductors such as g-C_3N_4 or WO_3 cannot fulfill these requirements alone. The construction of the graphitic carbon nitride-based tungsten oxide (MWO_x/g-C_3N_4) design nanostructured materials can overcome these issues. This review deeply analyzed all the research directions of the MWO_x/g-C_3N_4 nanostructured materials prepared and their organic pollutants efficiency in the last 6 years.

WO_3/g-C_3N_4 composite. WO_3/g-C_3N_4 exhibits improved photocatalytic activity compared to pristine components. Introducing WO_3 into g-C_3N_4 induces changes in the electronic structure, leading to red-shifted optical absorptions and upward absorption tails in all the hybrids. The synergistic effect between WO_3 and g-C_3N_4 enhances visible light absorption and promotes efficient charge carrier separation, thus enhancing the photocatalytic performance. WO_3/g-C_3N_4 demonstrates an excellent response to visible light irradiation, enabling it to harness a broader range of solar energy for photocatalytic reactions. It also utilizes a larger portion of the solar spectrum and increases the potential for energy conversion and environmental remediation. WO_3 provides structural stability and prevents the aggregation of g-C_3N_4, resulting in improved long-term performance. Kadi *et al.*[100] synthesized g-C_3N_4 nanosheets with high surface area *via* a calcination approach using the high mesoporous MCM-41. It was observed that incorporating WO_3 nanoparticles on the g-C_3N_4 surface increases the charge separation, lowers the bandgap value, and results in higher efficiency.

Electron-rich graphitic nitride materials transfer partial electrons to WO_3 due to the lone pair electrons on nitrogen, thus increasing the electron density of WO_3. A stable g-C_3N_4/WO_3 composite structure formed by strong interactions leads to stable activity. For strong interaction between g-C_3N_4 and WO_3, the interfacial charge transfer reduces the recombination of the e^-/h^+ pair, leading to improved efficiency. When weak interactions are formed between two components, decreased photocatalytic activity is observed since the g-C_3N_4/WO_3 composite can split into a mixture of the g-C_3N_4 and WO_3.[101,102] Huang *et al.*[101] first synthesized g-C_3N_4/WO_3 nanomaterial from precursor dicyandiamide and $(NH_4)_5H_5[H_2(WO_4)_6]\cdot H_2O$ for the degradation of 4-chlorophenol (4-CP) and methylene blue (MB), as shown in Fig. 9(e and f). The result indicates that under visible light irradiation, the activity of WO_3/g-C_3N_4 nanomaterial was 4.2 and 2.9 times higher than that of pristine WO_3 and g-C_3N_4, respectively. The TGA results in Fig. 9(a) reveal that the weight loss of WO_3/g-C_3N_4 occurs in the 510–670 °C temperature range. WO_3/g-C_3N_4 composites show stability before 510 °C (Fig. 9(b)). The SEM images of WO_3 indicate that it has obvious edges with particle sizes of approximately 50–200 nm. The TEM images in Fig. 9(e and f) show bright particles of about 100–200 nm diameters (red circles) attached to the g-C_3N_4 surface. WO_3/g-C_3N_4 showed 97% photocatalytic degradation efficiency for MB degradation within 2 h and 43% for 4-CP within 6 h under visible light irradiation (heterojunction formation due to interparticle electron transfer between component semiconductors). In the 4-CP structure, Cl and oxygen atom are strongly covalently bonded to the aryl or phenyl group, and there is no attacking side for the catalyst, while methylene blue has many atoms in the ring such as sulfur and nitrogen available for attack. These bonds easily break down in methylene blue. This issue can be resolved if the pH is optimized for this reaction.

Chen *et al.*[104] prepared the WO_3/g-C_3N_4 composite by heat treatment and ball milling procedures. They prepared different samples by varying the g-C_3N_4 and WO_3 to check the methylene blue (MB) and fuchsin (BF) degradation efficiency. The photocatalytic efficiencies of pure g- and g-C_3N_4 and WO_3 for MB (35.6%, 40.0%) and BF (30.9%, 42.4%) were determined. When the quantity of WO_3 is 5.0 wt% in g-C_3N_4, the photocatalyst displays the greatest photocatalytic activity, with the photocatalytic efficiencies for MB and BF of 87.9% and 75.6%, respectively. Yang *et al.*[43] manufactured the WO_3/g-C_3N_4 materials through three different methods such as ultrasonic dispersion, calcination, and hydrothermal method, and the prepared samples by these processes were named CNW(U), CNW(C), and CNW(H), respectively. They used the synthesized materials for Rhodamine B degradation. The rate constant for

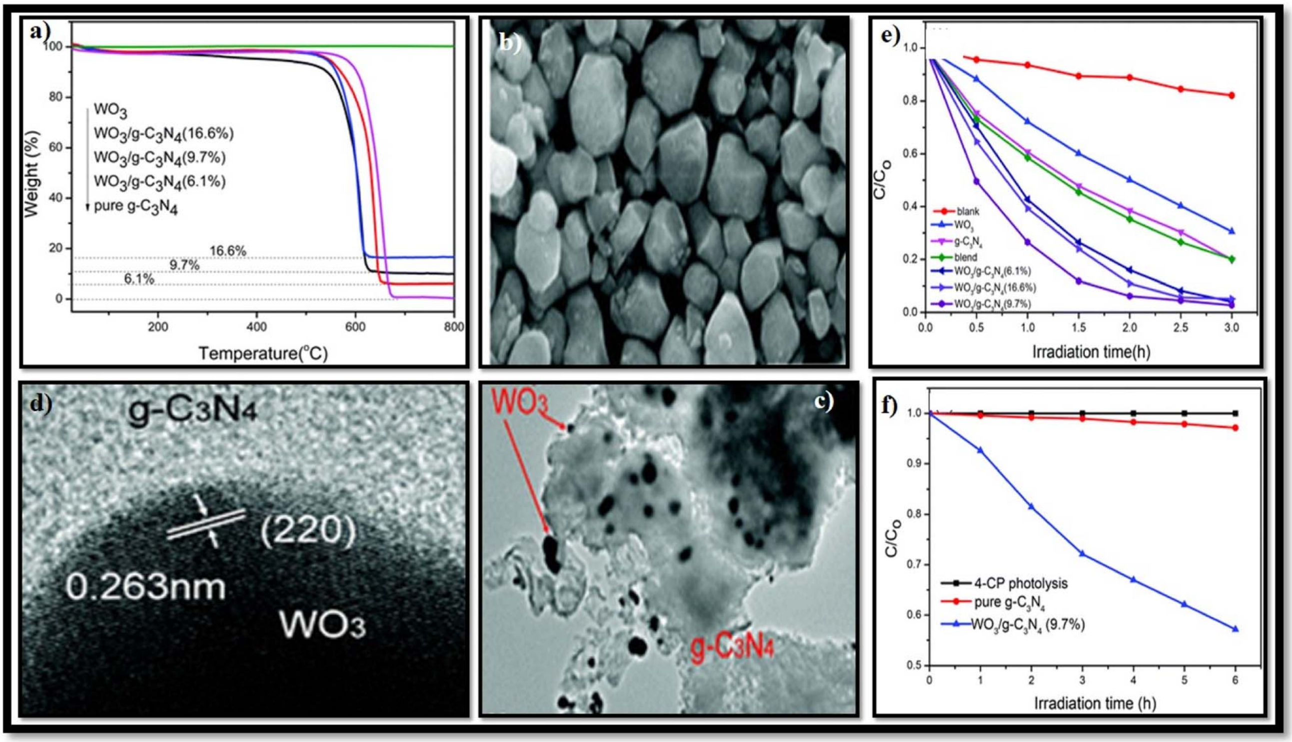

Fig. 9 (a–f) (a) TGA of WO_3/g-C_3N_4, (b) SEM of WO_3, (c) TEM of WO_3/g-C_3N_4, (d) HRTEM of the WO_3/g-C_3N_4 (9.7%) composite, (e) degradation rate of MB by g-C_3N_4, WO_3, and WO_3/g-C_3N_4, and (f) degradation rate of 4-CP by g-C_3N_4 and WO_3/g-C_3N_4 (reproduced with permission from ref. 103 Copyright 2013, Royal Society of Chemistry).

CNW(U), CNW(C), and CNW (H) was 0.034 min^{-1}, 0.022 min^{-1}, and 0.048 min^{-1}, respectively. CNW(H) showed a rate constant 4 and 2.6 times higher than that of WO_3 (0.012 min^{-1}) and g-C_3N_4 (0.018 min^{-1}), respectively. The BET surface area of WO_3, g-C_3N_4, CNW(U), CNW(C), and CNW (H) was 60.6, 11.2, 14.7, 14.3, and 15.1 $m^2\ g^{-1}$, respectively. The degradation efficiency decreased in the order CNWH (95.3%) > CNWU (85.7%) > CNWC (77.2%). To examine the stability, efficiency, and morphological changes of g-C_3N_4/WO_3 with respect to temperature, Doan *et al.*[105] prepared the g-C_3N_4/WO_3 composite at different temperatures (500, 600, and 700 °C) and named them WM(500), WM(600), and WM(700), respectively. At 600 °C and 700 °C, the decomposition of g-C_3N_4 occurred, and N-doped WO_3 formation was realized. The maximum degradation was shown by WM(500) for 80% MB compared to other materials synthesized at different temperature ranges. The above experimental data show that the synthesis method affects the interaction between WO_3 and g-C_3N_4. For example, the hydrothermal method shows the maximum efficiency since it can disperse WO_3 on the g-C_3N_4 surface better than other methods. This strong interaction enhanced interfacial charge transfer, efficient separation of electron–hole pairs (photogenerated), and the highest photocatalytic activity. In addition, the stable composite structure (WO_3 and g-C_3N_4) formed by the strong interaction in CNW(H) contributed to its superior stability compared to other photocatalyst composites.

Similar photocatalytic degradation was performed by Gondal *et al.*[52] They synthesized g-C_3N_4/WO_3 with dissimilar ratios and degraded Rhodamine B (RhB) and methyl tertiary-butyl (MTBE). Almost all WO_3/g-C_3N_4 composites exhibited higher photocatalytic efficiency than pure WO_3 or g-C_3N_4. The photocatalyst g-C_3N_4/$WO_{3-x-0.1}$ (combination ratio of WO_3 of 0.1) exhibited the highest photocatalytic activity (62%) of RhB under visible light irradiation in 90 min, while under the same conditions, pristine WO_3 and g-C_3N_4 only showed a 42% and 27% photocatalytic efficiency, respectively. Similarly, the highest photodegradation efficiency of WO_3/g-C_3N_4-0.2 (combination ratio of WO_3 0.2) for MTBE (96.7%) was reported, while under the same conditions, the photodegradation proficiency attained on the pure phase of WO_3 and g-C_3N_4 was 65.9% and 45.3%, respectively. The photocatalytic activity gradually reduced when the combination ratio of WO_3 from 0.1 to 0.9 increased in g-C_3N_4. The reason could be the accumulation of WO_3 on pure g-C_3N_4. Increasing WO_3 on the graphitic carbon nitride decreased the separation efficiency of photoinduced electron–hole pairs and the photocatalytic activity effect.

As reported by Karimi and coworkers,[48] the WO_3/g-C_3N_4 (1 : 3) nanocomposite (W1G3) showed the best photocatalytic activity at pH 2.2 for the degradation of RB5 (99%) under solar light irradiation in 90 min. A greater amount of catalyst results in light scattering due to the reduction and aggregation of the irradiation field since higher concentration causes the solution to be more turbid, thus decreasing the light penetration ability and ultimately reducing the photocatalytic performance. Under proper light exposure, a maximum number of electrons were excited, and their efficiency increased. The acidic medium is most favorable for dye degradation instead of the basic medium. By changing the pH of the solution, the surface properties of the WO_3/g-C_3N_4 nanocomposite changed, thus reducing the number of positively charged species. In the basic solution, excess OH ions decreased the photodegradation of RhB5.

Zhang *et al.*[106] synthesized the same photocatalyst through direct calcination method from raw materials (ammonium tungstate, melamine) at 550 °C and applied it for the selective oxidation (photocatalytic) of 5-hydroxymethyl furfural (HMF) to 2,5-diformylfuran (DFF) in UV and visible light. Compared to visible light, UV light irradiation easily caused overoxidation and resulted in a lower DFF selectivity, and the highest DFF selectivity (85.6%) was achieved with HMF conversion (31.2%) in the presence of oxygen. They also studied the charge transfer/separation efficiency of photogenerated e^-/h^+ pairs of WO_3/g-C_3N_4, further confirmed by the EIS Nyquist circle. The Nyquist circle of WO_3 (4.7%)/g-C_3N_4 was smaller than that of the pristine. The larger diameters indicate greater interfacial resistance, resulting in a higher current loss. Due to its low conductivity, the g-C_3N_4 electrode exhibited a large ohmic serial resistance (R_s). The doping of g-C_3N_4 with WO_3 decreased the R_s value, demonstrating a faster interfacial charge transfer, reduced recombination, and enhanced photocatalytic efficiency. In addition, the photocatalytic oxidation of HMF to DFF on the g-C_3N_4 catalyst was higher in the presence of ACN and $PhCF_3$ as solvents. The choice of the reaction solvent commonly influences the efficiency of a chemical reaction. Each solvent possesses distinct characteristics such as steric hindrance effect, dielectric constant, polarity, and acid–base properties. This enhanced performance could be attributed to its lower polarity and superior oxygen dissipation. Conversely, polar solvents may lead to reduced conversion rates due to their potential competition with the reactant for the active catalytic site.

Yan *et al.*[107] reported the *in situ* coupling of WO_3 with g-C_3N_4 (WO_3/g-C_3N_4) using single-source precursor melamine and tungstate for MO and TC degradation under visible light in 120 min. MO degradation using the pristine catalyst g-C_3N_4 and WO_3 was 38% and 26%, respectively, while the coupling of WO_3 with g-C_3N_4 (W-CN-5) improved the best photocatalytic performance up to 93% for MO and 97% for TC. The mineralization (TOC) of MO (at 120 min was 52.9%) and TC (at 120 min was 56.6%) over the photocatalysts (W-CN-5) was much larger than that of pristine WO_3 (15.7%) and g-C_3N_4 (19.3%) for MO and 3 times more than that (18.2%) for g-C_3N_4 for TC, with the highest reaction rate (0.0213 min^{-1}), 5.6 times greater than that of pristine g-C_3N_4 (0.0038 min^{-1}) for MO using W-CN-5. These results favor the coupling of g-C_3N_4 and WO_3, which promote the photocatalytic activity and mineralization to degrade organic pollutants. MO degradation compared to TC using the same catalyst may be due to the different molecular structures of MO (organic dye) and TC (antibiotic compound) and can influence their degradation kinetics rates. The presence of specific functional groups, aromatic rings, or chemical bonds in TC may make it more susceptible to degradation than MO.

Chang F.[108] also synthesized various combinations of WO_3/g-C_3N_4 binary composites by a facile one-step calcination

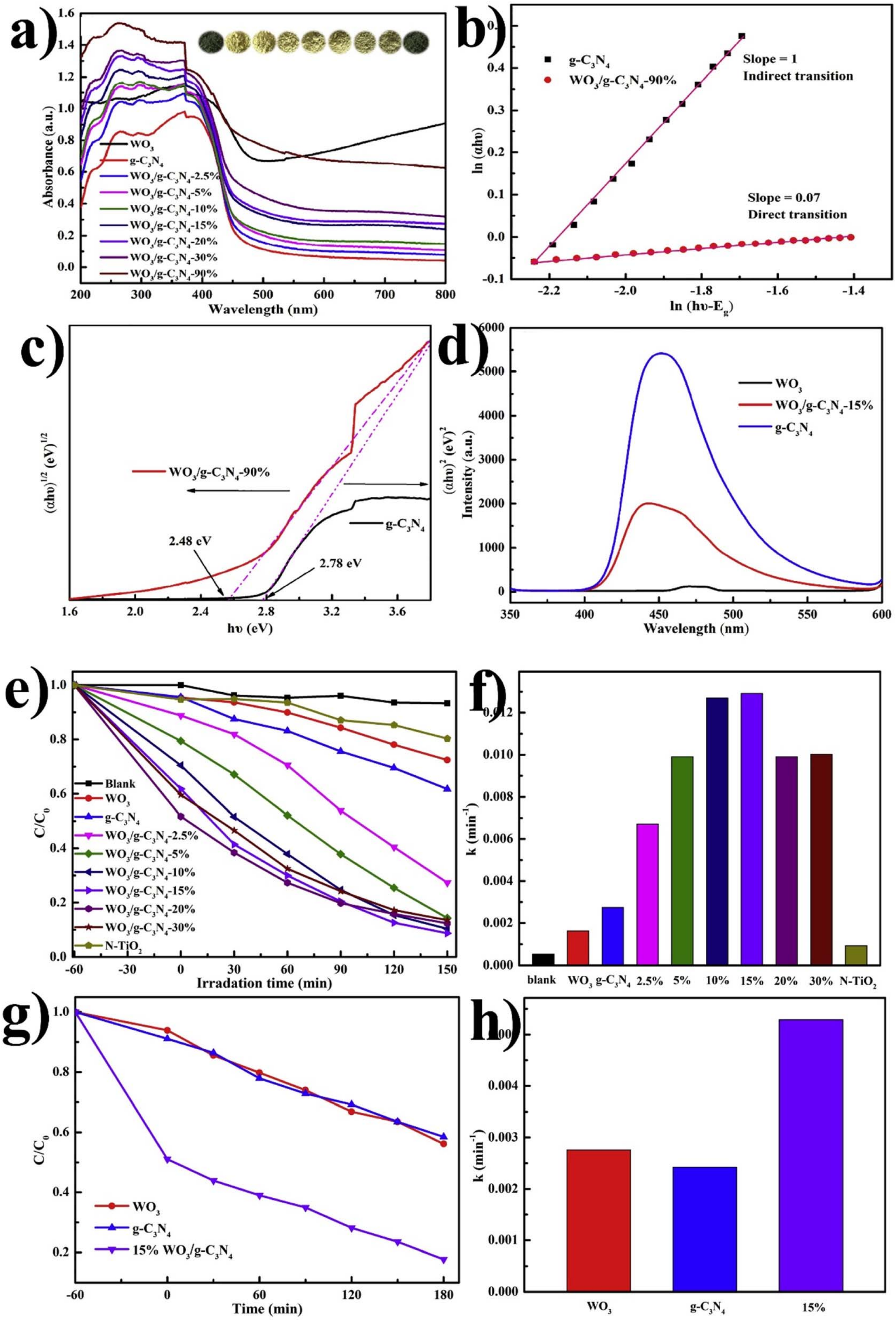

Fig. 10 (a) UV-Vis DRS spectrum of bare WO_3, g-C_3N_4, and binary series, (b) color variation in samples in the inset, ln($\alpha h\nu$) *vs.* ln($h\nu - E_g$) plot, (c) $(\alpha h\nu)^2$ or $(\alpha h\nu)^{1/2}$ *versus* E_g plot, (d) photoluminescence spectra of pristine WO_3, g-C_3N_4, and composite WO_3/g-C_3N_4 (e) photocatalytic degradation of RhB, (f) apparent rate constants (k) for RhB, (g) photocatalytic degradation of MB, and (h) corresponding k values (reproduced with permission from ref. 108 Copyright 2018, Elsevier).

procedure and applied them for RhB and MB photocatalytic degradation. The UV DRS spectra of the pristine and composite are shown in Fig. 10(a). The band energies of $WO_3/g\text{-}C_3N_4$-90% and $g\text{-}C_3N_4$ were estimated to be 2.48 eV and 2.78 eV, respectively. As shown in Fig. 10(b), the slopes of pristine $g\text{-}C_3N_4$ and $WO_3/g\text{-}C_3N_4$-90% were calculated as 1 and 0.07, respectively, suggesting indirect and direct transitions. The photoluminescence (PL) spectra in Fig. 10(d) demonstrate the suppressed recombination rate of charge carriers in $WO_3/g\text{-}C_3N_4$ compared to the pristine form. Suppressed recombination rate indicates higher degradation efficiency. Significantly, all binary hybrids composite showed higher photocatalytic efficiencies over RhB and MB than bare WO_3 and $g\text{-}C_3N_4$, as shown in Fig. 10(e and f) under visible light ($\lambda \geq 420$ nm). The photocatalytic performance of composites increased with the WO_3 contents by up to 15% but decreased beyond that. This behavior was attributed to the optical competition between WO_3 and $g\text{-}C_3N_4$ components or the potential disruption of heterojunction structures. $WO_3/g\text{-}C_3N_4$ (15%) can degrade about 91.3% of RhB after 150 min and exhibits the largest *k* value of about 0.0127 min^{-1}. Similarly, MB degradation under visible light irradiation was also checked by $WO_3/g\text{-}C_3N_4$, demonstrating significantly improved photocatalytic efficiency and relatively large *k* value; the trapping agent detection was also performed, as shown in Fig. 10(g and h). The first limitation of this synthesized photocatalyst is its 150 min degradation time. The second limitation is that this catalyst completely degrades RhB but does not completely degrade MB simultaneously. The possible reason because the degradation of dyes (Rhodamine B and Methylene Blue) depends on various factors (chemical structures, environmental conditions, degradation mechanisms). RhB has a more complex structure with multiple functional groups, making it more susceptible to degradation by environmental factors (reactive chemicals, light, heat). At the same time, MB has a relatively simpler structure (which may contribute to its higher stability). RhB is sensitive to light, especially in the presence of oxygen, and can undergo photobleaching (results in a loss of color). MB is also susceptible to photodegradation; however, its degradation rate may be slower than RhB.

Researchers also used $WO_3/g\text{-}C_3N_4$ for the degradation of other drugs and dyes, desulfuration, and selective oxidation: Ma *et al.*[109] designed a WO_3/few-layer $g\text{-}C_3N_4$ photocatalyst through the *in situ* calcination method for the oxidative desulfurization activity of Model oil (DBT, 4,6-DMDBT, 4-MDBT, and 3-MBT) at different temperatures from 0 °C to 60 °C. The sulfur removal efficiency was 100% at 50 °C at different intervals. The order of desulfurization activity can be listed as DBT > 4-MDBT > 4,6-DMDBT. Priya *et al.*[110] successfully applied the same catalyst, 3 wt% $WO_3/g\text{-}C_3N_4$, for acid orange 7 (AO7) degradation. The degradation efficiency was 100% using 3 wt% $WO_3/g\text{-}C_3N_4$. Reactive species were detected by introducing the radical scavengers into the reaction solution. Ammonium oxalate (AO) employs holes (h^+) detection, and to remove benzoquinone (BQ) and hydroxyl radicals, isopropanol was used to reduce the level of oxygen radicals (O_2^-). The result shows that the holes (h^+) do not significantly affect photodegradation. However, IPA and AO exhibited a quick decrease in the degradation efficiency, revealing the role of superoxide (O_2^-) and hydroxyl radicals in the degradation using 3 wt% $WO_3/g\text{-}C_3N_4$. Zhu Ma *et al.*[56] developed and employed $WO_3/g\text{-}C_3N_4$ using a facile hydrothermal method. (WCN) heterogeneous antibiotics degradation of sulfamethoxazole (SMX) increased to 91.7% when the optimized material WCN8 was applied at a concentration of 1.0 g L^{-1}. Moreover, the photocatalytic performance inhibited both low pH (pH at 3) and higher pH (pH at 7 and 9), while better photocatalytic activity was obtained without pH adjustment. Another study was successfully carried out by Zhao *et al.*[111] using $WO_3/g\text{-}C_3N_4$ to desulfurize model oil thiophene and dibenzothiophene using an ionic liquid with the assistance of oxidizing agent H_2O_2 and observed that the 36% $WO_3/g\text{-}C_3N_4$ composite showed improved performance and crystallinity. The removal rate of sulfur for model oil comprising DBT reached 91.2% with H_2O_2 at 60 °C for 180 min by the 36% $WO_3/g\text{-}C_3N_4$ composite. Navarro *et al.*[112] used $WO_3/g\text{-}C_3N_4$ for the degradation of Orange G (OG) dye and ciprofloxacin (CF). 5% $WO_3/g\text{-}C_3N_4$ degraded 98% (OG) and 100% (CF) as compared to bare $g\text{-}C_3N_4$ (40% degradation of OG, 60% degradation of CF) and bare WO_3 (14% degradation of OG, 19% degradation of CF).

The $g\text{-}C_3N_4/WO_3$ composite degrades when synthesized and combined in appropriate amounts since an optimum content of $g\text{-}C_3N_4$ into WO_3 can facilitate the partition of the electron-opening pair. On the other hand, the doping of $g\text{-}C_3N_4$ ends up higher than the limits, the space-charge region winds up thin, and the irradiation of light on WO_3 greatly surpasses the space-charge layer. This impact may induce prompt and less-demanding recombination of electron openings, bringing down photocatalytic degradation. Despite the improved photocatalytic activity of $WO_3/g\text{-}C_3N_4$, this photocatalyst may still have limitations regarding quantum efficiency, synthesis, and cost. During charge transfer processes or recombination of photoinduced electrons and holes, some energy loss may occur, reducing the overall efficiency of $WO_3/g\text{-}C_3N_4$. Synthesis of the $WO_3/g\text{-}C_3N_4$ composite may involve complex procedures and sometimes requires specific conditions, making its production challenging and time-consuming. This type of complexity can limit the scalability and widespread application of the $WO_3/g\text{-}C_3N_4$ composite. The cost of $WO_3/g\text{-}C_3N_4$ and raw materials used for this composite can be relatively high, and this cost factor can hinder its large-scale commercial applications.

Generalized mechanism for photoexcited e^-/h^+ separation in $WO_3/g\text{-}C_3N_4$. Two types of mechanisms are described in the literature for the photoexcited e^-/h^+ separation of $WO_3/g\text{-}C_3N_4$; (a) Z scheme and (b) S scheme heterojunctions. For the first time, Chen *et al.* studied the separation of photogenerated e^-/h^+ pair for $WO_3/g\text{-}C_3N_4$ photocatalysts. Fig. 11(a and b) shows the bandgap mechanism for WO_3 and $g\text{-}C_3N_4$ and the separation of the photoexcited e^-/h^+ process in two different ways. Charge carriers such as holes of WO_3 migrate from the valence band (VB) to the valence band of $g\text{-}C_3N_4$. Similarly, electrons from the conduction band (CB) of $g\text{-}C_3N_4$ migrate from the conduction band of WO_3; they cannot reduce O_2 into $\cdot O_2^-$ radicals. Conversely, the holes in the VB of $g\text{-}C_3N_4$ cannot oxidize OH into $\cdot OH$ radicals. These results show that the mechanism is unsuitable for active species. $\cdot O_2$ and $\cdot OH$. According to this mechanism, there is a quick combination among the photoexcited electrons of WO_3 from the conduction band and photoexcited holes of g-C_3N_4 from the valence band. The electrons from the g-C_3N_4 conduction band contain a high negative potential, reducing molecular oxygen into $\cdot O_2^-$, while the holes from the valence band of WO_3 produce OH radicals. It is confirmed that the Z-scheme photocatalyst mechanism is suitable for generating $\cdot O_2^-$ and $\cdot OH$ radical reactive species. Aslam *et al.*[113] also reported the degradation of rhodamine B (RhB) and described the formation of radicals for pollutant degradation. They reported that pure g-C_3N_4 takes 80 min while WO_3 takes 110 min to degrade RhB. Similarly, the WO_3/g-C_3N_4 composite takes 30 min for RhB degradation, and $\cdot OH/\cdot O_2^-$ free radicals play an important role in RhB degradation under visible light. Water molecules react with photogenerated holes h^+ or $\cdot O_2^-$ radicals at the surface of the photocatalyst and change to hydroxyl groups (OH^-) group. These holes generated in light are utilized by OH^- on the photocatalyst surface and generate$\cdot$ OH radicals. O_2 reacts with photoexcited electrons and is converted to hydrogen peroxide, a strong photodegradation oxidant. $\cdot O_2^-$ radicals can directly react with RhB or produce OH radicals by reacting with photoinduced electrons and hydrogen ions (H^+). $\cdot OH$ radicals are strong oxidants and finally degrade the RhB, confirming the Z-scheme photocatalyst mechanism. The overall reaction is shown in eqn (i), (ii), and

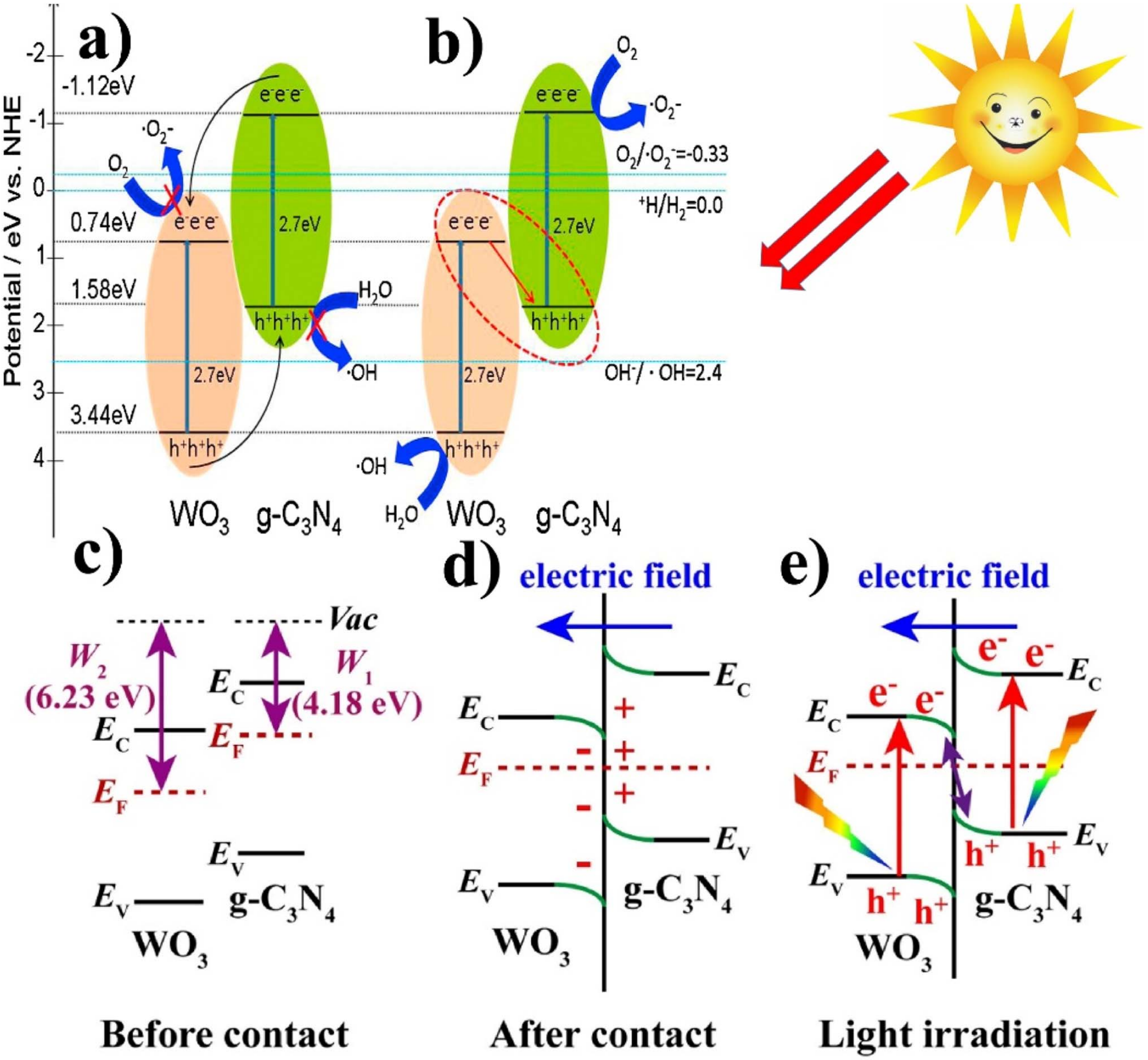

Fig. 11 (a and b) Generalized mechanism of the photoexcited e^-/h^+ separation process of WO_3/g-C_3N_4 (reproduced with permission from ref. 116 Copyright 2014, Elsevier). (c) Before contact with the work functions, g-C_3N_4 and WO_3; (d) after contact at the internal electric field/band edge bending at the interface of WO_3/g-C_3N_4. (e) Under light irradiation, the S-scheme charge transfer mechanism between WO_3 and g-C_3N_4 (reproduced with permission from ref. 82 Copyright 2018, Elsevier).

(iii).[113] The pristine structure does not show good efficiency, while the composite exhibits good efficiency. The main reason behind this is the heterostructure formation, facilitating an easy path to the composite, and promoting the separation of photoinduced charge carriers, ultimately enhancing the photocatalytic activity. Furthermore, the 1D composite can provide a high surface area-to-volume ratio with fewer defects, which is helpful for photodegradation.

$$h^+ + H_2O \rightarrow {*}OH + H^+ \qquad \text{(i)}$$

$$2O_2^{*-} + 2H_2O \rightarrow 2{*}OH + 2OH^- + O_2 \qquad \text{(ii)}$$

$$O_2 + H^+ + 2e^- \rightarrow H_2O_2 \qquad \text{(iii)}$$

Katsumata *et al.*[114] also proposed a photocatalytic mechanism for WO_3/g-C_3N_4 composite, as shown in Fig. 11(a and b). In pristine g-C_3N_4, the photogenerated electrons/holes tend to recombine, which results in low activity because only a small amount (fraction) of them participate in the photocatalytic degradation reaction. Contrary to the pristine from, when the composite of WO_3/g-C_3N_4 contains an optimized content of WO_3 (10 wt%), WO_3 covered a portion of the g-C_3N_4 surface, thus reducing electrons/holes recombination and forming a Z-scheme photocatalytic system.

Aslam *et al.*[113] and Gondal *et al.*[115] favored generic band–band transfer over Z-scheme mechanism. The bandgap value for the conduction and valence band of g-C_3N_4 is 1.57 eV and −1.12 eV, and the bandgap value of VB and CB for WO_3 is 3.18 eV and 0.41 eV, respectively. The potential of the g-C_3N_4 conduction band is lower than the WO_3 CB, which results from the migration of photoexcited electrons from the CB of WO_3 to the CB of g-C_3N_4. In addition, the band structure of the WO_3/g-C_3N_4 composite used in this study can be estimated using the following empirical equations.

$$E_{VB} = \chi - E^e + 0.5E_g \qquad \text{(iv)}$$

$$E_{CB} = E_{VB} - E_g \qquad \text{(v)}$$

where E_{VB} and E_{CB} are the valence and conduction band potentials, χ represents the electronegativity (geometric mean of electronegativity) of the semiconductor, and E^e denotes the energy of free electrons on the hydrogen scale, which is approximately 4.5 eV *vs.* NHE. Similarly, the WO_3 valence band has a higher potential than the g-C_3N_4 valence band, which causes the transfer of photogenerated h^+ from the valence band of WO_3 to g-C_3N_4. The transfer of photoinduced e^-/h^+ pair was carried out through the consecutive reduction of W^{6+} to W^{5+} by capturing the photoinduced e^- at the trapping sites of WO_3. At the same time, W^{5+} is re-oxidized to W^{6+} through O_2 reduction into $\cdot O_2^-$ radicals, which result in the sufficient separation of the photogenerated e^-/h^+ pair and causes a slow-down in the recombination rate.

Nidheesh *et al.*[82] also investigated the photocatalytic mechanism of WO_3/g-C_3N_4 by S-scheme heterojunction. Fig. 11 shows the mechanism (a) before contact with the work functions g-C_3N_4 and WO_3, (b) after contact at the interface of WO_3/g-C_3N_4, internal electric field, and band edge bending, and (c) under light irradiation S-scheme charge transfer mechanism between WO_3 and g-C_3N_4. The band edge of g-C_3N_4 bends upward (loss of electrons), and WO_3 bends the edge downward (accumulation of electrons). After light irradiation, electrons are excited from both photocatalysis (VB to CB). Due to the internal electric field, Coulomb interaction, and band edge (bending), the recombination of a few electrons from the conduction band of WO_3 and holes (h^+) from the valence band (VB) of g-C_3N_4 occurs and also inhibits the recombination of few electrons from the conduction band of g-C_3N_4 and holes (h^+) from the valence band of WO_3. This charge carrier transfer provides supreme redox capacity and helps to carry out the splitting of organic pollutants by providing strong force (S-scheme heterojunction).

Based on the above discussion, it can be inferred that the photocatalytic mechanism of the WO_3/g-C_3N_4 composite does not align with the conventional charge separation process. Specifically, a conventional Z-scheme photocatalyst is preferred for the photocatalytic degradation of organic pollutants. Other researchers have also documented the Z-scheme photocatalytic mechanism of WO_3/g-C_3N_4.[114,117] Table 1 shows a summary of the tungsten-based graphitic carbon nitride composites for several different applications.

Modified WO_3/g-C_3N_4 composites

0D, 1D, 2D, 3D modified WO_3/g-C_3N_4 composites. 1D, 2D, and 3D modified WO_3/g-C_3N_4 nanomaterials are largely used in different applications. Singh *et al.*[119] synthesized the novel coral-like WO_3/g-C_3N_4 nanocomposites by a wet chemical process using WO_3 and g-C_3N_4 for the degradation of Methylene blue (MB) and Remazol brilliant red X-3BS (RbX). SEM analysis was done for the morphology of coral-like WO_3/g-C_3N_4, and Fig. 12(a) presents that the composite WO_3/g-C_3N_4 (1 : 1) structure is similar to coral and has crystallographic particle spacing (0.20 nm and 0.39 nm) and close interface (g-C_3N_4 and WO_3) that allows accelerating the separation of photoexcited carriers. The coral-like structure (irregular and rougher surface) of the composite enhanced its adsorption capacity for pollutant degradation (MB (98%) and RbX (92%)). Fig. 12(b) shows the UV DRS of WO_3/g-C_3N_4 nanocomposites, pure g-C_3N_4, WO_3, and WO_3/g-C_3N_4-1 : 1, showing the absorption range up to 500 nm, 504 nm, and 575 nm, respectively. The WO_3/g-C_3N_4-1 : 1 composite extended the absorption range, appreciably improving the visible light adsorption assisting effective degradation and showing that WO_3/g-C_3N_4-1 : 1 absorbs visible light more effectively and generates more electron–hole pairs, thus effectively enhancing its efficiency. The possible reason could be the combination ratio of 1 : 1, which may result in a synergistic effect arising from improved charge transfer and optimized band structure, where two materials work together more effectively to enhance the degradation efficiency. Deviating from this optimal stoichiometry ratio, such as in the cases of WO_3/g-C_3N_4 (1 : 3) and WO_3/g-C_3N_4 (3 : 1), could disrupt the balance of active sites or alter the electronic properties, leading

Table 1 Summary of WO_3/g-C_3N_4-based material for the photocatalytic degradation of organic pollutants

Precursor	Synthesis method	Parameters	Pollutants	Degradation efficiency	Time	Ref.
$(NH_4)_5H_5[H_2(WO_4)_6]\cdot H_2O$ and dicyandiamide	Calcination, 450 °C	300 W Xe lamp	Methylene blue (MB), 4-chlorophenol (4-CP)	97% (MB), 43% (4-CP)	2 h for MB and 6 h for 4-CP	101
Melamine/$Na_2WO_4\cdot 2H_2O$	Hydrothermal method	250 W Na lamp	Rhodamine B (RhB)	95.3%	2 h	43
Melamine powder, ammonium tungstate	Ball milling, heat treatment	500 W xenon lamp	Methylene blue (MB), fuchsin (BF)	87.9% (MB), 75.6% (BF)	—	104
Melamine, $NaWO_4\cdot 2H_2O$	Hydrothermal	500 W xenon lamp	Rhodamine B (RhB)	99%	30 min	113
Melamine, WCl_6	Calcination	300 W xenon lamp	Methyl orange (MO)	60%	180 min	118
Melamine, WO_3	Thermal decomposing	Fluorescent lamp	Methylene blue (MB)	80%	—	105
Melamine and H_2WO_3	Pyrolysis method	500 W xenon lamp	Rh B and MTBE	62% (RhB), 96.7% (MTBE)	90 min	115
Melamine, $H_3PW_{12}O_{40}$	Calcination	60 °C	Dibenzothiophene (DBT)	91.2%	180 min	111
Melamine, urea, $Na_2WO_4\cdot 2H_2O$	Ultrasonic method	Solar light/400 W xenon lamp	Reactive black 5 (RB5)	98%		48
$[(C_{16}H_{33})_2N(CH_3)_2]_2\ W_2O_{11}$, urea	*In situ* calcination	Thermal (heating)	Dibenzothiophene (DBT)	100%	30 min	109
Urea, H_2WO_3	Wet-impregnation	450 W xenon lamps	Acid orange 7 (AO7)	99%	75 min	110
Melamine $(NH_4)_{10}W_{12}O_{41}\cdot xH_2O$	Calcination method	300 W xenon lamp	5-Hydroxymethyl furfural, 2,5-diformylfuran (DFF)	85.6%	10 h	106

to a decrease in the degradation efficiency. The WO_3/g-C_3N_4-(1 : 1) composite may have a higher surface area and more favorable porosity than other compositions, allowing for more efficient adsorption and reaction of the target pollutants, as shown in Fig. 12(c–f).

Lou *et al.*[121] prepared 1D WO_{3-x} nanowires on 2D g-C_3N_4-NS through a simple solvothermal process. WO_{3-x} nanowires and g-C_3N_4-NS facilitated the charge transfer in WO_{3-x} and g-C_3N_4 (beyond WO_{3-x}/g-C_3N_4-30). Free WO_{3-x} nanowires were created when $W(CO)_6$ concentration in the precursor solution was too high, aggregating the nanowires with no contact with g-C_3N_4 surfaces and lowering the photocatalytic activity. The highest efficiency photocatalyst was applied for the methyl orange (MO) degradation with 90% efficiency in 30 min. 1D/2D g-C_3N_4-NS does not completely degrade MO due to certain structural characteristics or functional groups that make it more resistant or may be due to the presence of electron-withdrawing groups in the molecular structure, which can contribute to its photostability. The intermediate byproducts had lower reactivity and required different reaction conditions for complete degradation, leading to incomplete degradation. Firstly, the abundant oxygen vacancies on WO_{3-x} nanowires contributed to a variation in free electrons and improved the conductivity of WO_{3-x}. Secondly, the WO_{3-x} nanowires exhibited a higher capacity for O_2 adsorption compared to g-C_3N_4 due to the presence of surface oxygen vacancies, thereby promoting charge separation on g-C_3N_4.

Pan and coworker[122] prepared for the first time the novel 2D/2D WO_3/g-C_3N_4 thin photocatalyst through the S-scheme combining carbon (C) with anionic polyacrylamide (APAM) through bridge construction and assistant template, which was named as C-W/N and applied for tetracycline (TC) photodegradation. pH slightly affected the degradation efficiency (82.96%, 84.69%, 87.52%, and 86.33% at pH 3, 5, 7, and 9, respectively). The most efficient photocatalyst C-W/N exhibited 91% photodegradation compared to the other synthesized photocatalysts after 1 h irradiation. WO_3 exhibited the lowest TC degradation, up to 12.14%, due the fast recombination of electron–hole pairs. By adjusting APAM, the photocatalytic efficiency of WO_3 and g-C_3N_4 was promoted. As expected, when WO_3 was combined with g-C_3N_4, it showed better photocatalytic activities than the pristine one. Although constructing 2D–2D WO_3/g-C_3N_4 is an effective approach for photocatalytic degradation, its practical application is still limited due to its stability and durability. Fei Z. *et al.*[123] prepared the photocatalyst WO_{3-x}/2D g-C_3N_4 heterostructure by a single-step calcination process and studied its photocatalytic activity against the degradation and removal of tetracycline (TC), Rhodamine B (RhB), and *S. aureus* under an LED light. Doping with nonmetal oxygen atoms increased the surface area, reduced the bandgap, increased the light-harvesting power, and promoted the transport of charged ions.

Antoniadou and a coworker[124] prepared the novel g-C_3N_4/WO_3 thin films for methylene blue dye removal and hexavalent chromium (Cr^{6+}) reduction. After 2 h under UV-A, almost 70% degradation of MB, 92.87% Cr^{6+} reduction was achieved by g-C_3N_4/WO_3, and 65% degradation of MB, Cr^{6+} reduction was 6.17% realized by WO_3, respectively. C. Xu *et al.*[125] synthesized leaf-like WO_3 nanoflakes decorated on g-C_3N_4 by the facile impregnation and annealing method for benzyl alcohol (BzOH)

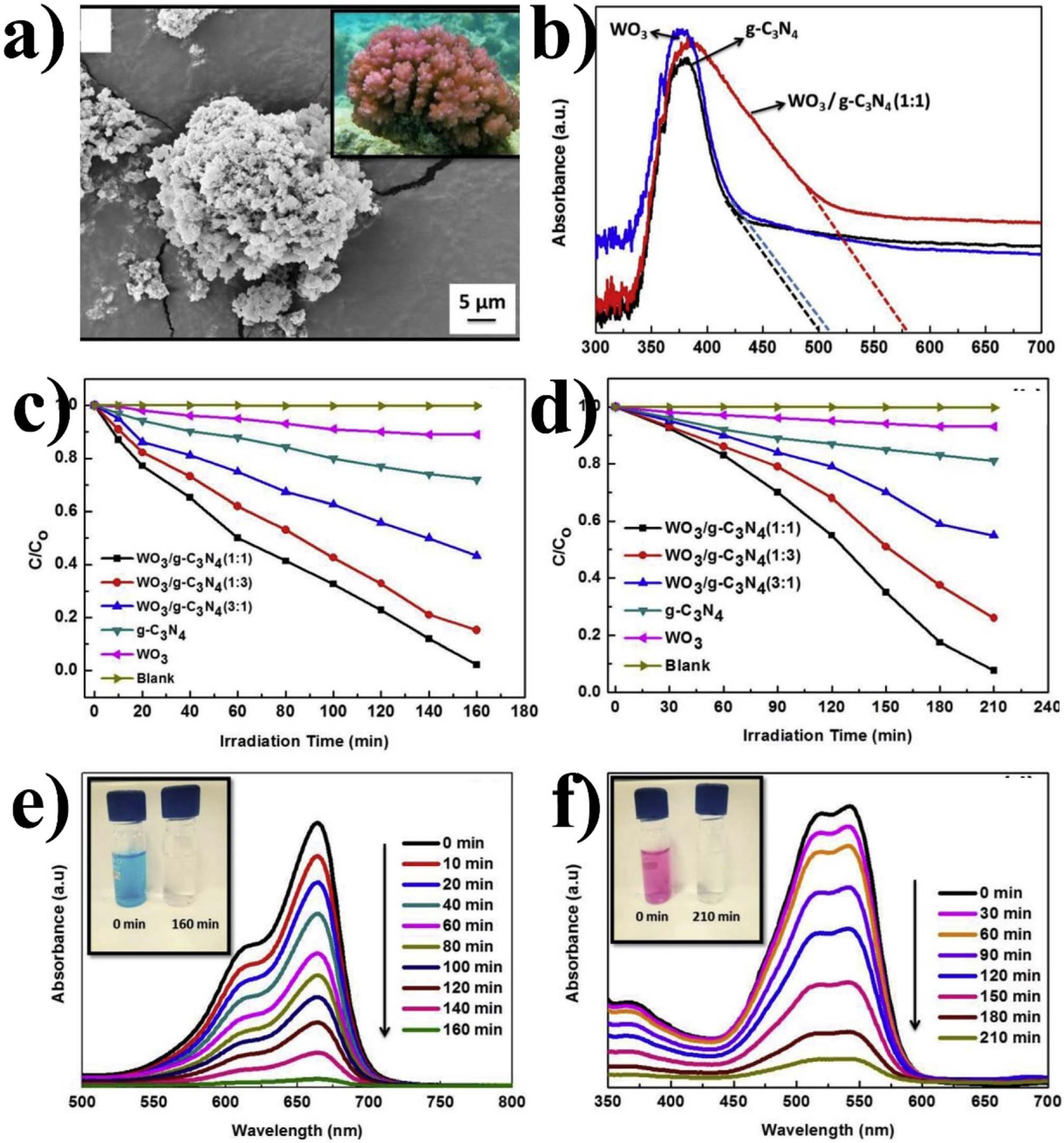

Fig. 12 (a) SEM image of $WO_3/g\text{-}C_3N_4$ (–1 : 1), (b) DRS of $WO_3/g\text{-}C_3N_4$ using various photocatalysts (c) C/C_0 MB and (d) C/C_0 RbX. (e) UV-Vis spectra at different time intervals under visible light for the degradation of MB and (f) RbX using $WO_3/g\text{-}C_3N_4$ (–1 : 1) (reproduced with permission from ref. 120 Copyright 2019, Elsevier).

to benzaldehyde (BzH) conversion, suggesting that no significant conversion was obtained when the experiment was performed at a low temperature (30–50 °C); however, on increasing the temperature up to 80 °C, 98.6% BzOH conversion was observed. Xiao *et al.*[126] constructed $WO_3/g\text{-}C_3N_4$ composite hollow microspheres (CHMs) through the hydrothermal method for the degradation of ceftiofur sodium (CFS) and tetracycline hydrochloride (TC-HCl). The degradation efficiency was 82% for TC-HCl and 70% for CFS within 2 h.

0D, 1D, 2D, and 3D are important in photocatalytic applications.[127] 0D modifications can improve the stability of materials by creating additional active sites, resulting in enhanced catalytic activity. One-dimensional nanomaterials (1D) can enhance the electron transport within the material, leading to improved conductivity and performance, increasing the material's surface area, providing more contact sites for chemical reactions, and enhancing the catalytic activity and efficiency. In two-dimensional nanomaterials (2D), these two dimensions are outside the nanoscale,[128] and 2D modifications (such as graphene-based materials) have a high aspect ratio, which allows for improved mechanical strength and electrical conductivity. Three-dimensional nanomaterials (3D) include bulk powders, dispersions of nanoparticles, bundles of nanowires, and nanotubes, as well as multinano layers that do not have any dimension to the nanoscale and can provide structural support and integrity to the material, making it more robust and resistant to degradation. The 3D structure allows for the efficient mass transport of reactants and products, enabling the better utilization of active sites and improved overall performance. A few disadvantages of these materials include the following: the synthesis techniques may require more complex procedures to obtain well-defined 1D, 2D, and 3D structures, and the synthesis methods for the production of large-scale uniform 2D and 3D structures (control over the morphology and interconnected pore structure in bulk materials) have complex procedures and higher costs. Aggregation in 2D/3D sheets may reduce the active surface area, thus limiting the photocatalytic efficiency. The separation and recovery of 1D, 2D/3D materials from the reaction medium can be difficult, thus impacting the recyclability (Table 2).

Transition metal-doped WO_3/g-C_3N_4 composites. Transition metal has broadly been applied for doping nanomaterials, bringing selectivity and efficiency to nanomaterials. Transition metals such as Ti, Pt, Co, Zn, Pd, Fe, Cu, W, and Zr have been applied to modify the nanomaterials' optical and electronic properties. Doping the transition metal into WO_3/g-C_3N_4 can endow the nanomaterials increased light absorption, low photocorrosion, efficient charge transfer, increased surface area, strong stopping power, chemical stability, and short decay line. The following properties that are mandatory for nanomaterials for photocatalytic applications are optical properties, higher transfer charge/separation, good interfacial contact, larger surface, higher crystallinity, good efficiency, and tandem photooxidation (Fig. 13).

Generally, introducing transition metals can form new energy levels and extend the visible light response from UV to visible region, suppressing the recombination rate of electron–hole (e^-/h^+) charges. In this section, we discuss the transition metal (Ag, Cd, Co, Fe, Cu, Mn, Ni, Zn)-doped WO_4/g-C_3N_4 and their photocatalytic application, and also investigate the binding energies, bandgap reduction, porosity, changes in nanomaterials appearance, and degradation rate after doping transition metals.

Ag-doped WO_3/g-C_3N_4. Vignesh *et al.*[41] first prepared the silver-supported Ag_2WO_4@g-C_3N_4 by the sonochemical impregnation method for methylene blue (MB) degradation, as shown in Fig. 14(a–d). The addition of g-C_3N_4 greatly impacts the stability, surface area, and degradation efficiency of Ag_2WO_4. Ag_2WO_4@g-C_3N_4 (40%) displays 100% MB dye degradation within 120 min. The Ag_2WO_4@g-C_3N_4 (40%) composite amplified the optical property, which gives the advantage for producing reactive oxygen species. With the addition of NaI and BQ scavengers, the photocatalytic activity is strongly suppressed. This shows that the holes (h^+) and oxygen radicals ($O_2^{\bullet-}$) are the principal reactive species for degradation. S_{BET} was determined for g-C_3N_4 (132.48 m^2 g^{-1}), Ag_2WO_4 (1.08 m^2

Table 2 Summary of 0D, 1D, 2D, and 3D modified WO_3/g-C_3N_4 materials against photocatalytic applications with prospective parameters

Precursor	Synthesis method	Parameters	Pollutant/application	Degradation efficiency	Time	Trapping agent	Ref.
Urea, $W(CO)_6$	Solvothermal method	300 W Xe lamp	Orange (MO) degradation	90%	35 min	$\cdot OH$, $\cdot O_2^-$	121
Urea, Na_2WO_3, APAM	Calcination	300 W xenon lamp	Tetracycline (TC)	91%	60 min	$\cdot O_2^-$, h^+	122
Dicyandiamide, $Na_2WO_4 \cdot 2H_2O$, NH_4F	*In situ* strategy	70 W metal halide lamp	RhB	100%	40 min	$\cdot O_2^-$	85
Urea, Pluronic P123, WCl_6	Calcination process	1000 W xenon lamp	Rhodamine B	75%	100 min	$\cdot OH$, $\cdot O_2^-$	129
Melamine, $H_4Na_2O_6W$	Thermally exfoliated	450 W xenon lamp	Phenol	100%	35 min	—	83
Melamine tungsten powder	Calcination	UVA lamps 15 W/BLB	Methylene blue (MB)	70%	120 min	$\cdot O_2^-$, h^+	124
Urea, Na_2WO_4	Wet chemical process	65 W CFL lamp	MB, BR	98% (MB), 92% (BR)	160 min 210 min	OH, $\cdot O_2^-$	119
Melamine, $Na_2WO_4 \cdot 2H_2O$	Impregnation and annealing	—	Benzyl alcohol (BA)	89%	7 h	—	125
Melamine, $(NH_4)_{10}(H_2W_{12}O_{42}) \cdot 4H_2O$	Thermal polymerization	300 W Xe lamp	MO, TC	93% (MO), 97% (TC)	120 min	$\cdot O_2^-$, h^+	107
Melamine, $Na_2WO_4 \cdot 2H_2O$, $Sr(NO_3)_2$	Calcination method	XG500 xenon long-arc lamp	Rhodamine B (RhB)	96%	100 min	OH, $\cdot O_2^-$	130
Dicyandiamide, $Na_2WO_4 \cdot 2H_2O$	Hydrothermal method	300 W xenon lamp	Tetracycline hydrochloride	70%	120 min	$\cdot OH$, h^+	126

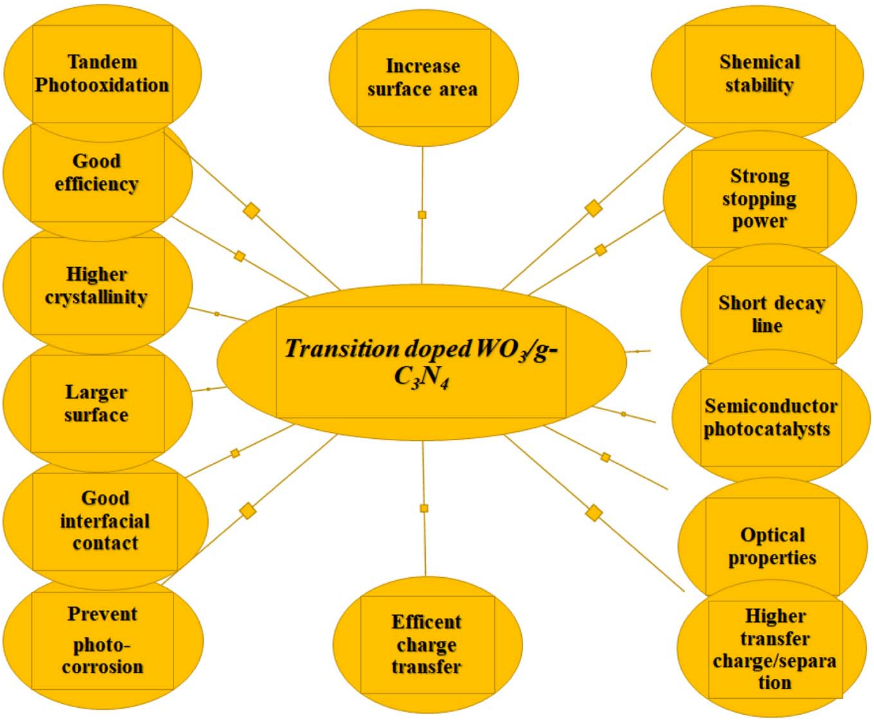

Fig. 13 Properties of $WO_3/g\text{-}C_3N_4$ after doping with transition metals.

g^{-1}), Ag_2WO_4@g-C_3N_4-5% (1.68 m^2 g^{-1}), Ag_2WO_4@g-C_3N_4-10% (2.73 m^2 g^{-1}), Ag_2WO_4@g-C_3N_4-20% (4.07 m^2 g^{-1}), and Ag_2WO_4@g-C_3N_4-40% (6.73 m^2 g^{-1}). The S_{BET} of the composite is less that of pristine g-C_3N_4, which could affect the photocatalytic activity, as shown in Fig. 14(e–h). The introduction of Ag_2WO_4 nanoparticles onto the g-C_3N_4 surface changes the surface morphology and structure, which results in a decrease in S_{BET} compared to pure g-C_3N_4, which implies a reduction in the available surface area for photocatalytic reactions. However, it is important to note that other factors, such as the interfacial interactions and synergistic effects between Ag_2WO_4 and g-C_3N_4, can also influence the photocatalytic performance of the composite, even with a lower S_{BET} value. Similarly, the stability of Ag_2WO_4@g-C_3N_4 under prolonged exposure to light and chemical environments can be a concern, affecting its long-term performance and durability of the materials. However, the photocatalytic efficiency depends not only on the S_{BET} but also on other factors, such as interfacial interactions and synergistic effects, which can influence the photocatalytic performance even with a lower S_{BET} value.

Chen *et al.*[131,132] reported 2D–2D $AgWO_3/g\text{-}C_3N_4$ by solvent evaporation, followed by the *in situ* calcination method for the degradation of dye rhodamine B (RhB) as well as the drug tetracycline (TC). The S_{BET} was measured for g-C_3N_4 (70.13 m^2 g^{-1}), WO_3 (11.95 m^2 g^{-1}), and $AgWO_3/g\text{-}C_3N_4$ (50.62 m^2 g^{-1}). The XPS survey spectrum for the $AgWO_3/g\text{-}C_3N_4$ composite gives the value of C/N/O/W/Ag. In the spectrum of C 1s, the peaks 284.7 eV and 287.9 eV are related to the coordination of N–C=N, and N 1s show three peaks at 398.4 eV, 399.7 eV, and 400.9 eV, indicating the C=N–C, N–(C)$_3$, and amino (NH_2) groups, respectively. For WO_3, the XPS peaks appear at 35.2 eV and 37.3 eV, and the O 1s peak at 529.6 eV indicates O^{2-} in WO_3. The Ag 3d peaks (368.1 eV, 374.2 eV) are attributed to Ag^0. These values indicated that $AgWO_3/g\text{-}C_3N_4$ was successfully synthesized and applied for RhB and TC degradation, which were degraded to 97% and ≈90%, respectively. This data shows that the reported catalyst is most efficient for one dye (97% RhB degradation takes only 40 min), while it is not efficient for the drug (TC ≈ 90% degradation in 140 min). This catalyst is selective only for one pollutant and less efficient for others. This may be because the photocatalysts' efficiency often depends upon the adsorption of pollutants on the catalyst's surface for degradation, and the adsorption capacity depends on its surface area, surface chemistry, and pore structure. Suppose a specific photocatalyst has a high adsorption capacity for a specific pollutant. It can effectively concentrate the pollutant near active sites and enhance the degradation rate of the pollutants for this catalyst, while if the same catalyst has low adsorption capacity for another pollutant, the pollutant may not be efficiently captured by the photocatalyst and is less degraded.

Li *et al.*[133] synthesized the same photocatalyst with some modifications. He prepared ultrathin $Ag_2WO_4/g\text{-}C_3N_4$-NS by a simple deposition–precipitation method for the degradation of methyl orange and Rhodamine B. After irradiation of 20 min in RhB, self-degradation is almost negligible, and $Ag_2WO_4/g\text{-}C_3N_4$-NS, NS-20 (RhB 100%) show higher photocatalytic activities than Ag_2WO_4 and g-C_3N_4-NS, NS-10, NS-30. In NS-30 (30%), further increasing Ag_2WO_4 reduces the photocatalytic efficacy and shows that during the photocatalytic reaction, the mass ratio of Ag_2WO_4 and g-C_3N_4-NS is crucial to the synergistic

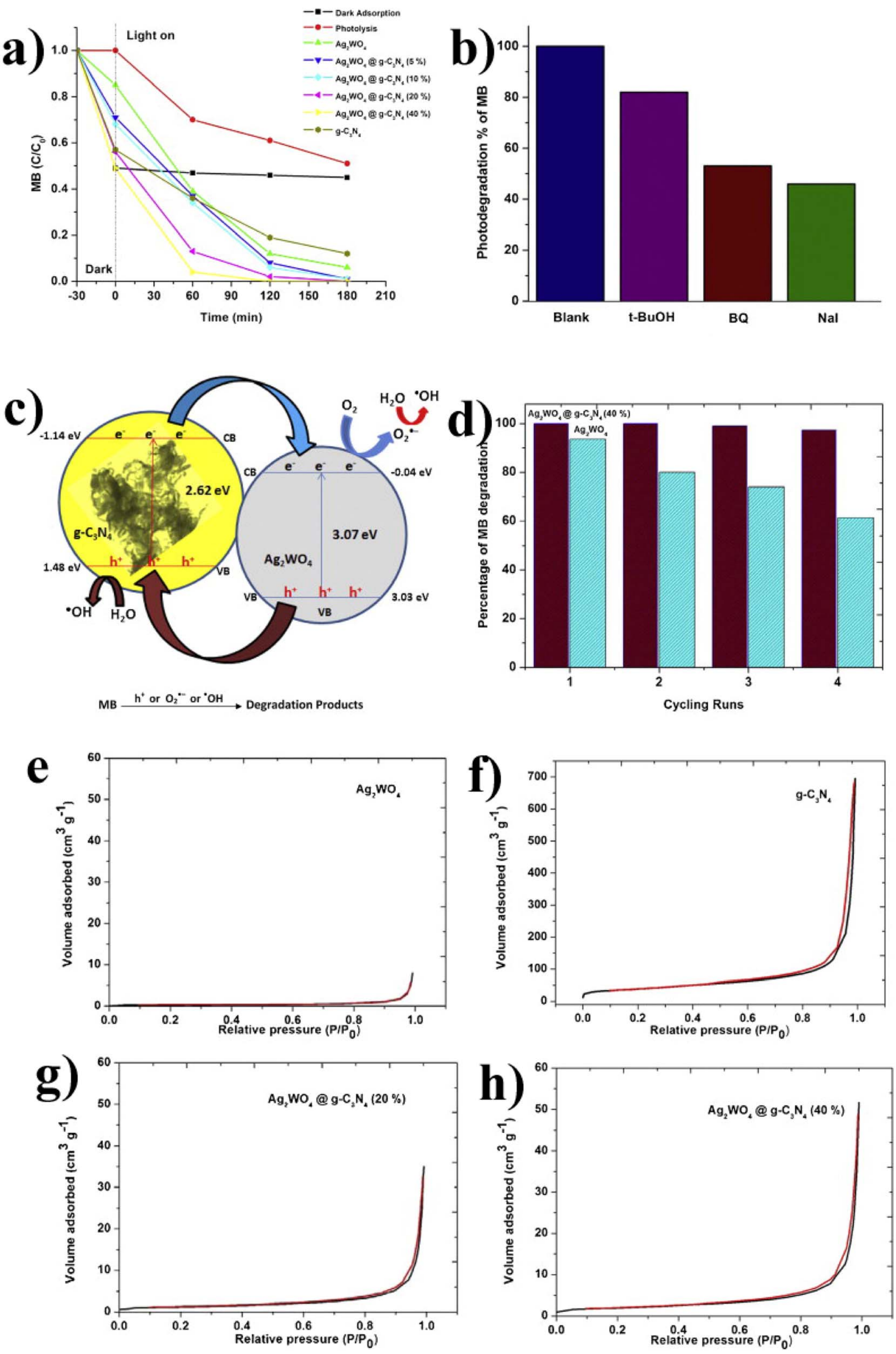

Fig. 14 (a) C/C_0 MB (10 ppm); (b) schematic diagram of electron–hole transfer. (c) Influence of radical scavengers on MB. (d) Cycling runs. (e–h) The N_2 adsorption/desorption isotherms of the pristine Ag_2WO_4, g-C_3N_4, and Ag_2WO_4@g-C_3N_4 composite (reproduced with permission from ref. 41 Copyright 2015, Elsevier).

effects. For comparison, P25, g-C_3N_4-NS, and bulk g-C_3N_4-20 composite were also investigated, and less than 20% RhB could be removed under the same conditions, which has much lower photocatalytic activities than the NS-20 composite. In the absence of photocatalysts, the direct photolysis of MO is almost ignored. After 50 min in visible light, MO (6%) can be removed by Ag_2WO_4, g-C_3N_4-B, and P25 but only 15–30% by B-20 and g-C_3N_4-NS. Under the same conditions, about 85% MO is degraded by NS-20. Under the same experimental conditions, the corresponding kinetic constants (k) for RhB and MO by NS-20 were calculated and displayed. The reaction rate constant for RhB degradation is 0.2180 min^{-1}, 18.9, 53.6, 10.9, and 26.5 times higher than that of Ag_2WO_4, g-C_3N_4-B, g-C_3N_4-NS, and B-20 samples, respectively. Similarly, the MO degradation sample is 0.0394 min^{-1}, 28.4, 30.6, 4.8, and 9.8 times higher than that of Ag_2WO_4, g-C_3N_4-B, g-C_3N_4-NS, and B-20 samples, respectively. The results showed that the novel Ag_2WO_4/g-C_3N_4-NS heterostructures are excellent photocatalytic and can have great photocatalytic activity.

Huang *et al.*[134] synthesized a novel catalyst Ag_2WO_4/P doped g-C_3N_4 (PCN) by single-step thermal polymerization for indomethacin (IDM) degradation. The experimental data shows that 30% (weight percentage) Ag_2WO_4 in the P-doped g-C_3N_4 by composites exhibits excellent photocatalyst efficiency. The BET surface of 30% Ag_2WO_4/PCN was determined to be 61.43 $m^2\ g^{-1}$, and the photocatalytic system's total organic carbon (TOC) removal rate was 51.9%. The IDM degradation rate constants of 30% Ag_2WO_4/PCN were −0.233 per min, 4.59 times greater than that of 30% Ag_2WO_4/CN (−0.0508 per min). There are already a number of the Ag_2WO_4/CN composite used for the degradation of the drugs, but here the purpose of the doping of P into the graphitic carbon nitride may be due to the following reason: P doping in graphitic carbon nitride increases the negative surface charge and can also modify the surface chemistry and morphology of g-C_3N_4. It may enhance the adhesion of Ag^+, which ultimately improves the stability of the phosphorus-doped Ag_2WO_4/CN composite, promotes efficient charge separation, and exposes more active sites. These effects contribute to the composite material's overall photocatalytic activity and performance in pollutant degradation. The overall summary is that the unique properties of Ag_2WO_4 (narrow bandgap, excellent photocatalytic capability) and complement characteristics of g-C_3N_4 offers a stable π-conjugated structure (promotes efficient charge separation), which enables the composite for the effective utilization of solar energy and enhancing the overall photocatalytic activity.

Cd-doped WO_3/g-C_3N_4. Tian *et al.*[135] first reported a novel $CdWO_4$/g-C_3N_4 composite prepared by calcination for Rhodamine B (RhB) degradation. The degradation efficiency of 1 : 10 $CdWO_4$/g-C_3N_4 nanomaterials for RhB is maximum, with the highest rate constant value ($k = 0.164\ h^{-1}$) in the visible spectrum region. These degradation efficiency values are 1.6 and 54.6 times greater than that of pure g-C_3N_4 and $CdWO_4$, respectively. SEM analysis data of $CdWO_4$ shows that it consists of nanorods with 50–100 nm length and 20–50 nm width. The TEM analysis for pure $CdWO_4$ shows a clear fringe with 0.301 nm interval, which forms the (1 1 1) lattice plane ($CdWO_4$ monoclinic). Active species trapping experiments were carried out using EDTA and IPA, showing the existence of $h^+/{\cdot}OH$ species, which plays a major role in the photocatalytic mechanism. The PL emissions of $CdWO_4$ and Cd/g-C_3N_4 composites were observed in the 480–500 nm visible range. The PL $CdWO_4$/g-C_3N_4 exhibited the lowest intensity, showing its lowest recombination. The possible reason behind this may be due to the reason that g-C_3N_4 and $CdWO_4$ have different bandgap energies, and the energy levels of $CdWO_4$ and g-C_3N_4 (after being combined in the composite) can align in a way that favors charge transfer and inhibits recombination. This alignment will facilitate the efficient migration of the photoexcited e^-/h^+ toward the respective energy levels (in $CdWO_4$, g-C_3N_4) and minimize the recombination of the photoexcited e^-/h^+, resulting in a reduced PL signal.

Maavia *et al.*[136] synthesized the same catalyst (g-C_3N_4/$CdWO_4$) through the hydrothermal method and used it for minocycline (MC) degradation with bandgap energies calculated for $CdWO_4$ (3.31 eV), g-C_3N_4 (2.67 eV), and g-C_3N_4/$CdWO_4$ (2.71 eV). The FTIR spectra of $CdWO_4$ provide information about three types of peaks. The two peaks at 522 cm^{-1} and 594 cm^{-1} are the bond stretching vibrations modes of Cd–O, and the peaks at 711 cm^{-1} and 820 cm^{-1} indicate W–O and Cd–O–W, respectively. The UV-visible spectra results show that g-C_3N_4 has an absorption at 460 nm and $CdWO_4$ at about 380 nm. But the g-C_3N_4/$CdWO_4$ composite shows an increase in the absorption peak intensity from 455 to 470 nm, and this g-C_3N_4/$CdWO_4$ composite shows better degradation than pristine materials, may be due to the reason that g-C_3N_4 has good absorption capacity in the visible range, while $CdWO_4$ absorbing UV light and by combining, g-C_3N_4/$CdWO_4$ can effectively utilize both UV and visible light; this broad spectrum range allows g-C_3N_4/$CdWO_4$ to degrade the pollutants efficiently. In short, combining the two materials (g-C_3N_4 and $CdWO_4$) creates a unique interface, promoting the surface reactions or photocatalytic activity. These prominent factors contribute to its superior photocatalytic performance and make it a promising material for various applications in photocatalysis.

Co-doped WO_3/g-C_3N_4. Xing *et al.*[137] reported for the first time Co-doped WO_3/g-C_3N_4 by the precipitation and calcination method at 400 °C for the deep sulfurization of fuel oil (dibenzothiophene (DBT), benzothiophene (BT), and thiophene (TH)), suggesting that the temperature for calcination is an important factor for catalytic performance. They prepared the desired photocatalyst at various temperatures such as 250 °C, 300 °C, 350 °C, and 400 °C. CoWO_3/g-C_3N_4 calcined at 400 °C has the highest desulfurization rate (92% DBT degradation) than the other prepared catalysts. Layered g-C_3N_4 can split into fragments (pieces) at 400 °C, resulting in a larger surface and higher crystallinity. The synthesis temperature is crucial in determining the photocatalyst's structural, physical, and chemical properties, especially in graphitic carbon nitride. At higher temperatures, such as 400 °C, the g-C_3N_4 material tends to have a more ordered and crystalline structure. Similarly, the temperature during the synthesis affects the degree of polymerization of g-C_3N_4, and higher temperatures promote higher degrees of polymerization, resulting in larger g-C_3N_4 domains and improved interfacial interactions between the layers. This can improve the charge carrier mobility, efficient charge separation, and reduced charge recombination during the photocatalytic processes. This can provide a favorable environment for charge transport and facilitate the efficient utilization of photoexcited electrons and holes, thus enhancing the overall photocatalytic performance. These factors contribute to enhanced photocatalytic efficiency. If we look at the same time, the reaction at lower temperatures, WO_3 and g-C_3N_4, do not fully react at lower calcination temperatures; thus, the catalytic performance is low. Increasing the temperature for the synthesis beyond the limit results in the crystal phase transition of the active constituent and decomposition of g-C_3N_4 into the carbon.

Prabavathi *et al.*[138] reported that $CoWO_4$/g-C_3N_4 nanomaterials were successfully fabricated by the hydrothermal method, followed by ultrasonication, and used for norfloxacin degradation. For the chemical bond information (Fig. 15(a)), the XPS analysis of a high-resolution spectrum of the Co 2p shows two peaks at 780.4 and 793 eV, which are related to Co $2p_{3/2}$ and Co $2p_{1/2}$, respectively, or it could be attributed to a +2 state and bandgap energy of $CoWO_4$ (2.2 eV), g-C_3N_4 (2.71 eV), and $CoWO_4$/g-C_3N_4 (1.85 eV), as shown in Fig. 15(b). The electron transport resistance (R_{cr} kΩ) values are $CoWO_4$/g-C_3N_4 (9.34), $CoWO_4$ (42.50), and g-C_3N_4 (47.11), which shows that $CoWO_4$/g-C_3N_4 has less charge transfer resistance and good interfacial contact than the other two (Fig. 14(c and d)). The norfloxacin degradation rate/first-order rate constant k at 80 min was observed for g-C_3N_4 nanosheets (~51.2%, 0.0089 S^{-1}), $CoWO_4$ (~57%), and $CoWO_4$/g-C_3N_4 (91%, 0.0283 S^{-1}, 0.0105 S^{-1}). The efficiency of $CoWO_4$/g-C_3N_4 is about 3.181, 2.691 times greater than that of g-C_3N_4 nanosheets and $CoWO_4$ nanorods, as shown in Fig. 14(e and f).

Sahoo *et al.*[139] designed $CoWO_4$-modified g-C_3N_4 nanocomposite by the reflux-calculation method for ciprofloxacin (CIP) degradation. UV-Vis diffuse reflectance analysis (UV-DRS) was conducted for the optical response of $CoWO_4$-modified g-C_3N_4 nanocomposite, and a characteristic absorption band was observed at 580 nm. The photoluminescence spectrum (PL) emission spectra of g-C_3N_4 and $CoWO_4$/g-C_3N_4 at 440 nm (strong emission band) because due to the recombination of the band–band charge carrier. Similarly, the degradation rate of 57% for CIP by $CoWO_4$ and 81% for $CoWO_4$/g-C_3N_4 in 60 min was observed. During the trapping experiment, superoxide and hydroxide radicals were the main factors for the degradation of CIP. The above summary and results are in favor of the $CoWO_4$/g-C_3N_4 composite, which can offer enhanced surface reactivity compared to the pristine catalyst because the combination of $CoWO_4$ and g-C_3N_4 creates a unique interface between them and promotes the surface reactions and catalytic activity. Besides these, the $CoWO_4$ nanoparticles on the surface of g-C_3N_4 increase the active sites available for photocatalysis, leading to improved photocatalytic efficiency and higher degradation rates of the pollutants.

Fe-doped WO_3/g-C_3N_4. According to our knowledge, the first synthesis of the g-C_3N_4/$FeWO_4$ nanorods was done by the hydrothermal method.[140] Dadigala *et al.*[141] also successfully prepared $FeWO_4$/g-C_3N_4 through a solvothermal *in situ* self-assembly method for the catalytic degradation of tetracycline (TC) and Rhodamine B (RhB). SEM analysis of pure $FeWO_4$ exhibited spherical shapes (diameter 10–20 nm). HRTEM analysis also shows the lattice spacing (0.326 nm of g-C_3N_4) and lattice fringe (0.37 nm $FeWO_4$). The peaks of XPS at 723.9 eV and 710.4 eV are attributed to the binding energies of $2p_{1/2}$ and $2p_{3/2}$. Pure $FeWO_4$ showed absorption over a large UV-visible spectral region in UV-Vis DRS analysis. After the doping of g-C_3N_4 nanosheets with $FeWO_4$, the nanosheets showed good absorption in the visible region relative to pure g-C_3N_4 nanosheets, and with an increase in the $FeWO_4$ content, the optical properties of nanosheets was further enhanced. Two methods for synthesizing the g-C_3N_4/$FeWO_4$ are hydrothermal method and solvothermal *in situ* self-assembly. In the hydrothermal method, g-C_3N_4/$FeWO_4$ nanorods were prepared by subjecting the precursors to high temperature and pressure in an aqueous solution, and this method allows for the controlled growth of nanorods and facilitates the integration of g-C_3N_4 with $FeWO_4$ during the synthesis process, while the solvothermal *in situ* self-assembly method involves the simultaneous formation of $FeWO_4$ and g-C_3N_4 in a solvent at high temperature. The self-assembly process leads to the integration of the two components at the nanoscale, and the solvothermal *in situ* self-assembly method may have the advantage of a more intimate and distributed arrangement and also allows for enhanced interfacial interactions, leading to superior photocatalytic performance. However, controlling the composite particles' size, shape, and uniformity during the self-assembly process, the disadvantage could be challenging. Besides this, $FeWO_4$/g-C_3N_4 is selective for one pollutant, not for another. For example, it degrades 95% RhB, but tetracycline only degrades 83% due to the different nature of the dyes and drugs and their interaction with $FeWO_4$/g-C_3N_4 with a different condition.

Rashidizadeh *et al.*[142] also synthesized a fabricated heterojunction g-C_3N_4 nanosheet/$FeWO_4$ nanoparticle for tandem photooxidation/Knoevenagel condensation reaction under visible light and O_2 as a green oxidant. Similarly, Choi *et al.*[143] reported the heterostructure $FeWO_4$/g-C_3N_4(FWO/CN) functionalized with the N-doped graphene quantum dots (NGQD) synthesized under the numerous conditions of sonication for the effectual removal of harmful vapors such as 2-butoxyethanol (2BE) and ethylbenzene (EB). C_3N_4/$FeWO_4$ photocatalyst was also synthesized[144] *via* the facile sonochemical method with post-annealing treatment for the reduction of CO_2. Hexangular flowerlike $FeWO_4$ heterojunctions containing g-C_3N_4 photocatalyst were fabricated using the *in situ* growth method.[145] In Fig. 16(a and b), the X-ray diffraction (XRD) patterns of each (g-C_3N_4 and $FeWO_4$) of the composite exhibit the typical diffraction peaks. For pure $FeWO_4$, the peaks at 15.60 (010), 18.81 (100), 23.72 (011), 24.50 (110), 30.50 (111), 31.41 (020), 36.42 (002), 38.30 (200), 41.11(200), 44.22 (102), 45.50 (112), 48.60 (211), 51.81(022), 53.90 (130), 61.50 (221), 65 (113), 68.70 (132), and 71.50 (041) planes of monoclinic $FeWO_4$ (JCPDS card file no. 71-2390). g-C_3N_4 peaks at 12.8 and 27.5° were indexed to the (100) and (002) planes, respectively. The composite g-C_3N_4/

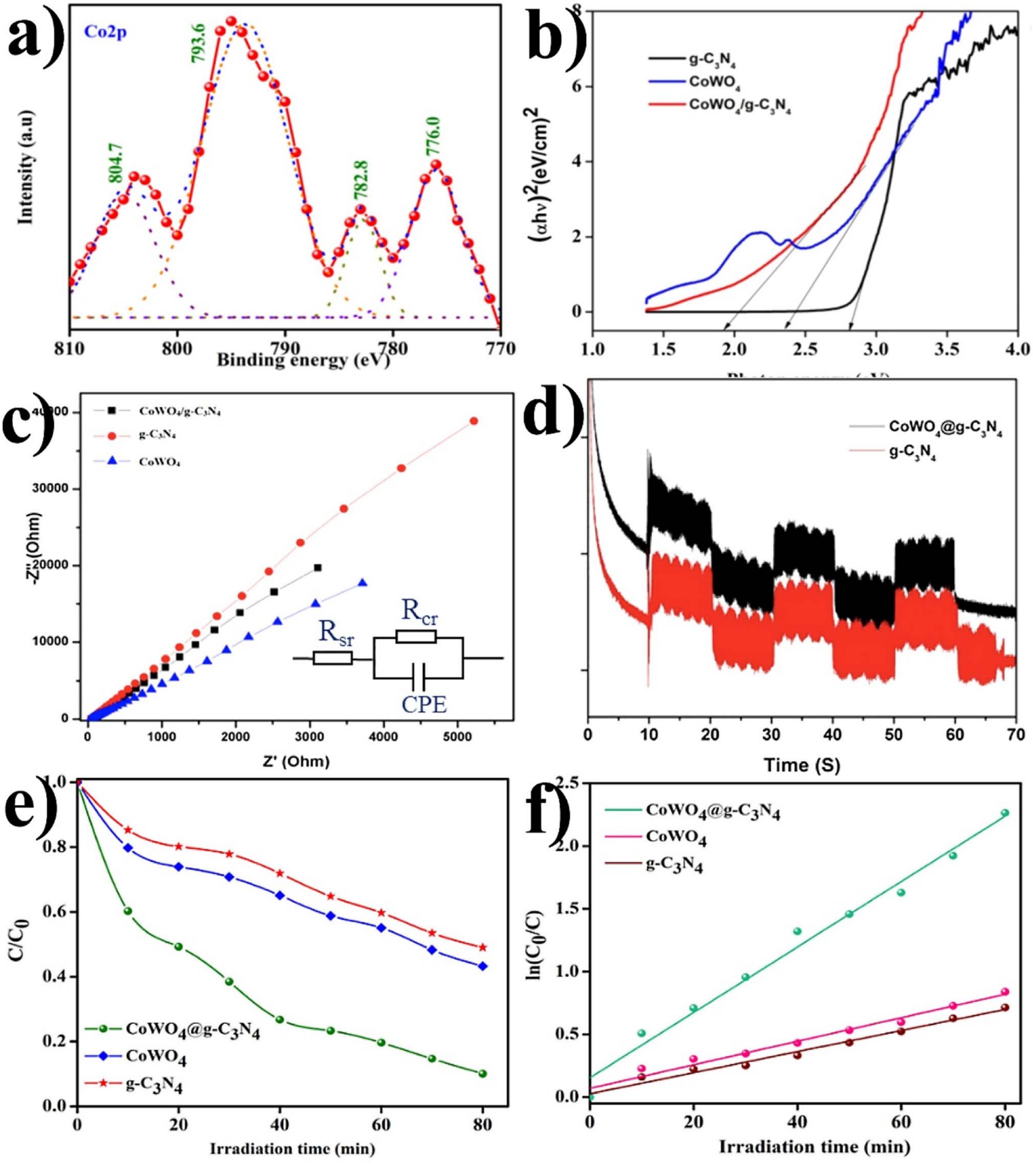

Fig. 15 (a) XPS spectrum of Co 2p, (b) the corresponding Tauc plot. (c) Electrical impedance, (d) transient photocurrent studies, (e) photocatalytic degradation of norfloxacin, (f) corresponding kinetics curves of CoWO$_4$/g-C$_3$N$_4$, CoWO$_4$, g-C$_3$N$_4$, and CoWO$_4$/g-C$_3$N$_4$ (reproduced with permission from ref. 93 Copyright 2019, Elsevier).

FeWO$_4$ (CNU–FW*x*) contains both pristine peaks in the XRD patterns. The FTIR peaks at 834 cm^{-1}, 877 cm^{-1}, and 566 cm^{-1} correspond to the characteristic peaks of the Fe–O–W and Fe–O bond. For thermostability (TGA), bulk g-C$_3$N$_4$ (CNU) exhibited rapid weight loss at 520 °C and at about 700 °C; its degradation was completed (Fig. 16(c)). Similarly, the rapid weight loss of g-C$_3$N$_4$/FeWO$_{4's}$ began at 430 °C and reached 500 °C. The photocurrent response of bulk and optimized materials during five periodical-off cycles is shown in Fig. 16(d) and enhanced the photocurrent response generated for optimized materials (CNU–FW90). Furthermore, a small arc radius of CNU–FW*x* was found in the EIS Nyquist plots, which means that there is

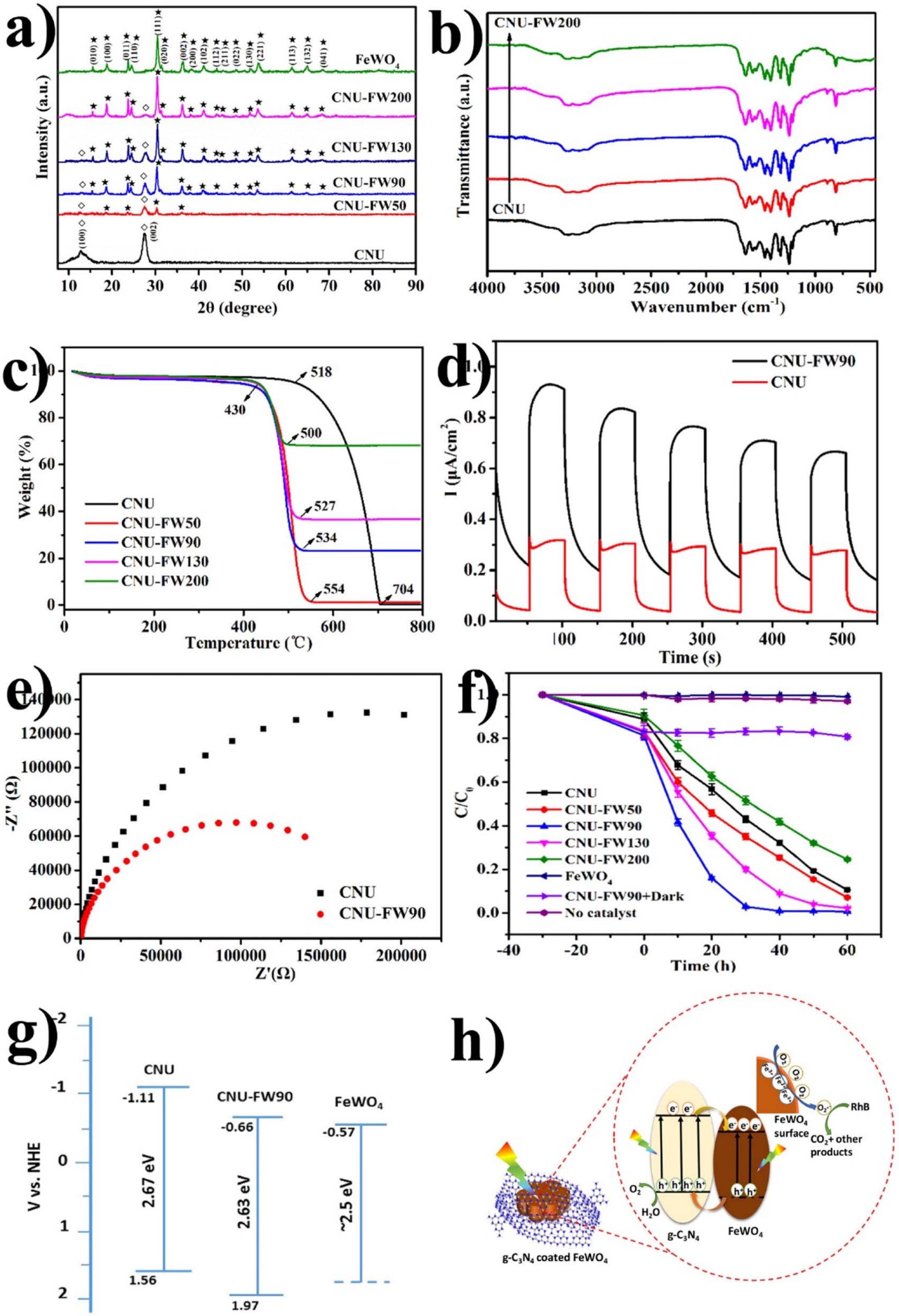

Fig. 16 (a) XRD patterns, (b) FTIR spectrum, (c) TGA profile, (d) photocurrent response, (e) EIS Nyquist plots, (f) photocatalytic activity toward the degradation of RhB, (g) bandgap structures, (h) schematic illustration of the photocatalytic mechanism of g-C_3N_4/$FeWO_4$ (reproduced with permission from ref. 145 Copyright 2018, American Chemical Society).

a lesser recombination of electron–hole pairs among the interface of g-C_3N_4 and $FeWO_4$, as shown in Fig. 16(e). In Fig. 16(f), $FeWO_4$ exhibited poor activity (0.79%) for RhB and $FeWO_4$ coated on g-C_3N_4. An enhancement in the photodegradation of RhB up to 97.2% was achieved in only 30 min. This is because of the arrangement of $FeWO_4$/g-C_3N_4 after composite formation. The close integration between the two materials allows for effective photoexcited (e^-/h^+) migration, reducing the recombination and enhancing photocatalytic activity, as shown in Fig. 16(h). A schematic illustration of the photocatalytic mechanism of g-C_3N_4/$FeWO_4$ is shown in Fig. 16(g). The g-C_3N_4/$FeWO_4$ heterojunction demonstrates a lower valence band (VB) level compared to the pristine by 0.41 V, and a significant difference confirms the enhanced photooxidation ability of the heterojunction since the lower VB level suggests that the heterojunction has a higher capability for accepting and transferring photoexcited holes, which are crucial for driving photooxidation reactions. This unique property of the g-C_3N_4/$FeWO_4$ heterojunction contributes to its stronger photooxidation ability, making it a promising material for various photocatalytic applications.

Cu-doped WO_3/g-C_3N_4. Huang *et al.*[146] synthesized a new Cu^+ self-doped $CuWO_4$/g-C_3N_4 composites (CWO/CN) by *in situ* hydrothermal methods, and the composite with 30 wt% $CuWO_4$/g-C_3N_4 displayed good results for the activation of H_2O_2 to degrade the organic dyes products. The FTIR absorption peaks at 578 cm^{-1}, 700 cm^{-1}, and 800 cm^{-1} display the stretching vibrations of WO_4 and Cu–O. The XPS peaks were obtained at 935.6 eV (Cu $2p_{3/2}$), 955.4 eV (Cu $2p_{1/2}$), and shake-up satellite peaks at 943.7 and 963.0 eV (Cu^{2+}). Similarly, peaks 932.7 and 952.5 eV represent 30 CWO/CN, indicating the Cu^+ oxidation state. The surface area of 30 CWO/CN is 65.1 m^3 g^{-1}, as calculated by BET analysis. The degradation efficiency of RhB was 63.0% in 5 min, nearly 100% after 90 min, and only 7.3% in the absence of H_2O_2 in 90 min. Fenton-like catalytic results showed that H_2O_2 significantly improved the degradation rate of RhB and degraded 91.3% of it in 30 min, with the addition of 40 mmol L^{-1} H_2O_2; at a H_2O_2 concentration of 80 mmol L^{-1}, the degradation rate was decreased. Besides this, methyl orange (81.1%), methylene blue (86.1%), methyl violet (70.9%), and malachite green (82.0%) were also utilized to assess the Fenton-like reaction activity and were degraded within 10 min. The Fenton-like catalytic results demonstrate that the addition of H_2O_2 significantly improves the degradation rate may be due to the reason that H_2O_2 acts as a precursor (generation of highly reactive ·OH radicals) and in the Fenton-like process, H_2O_2 reacts with Fe species to produce ·OH radicals. The combination of Fe and H_2O_2 creates a synergistic effect in the Fenton-like catalytic system, and H_2O_2 continuously supplies ·OH radicals, while Fe acts as a catalyst promoter for the generation and regeneration of ·OH radicals. These ·OH radicals exhibit strong oxidative ability and can effectively degrade organic pollutants because the ·OH radicals have a high oxidation potential and can oxidize a wide range of organic compounds. This synergistic effect enhances the overall degradation efficiency and accelerates the degradation rate of pollutants. Moreover, the catalyst worked at a very high pH, and a very high dose of catalyst was used only to degrade the few ppm solutions in this research work.

Zhou *et al.*[147] synthesized the same photocatalyst $CuWO_4$/g-C_3N_4 by hydrothermal reaction for Rhodamine B (RhB) degradation. The 10%$CuWO_4$/g-C_3N_4 composite displayed the highest degradation efficiency of 93% for RhB within 150 min, and the photodegradation efficiency remains 80% after four cycles, and the reaction mechanism of $CuWO_4$/g-C_3N_4 photocatalyst was fully discussed to according to the formation of the Z-scheme system. The Z-scheme formed may be because $CuWO_4$ and g-C_3N_4 have different energy band structures, and $CuWO_4$ has a narrower bandgap than g-C_3N_4, resulting in the different positions of their VB and CB energy levels. The energy levels of $CuWO_4$ and g-C_3N_4 align in such a way (after the combination of these two composites) that the CB of $CuWO_4$ is higher than the CB of g-C_3N_4, while the VB of g-C_3N_4 is higher than the VB of $CuWO_4$, and this energy level alignment forms the basis for efficient charge transfer and Z-scheme formation. Under the irradiation of light, g-C_3N_4 absorbs light and generates the e^-/h^+ pair. As discussed above, due to energy level alignment, the photoexcited electrons in the CB (g-C_3N_4) is readily transferred to the CB of $CuWO_4$. Here, they are trapped and utilized for redox reactions. Similarly, the h^+ generated in the VB of g-C_3N_4 migrated to the VB of $CuWO_4$, creating a strong oxidation environment. This efficient charge separation and transfer between $CuWO_4$ and g-C_3N_4 form the Z-scheme system.

Mn-doped WO_3/g-C_3N_4. Manganese (Mn)-doped WO_3/g-C_3N_4 heterojunctions were employed for Rhodamine B degradation.[148] The SEM results showed the uniform distribution of flower-like $MnWO_4$ on the g-C_3N_4 surface. HRTEM exhibited the lattice spaces (0.369 nm) of the $MnWO_4$ crystallite. The bandgap value of g-C_3N_4 and $MnWO_4$ is 2.68 eV and 2.46 eV, respectively. The FTIR data of $MnWO_4$ shows that the band at 3400 cm^{-1} and 1600 cm^{-1} correspond to the ν(O–H) and δ(O–H) surface hydroxyl group, respectively. Similarly, a strong band was observed at 455 cm^{-1}, 592 cm^{-1}, 735 cm^{-1}, and 885 cm^{-1} (vibration modes $MnWO_4$). The XPS spectrum of the $MnWO_4$ indicates that peaks at 641.9 eV, 35.17 eV, and 531.9 eV are due to Mn 2p, W 4f, and O 1s. The RhB degradation is 44% using g-C_3N_4 and 10% using $MnWO_4$ (10%) after a 4 h reaction under visible light irradiation. The limitation of this work is that it takes too much time for degradation, and it only degrades 73% after 4 h of irradiation. The reason for poor catalytical activity might be because the hydrothermal method might not provide the ideal conditions (temperature, reaction time, precursor concentration, stirring rate) for the formation of a highly active and well-dispersed $MnWO_4$/g-C_3N_4 composite during the synthesis process, and the lack of these parameters can result in incomplete crystallization, limited interfacial contact, inadequate particle size, and can lower the catalytic activity. By optimizing these factors, the photocatalytic performance of $MnWO_4$/g-C_3N_4 can be improved.

The same material was synthesized with some modifications. 1D/2D $MnWO_4$ nanorods were anchored on g-C_3N_4 nanosheets *via* a one-pot hydrothermal approach for the photocatalytic degradation of ofloxacin (OFX 90.4%), and the calculated bandgap for this material was 2.58 eV.[149] It was experimentally observed that different combinations of the photocatalyst show different photocatalytic activity, for *e.g.*, $MnWO_4$@g-C_3N_4 1 : 0.25 (45%), $MnWO_4$@g-C_3N_4 1 : 0.5 (50.2%), $MnWO_4$@g-C_3N_4 1 : 1 (90.4%), $MnWO_4$@g-C_3N_4 1 : 1.5 (56.8%), and $MnWO_4$@g-C_3N_4 1 : 2 (45%), and when the g-C_3N_4 ratio was increased to 1, maximum degradation was observed due to sufficient interaction, leading to synergy toward OFX degradation. After that, a further increase in the g-C_3N_4 ratio results in lesser degradation efficiency due to the shielding effect among $MnWO_4$ nanorods and OFX molecules. As we know, increasing the ratio of one material to the other material beyond a limit can cause the aggregation of particles within the composite and can also cause a mismatch in electronic and energy levels between the materials. This aggregation reduces the available surface area for catalytic reactions, hinders efficient charge transfer, limits the active sites, impedes the utilization of photoexcited electrons/holes, and hinders the accessibility of the reactants to the catalyst. Consequently, the photocatalyst may experience higher recombination rates and reduce the overall efficiency. Inorganic anions such as SO_4^{2-}, CO_3^{2-}, and Cl^- can also affect the degradation ability of the photocatalysts because of the scavenging properties created by the formation's weak oxidative species. $MnWO_4$/g-C_3N_4 (MWG) hybrid catalysts were synthesized by a facile hydrothermal approach for the degradation efficiency of RhB and 4-CP dyes.[150] MWG3 (3 : 1) displayed the high photocatalytic activity of RhB (98%), high first-order kinetics of 0.0923 min^{-1}, long-term stability, and loss of only 2.8%. The *J–V* characteristics reveal that the $MnWO_4$/g-C_3N_4 photoanode shows high photoconversion efficiency (PCE%) at 7.15% and pure $MnWO_4$ at 2.34%.

When mixed in the proper amount and method, each composite material has optimal stoichiometry, desired synergistic effects, and photocatalytic activity. Deviating from this optimal ratio can disrupt the balance of interactions and hinder the desired functionalities. Similarly, optimizing various experimental parameters (such as catalyst loading, irradiation intensity, and reaction temperature) can enhance the photocatalytic activity.

Ni-doped WO_3/g-C_3N_4. A novel $NiWO_4$/g-C_3N_4 photocatalyst was first synthesized for norfloxacin (NRF) photodegradation under visible light.[151] The designed photocatalyst was synthesized by the hydrothermal method, followed by sonication. Fig. 16(a and b) shows the SEM images of the $NiWO_4$@g-C_3N_4 nanocomposite, consisting of two phases. $NiWO_4$ nanorods were decorated on the surface of the g-C_3N_4 nanosheet. The HRTEM images show the clear lattice fringes (interlayer distance 0.28 and 0.31 nm) of $NiWO_4$ (111) and g-C_3N_4 (110), respectively (Fig. 17(c, d and f)). In the FT-IR spectrum, the strong peaks at 830 cm^{-1}, 615 cm^{-1}, 450 cm^{-1}, and 711 cm^{-1} show the vibration mode of O–W, Ni–O, NiO, and W–O–W, respectively. After deconvolution, the XPS peaks of Ni 2p were observed at two different positions, which were assigned to Ni $2p_{1/2}$ (873.4 eV) and Ni $2p_{3/2}$ (855.6 eV). The Tauc's formula was used to calculate the direct bandgap energy of g-C_3N_4, $NiWO_4$, and $NiWO_4$@g-C_3N_4, which was found to be 2.74, 2.44 eV, and 2.26 eV, respectively. Fig. 17(e) shows that the mean diameter and pore size distribution of $NiWO_4$@g-C_3N_4 nanocomposite was 9.08 $m^2\ g^{-1}$ and 1.8 nm, respectively. The calculated rate constant value for $NiWO_4$/g-C_3N_4, g-C_3N_4, and $NiWO_4$ was 0.0547, 0.0152, and 0.0119, respectively, which revealed pseudo-first-order kinetics. The photocatalytic activity of the catalyst was gradually increased up to 97% within 60 min as the catalyst dosage increased from 10 to 50 mg. But the further increase in the dosage decreases the light penetration ability, resulting in a lesser degradation ability because the higher concentration of the catalyst blocks the incoming light, and no sufficient e^-/h^+ produced resulted in decreased photocatalysts. NRF concentration is also an important factor for degradation efficiency. Using 10 to 30 mg L^{-1} NRF, the degradation rate slowed, possibly due to a lower number of hydroxyl radicals at the photocatalyst surface. IPA, AO, and BQ were used as a scavenger, which retards the photocatalytic activity up to 56%, 65%, and 85%, respectively, which clarified that h^+ and ·OH played the main role in the degradation relative to $\cdot O^{2-}$. The BET for $NiWO_4$@g-C_3N_4 was estimated to be 9.08 $m^2\ g^{-1}$, and BET is not a comparison for other pristine materials. All the points discussing the mechanism of photodegradation above are shown in Fig. 17(g–j).

g-C_3N_4 and $NiWO_4$ were fabricated to establish g-C_3N_4/$NiWO_4$ for the photocatalytic degradation of toluene.[153] The combination of 1C/1N exhibited the highest photocatalytic degradation activity: removal efficiency (95.3%) and mineralization degree (99.1%). The g-C_3N_4/$NiWO_4$ heterojunction absorbs visible light for electron excitation from the CB to VB, and due to the heterojunction, the photoexcited electrons in the CB of $NiWO_4$ combine with the photoexcited holes in the VB of the g-C_3N_4, which provide the maximum amounts of accessible electrons and holes for toluene degradation under visible light. This interface-driven synergy enhances the overall performance of the composite and contributes to its superior catalytic activity in various photocatalytic applications. $NiWO_4$@g-C_3N_4 may face challenges related to stability and durability because the nanocomposite's prolonged usage may undergo structural degradation, chemical leaching, or material loss, leading to reduced catalytic performance and hindering its practical applications.

Zn-doped WO_3/g-C_3N_4. Similarly, a novel heterostructured g-C_3N_4/$ZnWO_4$ (CNZW) nanocomposite was fabricated by hydrothermal methods for Rhodamine degradation.[154] Raman spectroscopy was also performed to understand the binding between g-C_3N_4 and $ZnWO_4$. The peaks at 1345 cm^{-1} and 1581 cm^{-1} correspond to pure g-C_3N_4, and the internal and external vibration modes of the ZnO_6 octahedron and WO_6 octahedron show the Raman modes (275, 356, 415, 702, and 915 cm^{-1}) for pristine $ZnWO_4$. Similarly, the A_{1g} symmetric stretching (~915 cm^{-1}), E_g asymmetric stretching (~702 cm^{-1}), and T_{2g} bending deformation ($2A_g + B_g$, ~415, 356, and 275 cm^{-1}) are correlated to the monoclinic structure of $ZnWO_4$. This result conforms to the formation of the interaction of g-C_3N_4 and $ZnWO_4$. It is observed that the g-C_3N_4/$ZnWO_4$ nanocomposites exhibited lower PL emission intensities than that of pristine $ZnWO_4$ and g-C_3N_4, which is attributed to improved interfacial charge transfer due to superior charge separation,

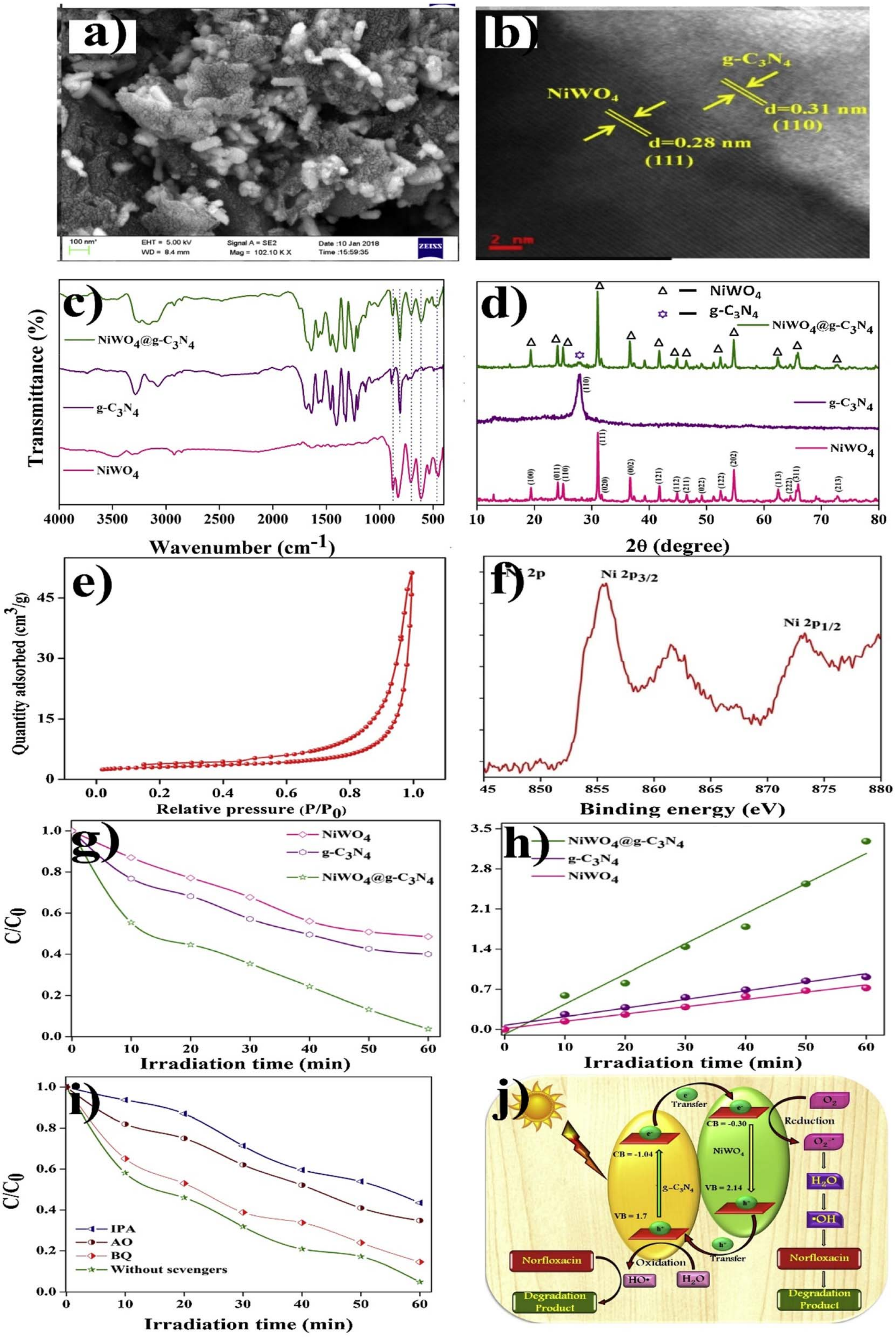

Fig. 17 (a) SEM images, (b) TEM images, (c) FT-IR spectra, (d) XRD, (e) BET, (f) XRD of the NiWO$_4$@g-C$_3$N$_4$ nanocomposite, (g) C/C_0, (h) kinetic study, (i) trapping agent, and (j) mechanism of photocatalytic degradation of NRF by the NiWO$_4$@g-C$_3$N$_4$ nanocomposite (reproduced with permission from ref. 152 Copyright 2019, Elsevier).

which in turn significantly enhances the photocatalytic activity. The photocatalytic ability of the photocatalysts at 80 min follows the order CNZW20 99% > CNZW10 76% > CNZW30 63% > gC_3N_4 44% > $ZnWO_4$ (18%). After recycling, the degradation efficiency of the composite continuously decreases, which means that it is efficient only up to a limit. During the recycling of g-C_3N_4/$ZnWO_4$, nanocomposites may experience surface fouling (due to the deposition of organic/inorganic species) from the reaction mixture, and this fouling creates a barrier that inhibits the reactant adsorption and hinders the photocatalytic performance.

Recently, $ZnWO_3$/g-C_3N_4 (CZW) was reported for phenol degradation under UV irradiation.[155] Their characterization is checked by different techniques such as XRD data, which shows the diffraction angles at 15.30° (0 1 0), 23.78° (0 1 1), 24.25° (0 2 1), 30.56° (1 1 1), and 36.32° (0 0 2). These peaks could be attributed to the structure of the $ZnWO_4$. In the FT-IR spectra, two peaks at 3447 cm^{-1} and 1620 cm^{-1} indicate that the basic hydroxyl groups existed in $ZnWO_4$, and the surface of $ZnWO_4$ was hydroxylated. Similarly, in the XPS data, the binding energies at 1045.1 eV and 1021.7 eV are assigned to Zn^{2+} $2p_{1/2}$ and Zn^{2+} $2p_{3/2}$, respectively. The binding energy values of Zn $2p_{3/2}$ and Zn $2p_{1/2}$ were observed at 1021.7 and 1045.1 eV, respectively, which can be assigned to Zn^{2+} ions in $ZnWO_4$. The BET-specific surface areas were determined for g-C_3N_4 (4.698 m^2 g^{-1}), $ZnWO_4$ (4.698 m^2 g^{-1}), and 5-CZW (21.315 m^2 g^{-1}). The different combinations of photocatalysts show the different degradation efficiency of $ZnWO_4$ (16.8%), 1-CZW (21.8%), 3-CZW (25.4%), 5-CZW (30.4%), 7-CZW (23.2%), and g-C_3N_4 (3.9%).

In transition metal-doped WO_3/g-C_3N_4, the transition metal can improve the photocatalytic efficiency of the composites. Some transition metals can enhance the stability, ensure long-term performance, and extend the composite's lifespan. Moreover, transition metal dopants can modify the electronic structure and band alignment, and this modification facilitates efficient charge separation, reducing electron–hole recombination and enhancing the overall photocatalytic performance. Transition metal-doped WO_3/g-C_3N_4 has potential in various fields such as photocatalytic water splitting to produce hydrogen, solar cell, and CO_2 reduction. Furthermore, it can be employed in energy storage devices, sensors, and optoelectronic devices. However, some disadvantages of this composite are briefly described below: transition metal-doped WO_3/g-C_3N_4 can only be degraded by a limited number of dyes, drugs, and other pollutants because different pollutants possess varying chemical structures and properties, and if a composite is well-suited to the chemical nature of a pollutant, it can form strong bonds, promote reactive species generation, and facilitate degradation. However, pollutants with complex chemical structures may be more challenging for the composite to break down effectively. Moreover, the composite possesses specific active sites that promote photodegradation and activity, and the selectivity of these active sites determines how effectively the composite can interact with pollutants. The composite with high activity can facilitate the conversion of maximum pollutants into less harmful byproducts, but the composite with selectivity can specifically target certain pollutant species. Therefore, the different composite may be designed to target specific pollutants or related pollutant classes, and the degradation depends on a combination of composite properties and pollutant characteristics.

Table 3 presents the transition metal-doped WO_3/g-C_3N_4-based materials for the degradation and removal of various materials with their efficiency.

Ternary-doped modified materials of WO_3/g-C_3N_4 composites. Ternary-doped modified materials of WO_3/g-C_3N_4 enable the exploitation of synergistic effects between the different dopant elements and WO_3/g-C_3N_4 host materials. The presence of multiple dopants can in WO_3/g-C_3N_4 creates a cooperative interaction, and this synergistic effect can include improved charge transfer, enhanced light absorption, and efficient separation of electron–hole pairs, which enhances the overall photocatalytic performance, making them more attractive for various energy conversion and environmental remediation applications. Similarly, various natures of metal oxide nanoparticles and graphene oxide are widely used for many applications due to their good intrinsic properties at domestic and commercial levels. To enhance the properties of g-C_3N_4, its combination with metal oxides such as WO_3, ZnO, TiO_2, and graphene seems more suitable. These composites would lead to new hybrid nanostructured materials and have good photocatalytic properties against various natural constituents such as dyes, drugs, pharmaceutical waste, and pesticides. Photoelectrochemical and electrochemical mechanism-based semiconducting catalysis can oxidize organic pollutants or degrade inorganic pollutants in wastewater.[156]

Currently, dual Z-scheme-based various ternary composites of g-C_3N_4 were synthesized, stimulating the complete transformation of photoexcited electrons and giving high charge separation properties.[157,158] Tang *et al.*[159] synthesized a ternary g-C_3N_4/WO_3/AgI photocatalytic system with a double Z-scheme for neonicotinoid degradation. The developed photocatalyst has an exclusive transmission path for photoinduced charge carriers, thus increasing the photocatalyst's activity. Guo *et al.*[160] prepared a dual Z-scheme Bi_2S_3/$BiVO_4$/$MgIn_2S_4$ nanocomposite heterojunction for the photocatalytic degradation of carbamazepine by the *in situ* growth method. Photoexcited charge carriers have a Z-scheme transformation path, which leads to enhanced photocatalytic activity. These ternary structures contain a better charge transformation path, thus improving the catalyst performance. Hongfei Y. *et al.*[161] fabricated AgBr/β-Ag_2WO_4/g-C_3N_4 dual Z-scheme heterostructure by the precipitation method for tetracycline(TCH) and rhodamine B degradation. The synthesized ternary composite AgBr/β-Ag_2WO_4/g-C_3N_4 (CNAWAB7) degraded the rhodamine by almost 99.2% within just 25 min respective to CN, β-Ag_2WO_4, and composite of both CNAW9. The ternary composite also showed little better results for the degradation of tetracycline (60% within 25 min). The fabricated photocatalyst has better charge separation properties due to the alignment of a band, which mainly improves the photocatalytic performance of the proposed catalyst against TCH and rhodamine. However, catalytic efficiency decreases after every cycle. Mitra M. *et al.*[161] synthesized

Table 3 Summary of transition metal-doped WO_3/g-C_3N_4 materials against photocatalytic applications with prospective parameters

Catalyst	Synthesis method	Parameters	Pollutant/application	Degradation efficiency	Time	Trapping agents	Ref.
Ag_2WO_4@g-C_3N_4	Sono-chemical impregnation	150 W xenon arc lamp	MB	100%	120 min	h^+, $O_2^{\bullet -}$	41
$AgWO_3$/g-C_3N_4 2D/2D heterostructure	Solvent evaporation and *in situ* calcination	XG500 xenon long-arc lamp	RhB TC	96% (RhB), ≈90% (TC)	40 min, 140 min	$O_2^{\bullet -}$, ·OH	131
Ag_2WO_4/P doped g-C_3N_4	Single-step thermal polymerization	350 W xenon lamp	Indometacin orange (MO)	52%	15 min	$O_2^{\bullet -}$	134
$CdWO_4$/g-C_3N_4	Mixed-calcination method	500 W xenon lamp	Rhodamine B (RhB)	≈45	4 h	·OH, h^+	135
g-C_3N_4/$CdWO_4$	Hydrothermal process	250 W xenon lamp	Minocycline (MC)	86%	5 h	·OH	136
$CoWO_4$/g-C_3N_4	Hydrothermal method	Tungsten–halogen	Norfloxacin (NF)	91%	80 min	·OH	138
g-C_3N_4/$FeWO_4$	Solvothermal method	Sunlight	RhB, TC	99% (RhB), 88% (TC)	90 min	$O_2^{\bullet -}$, ·OH	141
$CuWO_4$/g-C_3N_4 heterojunction	Hydrothermal method	500 W xenon lamps	Rhodamine B (RhB)	93%	150 min	$O_2^{\bullet -}$, ·OH	147
$MnWO_3$/g-C_3N_4 heterojunction	Facile hydrothermal method	250 W xenon lamp	Rhodamine B (RhB)	73%	4 h	$O_2^{\bullet -}$, ·OH	148
1D/2D $MnWO_4$ nanorods on g-C_3N_4	One-pot hydrothermal	150 mW cm^{-2} tungsten lamp	Ofloxacin (OFX)	90%	70 min	h^+, $O_2^{\bullet -}$	149
$MnWO_4$/g-C_3N_4 hybrid	Hydrothermal method	Xenon lamp XQ-500 W	RhB, 4-CP	98% (RhB), 91% (4-CP)	100 min	·OH	150
$NiWO_4$ nanorods anchored on g-C_3N_4	Hydrothermal method	Tungsten lamp (150 mW)	Norfloxacin (NRF)	97%	60 min	·OH, h^+	151
g-C_3N_4/$NiWO_4$	Hydrothermal	1000 W Xe	Toluene	95%	180 min	·OH	153
g-C_3N_4/$ZnWO_4$ films	Hydrothermal	UV lamp 12 W	Phenol	—	4 h	$O_2^{\bullet -}$	155
g-C_3N_4/$ZnWO_4$	*In situ* hydrothermal technique	100 W solar simulator	Rhodamine (RhB)	99%	180 min	·OH, h^+	154
$CoWO_4$/g-C_3N_4	Reflux-calcinations method	Sunlight	Ciprofloxacin (CIP)	81%	60 min	$O_2^{\bullet -}$, ·OH	139

a new ternary Z-scheme material by incorporating the nanoparticles of $CoWO_4$ and Fe_3O_4 over g-C_3N_4 by the simple refluxing calcination method. The ternary nanocomposite with 10% g-C_3N_4/Fe_3O_4/$CoWO_4$ degraded almost 100% Rhodamine B in 240 min. The proposed catalyst has high catalytic efficiency, but the time duration is very high to degrade Rhodamine B completely. There is a further need to improve to minimize the time factor.

Longbo J. *et al.*[162] synthesized a new composite material (WO_3/g-C_3N_4/Bi_2O_3) by single-step cocalcination strategy utilizing simple melamine, bismuth(III) nitrate pentahydrate, and tungstic acid as the starting material. The photocatalytic capability of the catalyst against TC increased by up to 80% (Fig. 10(b)). The pore volume, BET surface area, and pore diameter of the catalyst improved by preparing the composite of g-C_3N_4 with WO_3 and Bi_2O_3. To effectively remove these drugs *via* photocatalysis, Nguyen T. *et al.*[163] introduced another ternary Z-scheme dual Cu-$NiWO_4$/g-C_3N_4 heterojunction for the photocatalytic breakdown of *n*-hexane under visible light. The designed catalyst gives better removal and degradation efficiency up to 5 cycles and has a better surface area (84.6 m^2 g^{-1}), which is a sign of the stability of the catalyst, but there is a need to test it for more than five cycles. Y. O. Ibrahim *et al.*[164] synthesized a ternary nanocomposite-based TiO_2/WO_3/g-C_3N_4 photocatalyst to degrade methylene blue as a pollutant under visible light. The photocatalyst TiO_2/WO_3/g-C_3N_4 with 15 wt% g-C_3N_4 displayed the maximum photodegradation action with 91.5% effectiveness. The stability and reusability of the designed catalyst are not good enough, but by seeing this work, the potential photocatalyst can be formed for pollutant degradation under visible light.

M. B. Tahir *et al.*[50] designed a photocatalyst to degrade aspirin and caffeine under visible light. They synthesized WO_3-TiO_2-g-C_3N_4 by a simple hydrothermal process. Tingting Y. *et al.*[165] synthesized a self-sustained catalytic fuel cell system based on anodic TiO_2/g-C_3N_4 heterojunction and cathodic WO_3/W for the oxidation of triclosan or rhodamine B and reduction of NO^{3-}-N to N_2 instantaneously. When these two electrodes are combined, a microscopic current was produced without harvesting light that caused nitrate reduction into N_2 at the cathode. The electrons generated by the system activate the oxygen molecules to generate reactive oxygen species, which cause the oxidation of triclosan and rhodamine B by h^+ in the anode chamber. The electron produced at the anode is transferred to the cathode through an external conducting system where the reduction of nitrates occurs. The designed self-biased system removed almost ~90% RhB and reduced ~95% NO_3–N under UV light after 4 h. Along with the generation of photo--excited electrons ~98%, triclosan was degraded, and ~81% NO^{3-}-N in the cathode chamber was removed in 60 min. The catalytic mechanism of the designed photoelectrochemical and the degradation rate discussed above are shown in Fig. 18(a–c).

Na Lu *et al.*[167] synthesized a Z-scheme photocatalyst for the photodegradation of antibiotic ciprofloxacin, and RGO was used as an electron mediator. They synthesized the photocatalyst g-C_3N_4/RGO/WO_3 by simple self-assembly and photoreduction method. The light-harvesting and charge transfer properties became high with the assimilation of RGO as an electron mediator in place of conductive material within C_3N_4/WO_3. The charge mobility properties were studied using photoluminescence (PL) and electrochemical impedance spectroscopy (EIS), and the photocatalytic degradation efficiency of the synthesized material against ciprofloxacin is still 85%. Yongchao B.[168] synthesized WO_3/RGO/protonated g-C_3N_4 (PCN) composites by the microwave-assisted hydrothermal method for the degradation of tetracycline (TC-HCL). The proposed photocatalyst by this method showed a shorter path of charge migration and a wide interface contact area. The photodegradation efficiency of the 20% WO_3/RGO/PCN composite is maximum. This photocatalyst shows more than 90% catalytic efficiency relative to the previously designed one. By analyzing this work, it is possible to do more work in this field and near future synthesis of a photocatalyst with 100% efficiency, that requires minimum time for the photodegradation of multiple pollutants.

The above discussion highlights the potential of ternary-doped modified WO_3/g-C_3N_4 for advanced photocatalysis. However, it is important to note that the specific scientific advantages may vary depending on the dopant elements, synthesis methods, and intended applications. Ternary photocatalysts typically consist of three different materials, which can increase the complexity of their synthesis, characterization, and application for optimization. Achieving precise control over the composition, morphology, and size of three components in the ternary composite can be challenging, with batch-to-batch variation potentially resulting in low reproducibility. The synthesis of ternary photocatalyst composites can be more demanding than binary or single-component photocatalysts since the longer reaction times and harsher conditions increase energy consumption and create complexity. The synthesis of ternary materials often involves more cost, leading to higher production costs; ternary photocatalysts composite often

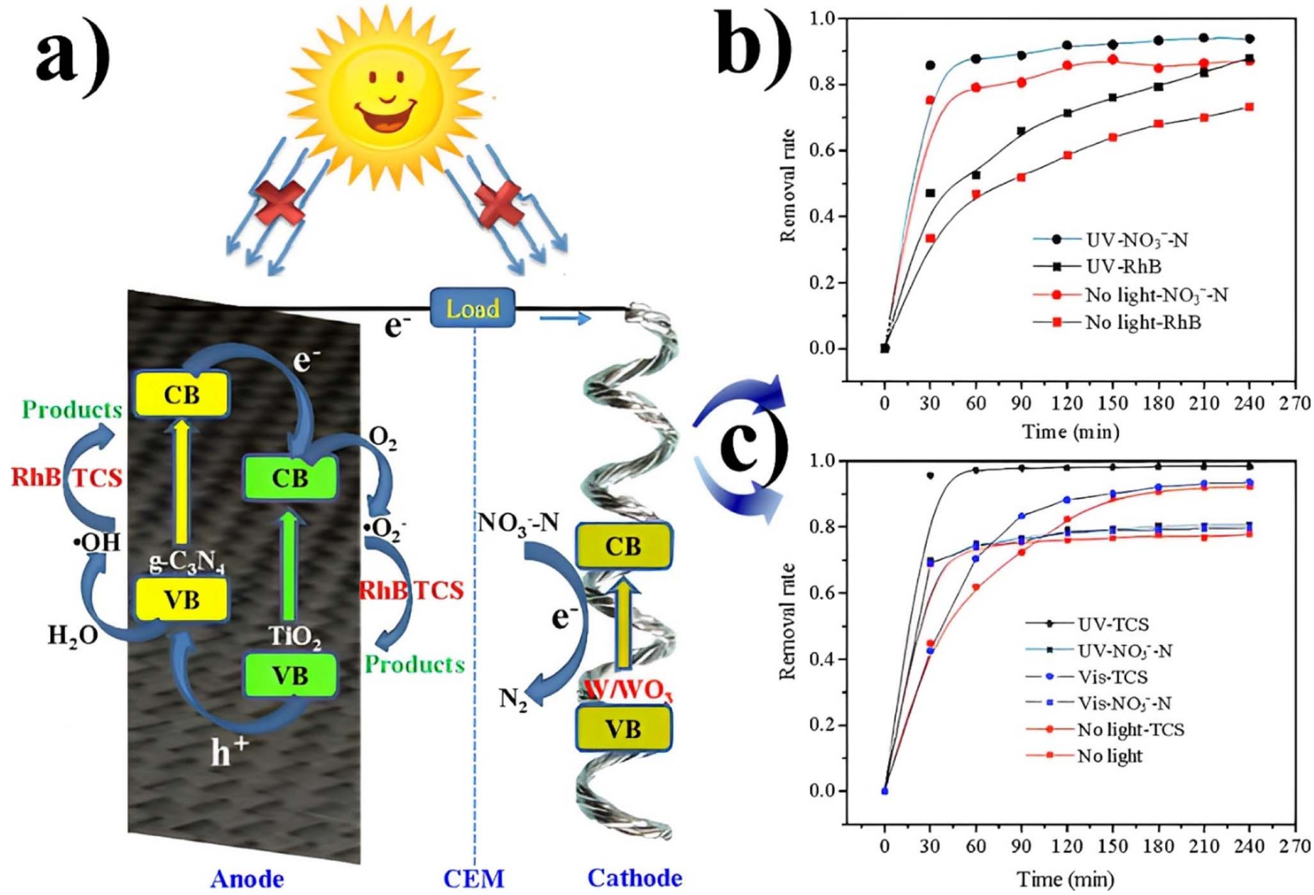

Fig. 18 (a) Degradation mechanism of the self-sustained system. (b) RhB and NO_3^--N degradation rate in anode/cathode chamber and spontaneous current. (c) TCS and NO_3^--N degradation rate in the anode/cathode chamber and spontaneous current (reproduced with permission from ref. 166 Copyright 2017, Elsevier).

involves complex interactions, and their performance may depend on intricate mechanisms. Multiple components in the ternary composite can introduce additional chemical reactions and phase separation, leading to decreased photocatalytic activity.

Nonmetal-doped modified $WO_3/g\text{-}C_3N_4$ composites. At present, modification and variations in the electronic properties of $g\text{-}C_3N_4$ by doping with heteroatom emerge with time. Heteroatom doping typically includes nonmetal element doping. Some favorable changes occur after doping with heteroatoms, such as expanding the crystal cell, broadening the ions transfer path, distributing the crystal cell, and promoting electron transport. In addition, doping with the heteroatom can modify the intrinsic crystal structure, bandgap, crystal structure stability, and affect the charge state. Controllable doping can modify the reaction kinetics with nonmetal atoms. However, well-regulated doping methodologies are crucial for optimized the performance, and further development is needed.

Nonmetal-doped $g\text{-}C_3N_4/WO_3$ materials are environment friendly and utilizing them as dopants can reduce the toxicity of heavy metals, making materials more sustainable and cost-effective. Introducing nonmetal elements into $g\text{-}C_3N_4/WO_3$ can improve the material's resistance to photocorrosion, structural changes, and efficient use in photocatalytic processes. Huinan Che *et al.*[169] synthesized nitrogen-doped graphene quantum dots (NGQDs)-modified Z-scheme $g\text{-}C_3N_4/Bi_2WO_6$ heterojunctions through the hydrothermal method for the photocatalytic degradation of multiple antibiotic drugs such as ciprofloxacin (CIP), tetracycline (TC), and oxytetracycline (OTC) under near-infrared and visible light. Relative to pure $g\text{-}C_3N_4$, Bi_2WO_6, and 60% C_3N_4/Bi_2WO_6, the visible light absorption intensity of 3% NGQDs-60% C_3N_4/Bi_2WO_6 heterojunction increased from 500 nm to 700 nm, suggesting that the incorporation of 3% NGQDs enhanced the photogenerated electron–hole pair production, which results in enhanced photocatalytic activity. The photocatalytic activity of 3% NGQDs–60% C_3N_4/Bi_2WO_6 is higher than that of other pure $g\text{-}C_3N_4$, Bi_2WO_6, and 60% C_3N_4/Bi_2WO_6 photocatalysts. By varying the weight of NGQDs between 1 to 7 wt%, the photocatalytic activity of the photocatalyst against TC increased. A further increase decreased the catalyst's performance, indicating that a high concentration of NGQDs reduced the light absorption capability. NGQDs are more spread over the surface of $g\text{-}C_3N_4/Bi_2WO_6$. The photocatalytic efficiency of 3% NGQDs-60% C_3N_4/Bi_2WO_6 within 60 min against TC was 85.2%, 89.1%, 80.8%, and 75.0%. The photocatalytic performance of the catalyst is lower against other mentioned drugs, only degrading specific pollutants. These catalysts should be designed to degrade multiple drugs under visible and UV light regions within a minimum time and with maximum reusability.

Mi G. *et al.*[170] designed a novel photocatalyst to degrade organic solvent vapors, which are toxic. They fabricated nitrogen-doped carbon quantum dots NCQDs, $g\text{-}C_3N_4$ (CN), and Bi_2WO_6 (BWO) heterostructure (NCQDs/CN/BWO) by a simple sonication method. The TEM and SEM images in Fig. 18(a and b) show that the average size range of 2.5–9.4 nm and lattice distance of NCQDs was 0.320 nm; the corresponding (002) plane of graphitic carbon and the SAED pattern in the SEM image of NCQDs (inset) confirmed the diffraction ring of the (002) crystal plane. NCQDs exhibited a light blue color for suspension when subjected to UV irradiation (Fig. 18(c)). In dark, unmodified, nearly transparent CQDs solution, the color difference between unmodified CQDs and NCQDs is attributed to the absence or presence of N in the CQDs, indicating that the NCQDs sample contained N. Fig. 18(d) shows that the removal efficiency of nUD by NCQDs/CN/BWO-1 was 57.8 (average) ± 0.8%, while that observed for CN/BWO-0.5, NCQDs/BWO, NCQDs/CN, CN, and BWO was 35.6 ± 0.9%, 29.2 ± 0.4%, 26.1 ± 0.3%, 17.6 ± 0.9%, 13.4 ± 1.2%, respectively. The catalytic performance was still good after 5 cycles; however, the performance efficiency was lower. This work established a landmark for designing a more effective photocatalyst to remove these hazardous organic-based vapors from the atmosphere. Jong U. *et al.*[143] synthesized another ternary composite NGQD/FWO/CN material to remove harmful vapors. Firstly, the $FeWO_4/g\text{-}C_3N_4$ heterostructure was synthesized, and then N-doped graphene quantum dots (NGQDs) were decorated on it. The normal elimination efficiency of vaporous ethylbenzene (EBZ) and 2-butoxyethanol (2BE) over a typical NGQD/FWO/CN sample were 97.3% (±0.7%) and 55.1% (±0.6%), as shown in Fig. 19(e and f).

K. M. *et al.*[173] synthesized a porous oxygen-doped-$g\text{-}C_3N_4/WO_3$ photocatalyst for H_2 production. The optimal production of hydrogen was 15 142 $\mu mol\ g^{-1}$, obtained using 10 mg photocatalyst (O-g-CNW-4). However, loading more than 10 mg catalysts reduced the photocatalytic H_2 evaluation. The heteroatom doping of $WO_3/g\text{-}C_3N_4$ set a new site for developing a new photocatalyst for various applications. There is a further need to work in this field to synthesize photocatalysts that can be applied commercially. However, nonmetal doping in photocatalysis can have a few disadvantages, for instance, it may not have the same photocatalytic activity as the metal doping photocatalyst since they can not provide active sites for the desired chemical transformations, thus lowering the photocatalytic efficiency. Nonmetal dopants may decrease the stability of the photocatalytic material by introducing defects in the structure, reducing the material's durability over time and limiting the lifespan of the photocatalyst. Some nonmetals may have narrow absorption ranges, may not effectively utilize the visible light spectrum, and can restrict the photocatalyst's ability.

Limitations of $WO_3/g\text{-}C_3N_4$-based materials

The stability of $WO_3/g\text{-}C_3N_4$ limits its practical applications since some studies reported issues with $WO_3/g\text{-}C_3N_4$ photocorrosion under prolonged irradiation or harsh reaction conditions. Therefore, strategies such as 0D, 1D, 2D, 3D,[122,126,130,174,175] metallic and bimetallic doping, or structural modifications have been explored to enhance the stability of these photocatalysts.[40,43,45,47–51]

The preparation method for the $WO_3/g\text{-}C_3N_4$ can impact the performance efficiency and stability of the photocatalyst.[100] Different synthesis methods (hydrothermal, coprecipitation, calcination, *in situ* synthesis, thermal condensation, acid treatment, *etc.*) have been employed to fabricate the $WO_3/g\text{-}$

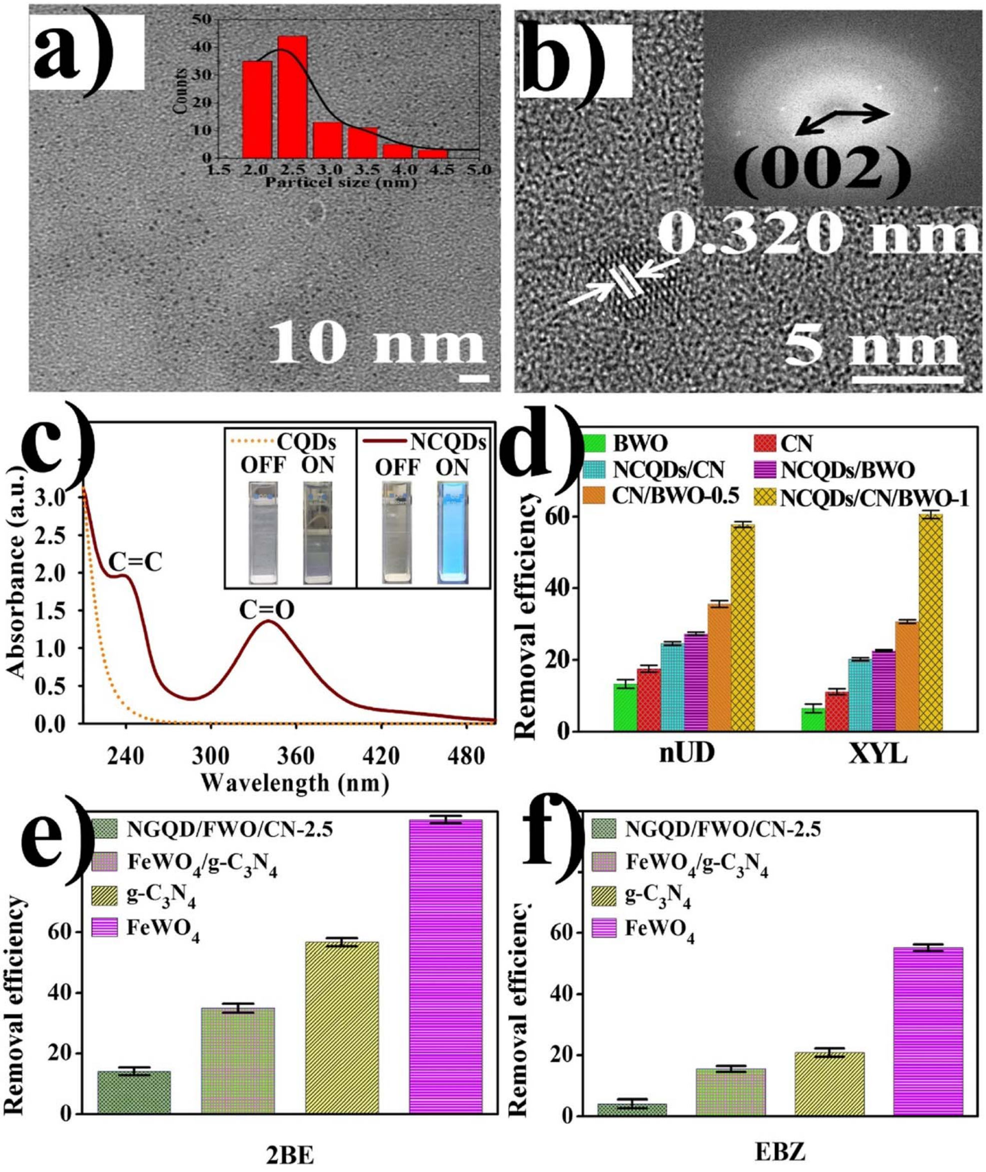

Fig. 19 (a) TEM image and size distribution and (b) HRTEM image with the SAED pattern of NCQDs. (c) UV-Vis spectra of CQDs and NCQDs suspended in deionized water. (d) Average efficiencies ± standard error for *n*UD and *m*XYL removal.[171] (e) Efficiencies of the photocatalytic removal of 2BE and (f) EBZ (reproduced with permission from ref. 172 Copyright 2020, Elsevier).

C_3N_4 composite; however, the optimized synthesis parameters and achieving uniform dispersion can be challenging.[122,126,130,174,175]

The efficiency of WO_3/g-C_3N_4 can vary depending on several factors (morphology, composition, and pH conditions). However, there is still room for improvement to enhance the WO_3/g-C_3N_4 efficiency.[82,176]

Different studies have reported different bandgap values, even for the same doped materials of the WO_3/g-C_3N_4-based nanocomposite.[56,58,59] Advanced spectroscopic characterization can be useful to evaluate the bandgap energy of the doped WO_3/g-C_3N_4 nanocomposite.

A deep understanding of the photoexcited electron–hole separation process is unclear on the WO_3/g-C_3N_4-based nanocomposite. Different advanced characterization techniques should verify it for better understanding.

Efficient recycling and catalyst recovery of WO_3/g-C_3N_4 is an important parameter in practical applications, and some techniques such as filtration, centrifugation, or magnetic separation are used to recover photocatalysts for reuse. After the separation, the catalyst shows less photocatalytic activities. The separation from the system is not fruitful; therefore, further research is needed to develop more effective and scalable methods for photocatalyst separation and recycling. It is a drawback for real applications, which could be resolved with the development of science and technology. More attention should be paid to overcoming the separation and recyclability issue of the WO_3/g-C_3N_4-based nanocomposite.

Future perspectives

The combination of WO_3 and g-C_3N_4 as photocatalysts has significant advances in recent research. Here are some of the most important advancements for WO_3/g-C_3N_4 photocatalysts based on the above data.

• The synergistic effect between WO_3 and g-C_3N_4 has shown improved photocatalytic performance compared to individual components, and this advancement opens avenues for the further optimization and exploration of the WO_3/g-C_3N_4 system.

• Researchers have made progress in understanding the mechanisms behind the improved photocatalytic activity of WO_3/g-C_3N_4. Current research further elucidates the charge separation, transfer processes, and surface reactions contributing to enhanced performance.

• Modifying the band structure of WO_3/g-C_3N_4 through element doping and heterojunction formation offers opportunities to tailor the photocatalytic properties. Future research can explore novel strategies to fine-tune the band structure for specific applications and improved efficiency.

• While significant progress has been made in the laboratory, scaling up the synthesis and application of WO_3/g-C_3N_4 photocatalysts is an important area for future research. Efforts can be directed toward developing scalable synthesis methods and exploring real-world applications.

• In the future, this material can solve global energy challenges and minimize water pollution by providing green and economical cheap materials for designing different modification techniques. This material can be used in water splitting (the process that converts water into hydrogen and oxygen gases). Hydrogen gas can serve as a clean and renewable energy source soon.

• Researchers should apply these materials in environmental studies to remove volatile organic compounds for air purification. This application can improve the air quality in environments. The photocatalytic properties of the WO_3/g-C_3N_4-based nanocomposite make them more effective in volatile organic compounds (VOCs) and nitrogen oxides (NO_x) detection from air. This material can detect bimolecular, toxic gases, and environmental pollutants shortly for designing such sensing devices.

• The surface area of the WO_3/g-C_3N_4-based nanocomposite is small. To enhance the specific surface area of the WO_3/g-C_3N_4-based nanocomposite, further studies should be focused on, such as synthesizing mesoporous WO_3/g-C_3N_4-based nanocomposite using different methods.

• The antimicrobial properties of the WO_3/g-C_3N_4-based nanocomposite can be utilized for developing antibacterial coatings on surfaces, preventing the growth and spread of bacteria and infections, and medical equipment. Drug delivery in the present era is the most popular medical field. Researchers should pay attention to these materials for drug delivery. Further investigations should focus on this application in *in vitro* and *in vivo* studies and living organisms.

• Little data is available on these materials (WO_3/g-C_3N_4) for artificial photosynthesis and nitrogen fixation. Researchers should apply this catalyst in this recent hot field.

• Transition metals are important in nanotechnology since have variable oxidation states. They adsorb on another surface and activate them. Several transition metals are not reported for doping in WO_3/g-C_3N_4-based nanocomposite and need to be further investigated in detail. In addition, s-block and p-block elements can significantly change the properties of WO_3/g-C_3N_4-based nanocomposites.

• Computational approaches for theoretical calculations to evaluate the degradation pathways for understanding the photocatalytic mechanism can also be helpful in WO_3/g-C_3N_4-based materials.

• Similarly, future research work must focus on the development of superconductors. Superconductors are used mostly in levitating trains, engines, generators, highly sensitive optical sensors, detectors of magnetic fields, low-noise amplifiers, transformers, magnetic resonance imaging (MRI), and areas that apply strong magnetic fields. A limited number of publications are available on this material for a superconductor.

Conclusion

In this review, we described the history, crystalline structure, synthesis, precursor, method of fabrication, modification (element-doping and structure modification), characterization, and application of WO_3/g-C_3N_4-based nanocomposite in photocatalysis. It is observed that the pristine g-C_3N_4 and WO_3 show unacceptable efficiency due to their low surface area, insufficient sunlight absorption, and fast recombination of photoinduced electron–hole pairs. Strategies to improve the efficiency of WO_3/g-C_3N_4 highlighted the various synthetic routes such as sol–gel, ultrasonic dispersion, microwave irradiation, precipitation, hydrothermal, pyrolysis method, and calcination methods are discussed. A wide range of composites, including WO_3/g-C_3N_4, modified WO_3/g-C_3N_4, (0D, 1D, 2D, 3D) light metal-doped WO_3/g-C_3N_4, transition metal-doped WO_3/g-C_3N_4, ZnO-WO_3/g-C_3N_4, and TiO_2-WO_3/g-C_3N_4 nanomaterials, are investigated. These modifications provide fascinating properties such as a wide range of visible light responses, good redox ability, suitable bandgap, nontoxicity, environmental friendliness, high physicochemical stability, and thermal stability. A brief overview of the recent advanced publications from 2009 to 2023 is discussed for the photocatalytic degradation of organic pollutants. In future studies, WO_3/g-C_3N_4-based nanocomposites can be applied for the betterment of human beings.

Data availability

All the data is available in the manuscript.

Conflicts of interest

Authors declare no competing interests.

Acknowledgements

There is no funding to report for this article. Authors acknowledge the Higher Education Commission (HEC) of Pakistan for this research.

References

1 P. V. Nidheesh, M. Zhou and M. A. Oturan, An overview on the removal of synthetic dyes from water by electrochemical advanced oxidation processes, *Chemosphere*, 2018, **197**, 210–227.

2 T. Shindhal, *et al.*, A critical review on advances in the practices and perspectives for the treatment of dye industry wastewater, *Bioengineered*, 2021, **12**(1), 70–87.

3 X. Yang, *et al.*, Visible-near-infrared-responsive g-C3N4Hx+ reduced decatungstate with excellent performance for photocatalytic removal of petroleum hydrocarbon, *J. Hazard. Mater.*, 2020, **381**, 120994.

4 P. G. Kougias and I. Angelidaki, Biogas and its opportunities—A review, *Front. Environ. Sci. Eng.*, 2018, **12**, 1–12.

5 Administration, *U.E.I., Annual Energy Outlook 2011: With Projections to 2035*, Government Printing Office, 2011.

6 P. Gao, *et al.*, A critical review on bismuth oxyhalide based photocatalysis for pharmaceutical active compounds degradation: Modifications, reactive sites, and challenges, *J. Hazard. Mater.*, 2021, **412**, 125186.

7 M. M. Moura, *et al.*, Degradation of the mixture of the ketoprofen, meloxicam and tenoxicam drugs using TiO2/metal photocatalysers supported in polystyrene packaging waste, *Water Sci. Technol.*, 2021, **83**(4), 863–876.

8 H. Wang, *et al.*, Visible-light-driven removal of tetracycline antibiotics and reclamation of hydrogen energy from natural water matrices and wastewater by polymeric carbon nitride foam, *Water Res.*, 2018, **144**, 215–225.

9 L. M. Bexfield, *et al.*, Hormones and pharmaceuticals in groundwater used as a source of drinking water across the United States, *Environ. Sci. Technol.*, 2019, **53**(6), 2950–2960.

10 B. P. Gumbi, *et al.*, Detection and quantification of acidic drug residues in South African surface water using gas chromatography-mass spectrometry, *Chemosphere*, 2017, **168**, 1042–1050.

11 Z. Zhao, *et al.*, In Situ Preparation of Mn0. 2Cd0. 8S-Diethylenetriamine/Porous g-C3N4 S-Scheme Heterojunction with Enhanced Photocatalytic Hydrogen Production, *Adv. Sustainable Syst.*, 2023, **7**(1), 2100498.

12 C. J. Ogugbue and T. J. Sawidis, Bioremediation and detoxification of synthetic wastewater containing triarylmethane dyes by Aeromonas hydrophila isolated from industrial effluent, *Biotechnol. Res. Int.*, 2011, **2011**, 967925.

13 P. A. Carneiro, *et al.*, Homogeneous photodegradation of CI Reactive Blue 4 using a photo-Fenton process under artificial and solar irradiation, *Dyes Pigm.*, 2007, **74**(1), 127–132.

14 A. Aziz, *et al.*, Chitosan-zinc sulfide nanoparticles, characterization and their photocatalytic degradation efficiency for azo dyes, *Int. J. Biol. Macromol.*, 2020, **153**, 502–512.

15 S. Khan, *et al.*, Electrochemical sensors based on biomimetic magnetic molecularly imprinted polymer for selective quantification of methyl green in environmental samples, *Mater. Sci. Eng., C*, 2019, **103**, 109825.

16 N. H. Tran, M. Reinhard and K. Y.-H. Gin, Occurrence and fate of emerging contaminants in municipal wastewater treatment plants from different geographical regions-a review, *Water Res.*, 2018, **133**, 182–207.

17 K. He, *et al.*, Advances in nanostructured silicon carbide photocatalysts, *Acta Phys.-Chim. Sin.*, 2022, **38**, 2201021.

18 F. C. Moreira, *et al.*, Electrochemical advanced oxidation processes: a review on their application to synthetic and real wastewaters, *Appl. Catal., B*, 2017, **202**, 217–261.

19 N. Li, *et al.*, Recent Developments in Functional Nanocomposite Photocatalysts for Wastewater Treatment: A Review, *Adv. Sustainable Syst.*, 2022, **6**(7), 2200106.

20 N. Taoufik, *et al.*, Comparative overview of advanced oxidation processes and biological approaches for the removal pharmaceuticals, *J. Environ. Manage.*, 2021, **288**, 112404.

21 K. Ayoub, *et al.*, Application of advanced oxidation processes for TNT removal: a review, *J. Hazard. Mater.*, 2010, **178**(1–3), 10–28.

22 P. K. Pandis, *et al.*, Key points of advanced oxidation processes (AOPs) for wastewater, organic pollutants and pharmaceutical waste treatment: A mini review, *ChemEngineering*, 2022, **6**(1), 8.

23 H. Sun, *et al.*, One-pot thermal polymerization route to prepare N-deficient modified g-C3N4 for the degradation of tetracycline by the synergistic effect of photocatalysis and persulfate-based advanced oxidation process, *Chem. Eng. J.*, 2021, **406**, 126844.

24 D. Zhu and Q. Zhou, Monitoring, and Management, Action and mechanism of semiconductor photocatalysis on degradation of organic pollutants in water treatment: A review, *Environ. Nanotechnol., Monit. Manage.*, 2019, **12**, 100255.

25 R. Dewil, *et al.*, New perspectives for advanced oxidation processes, *J. Environ. Manage.*, 2017, **195**, 93–99.

26 M. H. Mahdi, T. J. Mohammed, and J. A. Al-Najar, Advanced Oxidation Processes (AOPs) for treatment of antibiotics in wastewater: a review, in *IOP Conference Series: Earth and Environmental Science*, IOP Publishing, 2021.

27 C. Comninellis, *et al.*, Advanced oxidation processes for water treatment: advances and trends for R&D, *J. Chem. Technol. Biotechnol.*, 2008, **83**(6), 769–776.

28 S. A. Fast, *et al.*, A critical evaluation of advanced oxidation processes for emerging contaminants removal, *Environ. Processes*, 2017, **4**, 283–302.

29 J. Y. Hwang, *et al.*, Crystal phase-dependent generation of mobile OH radicals on TiO2: Revisiting the photocatalytic oxidation mechanism of anatase and rutile, *Appl. Catal., B*, 2021, **286**, 119905.

30 E. S. Elmolla and M. Chaudhuri, Degradation of amoxicillin, ampicillin and cloxacillin antibiotics in aqueous solution by the UV/ZnO photocatalytic process, *J. Hazard. Mater.*, 2010, **173**(1–3), 445–449.
31 X. Feng, *et al.*, High performance, recoverable Fe3O4ZnO nanoparticles for enhanced photocatalytic degradation of phenol, *Chem. Eng. J.*, 2014, **244**, 327–334.
32 Q. Li, *et al.*, CdS/graphene nanocomposite photocatalysts, *Adv. Energy Mater.*, 2015, **5**(14), 1500010.
33 M. T. Uddin, *et al.*, Nanostructured SnO2–ZnO heterojunction photocatalysts showing enhanced photocatalytic activity for the degradation of organic dyes, *Inorg. Chem.*, 2012, **51**(14), 7764–7773.
34 D. Zhu and Q. Zhou, Action and mechanism of semiconductor photocatalysis on degradation of organic pollutants in water treatment: A review, *Environ. Nanotechnol., Monit. Manage.*, 2019, **12**, 100255.
35 I. Ani, *et al.*, Photocatalytic degradation of pollutants in petroleum refinery wastewater by TiO2-and ZnO-based photocatalysts: recent development, *J. Cleaner Prod.*, 2018, **205**, 930–954.
36 X. Gu, *et al.*, Self-assembly synthesis of S-scheme g-C3N4/Bi8 (CrO4) O11 for photocatalytic degradation of norfloxacin and bisphenol A, *Chin. J. Catal.*, 2022, **43**(10), 2569–2580.
37 J. Jia, *et al.*, Recent advances on g–C3N4–based Z-scheme photocatalysts: Structural design and photocatalytic applications, *Int. J. Hydrogen Energy*, 2023, **48**(1), 196–231.
38 H. Wang, *et al.*, Synthesis and applications of novel graphitic carbon nitride/metal-organic frameworks mesoporous photocatalyst for dyes removal, *Appl. Catal., B*, 2015, **174**, 445–454.
39 T. Song, *et al.*, Preparation, structure and application of g-C3N4/BiOX composite photocatalyst, *Int. J. Hydrogen Energy*, 2021, **46**(2), 1857–1878.
40 Y. Gong, M. Li and Y. J. C. Wang, Carbon nitride in energy conversion and storage: recent advances and future prospects, *ChemSusChem*, 2015, **8**(6), 931–946.
41 K. Vignesh and M. Kang, Facile synthesis, characterization and recyclable photocatalytic activity of Ag2WO4@ g-C3N4, *Mater. Sci. Eng., B*, 2015, **199**, 30–36.
42 Z. Fan, *et al.*, Bridging effect of S–C bond for boosting electron transfer over cubic hollow CoS/g-C3N4 heterojunction toward photocatalytic hydrogen production, *Langmuir*, 2022, **38**(10), 3244–3256.
43 M. Yang, *et al.*, The influence of preparation method on the photocatalytic performance of g-C3N4/WO3 composite photocatalyst, *Ceram. Int.*, 2014, **40**(8), 11963–11969.
44 J. Bai, *et al.*, Integration of 2D layered CdS/WO3 S-scheme heterojunctions and metallic Ti3C2 MXene-based Ohmic junctions for effective photocatalytic H2 generation, *Chin. J. Catal.*, 2022, **43**(2), 359–369.
45 M. G. Peleyeju and E. Viljoen, WO_3-based catalysts for photocatalytic and photoelectrocatalytic removal of organic pollutants from water A review, *J. Water Process Eng.*, 2021, **40**, 101930.
46 H. Wang, *et al.*, Structure–performance correlation guided applications of covalent organic frameworks, *Mater. Today*, 2022, 106–133.
47 V. Alman, *et al.*, Sunlight Assisted improved photocatalytic degradation of rhodamine B using Pd-loaded gC 3 N 4/WO 3 nanocomposite, *Appl. Phys. A: Mater. Sci. Process.*, 2020, **126**(9), 1–9.
48 M. Karimi-Nazarabad, *et al.*, Highly efficient photocatalytic and photoelectrocatalytic activity of solar light driven WO3/g-C3N4 nanocomposite, *Sol. Energy Mater. Sol. Cells*, 2017, **160**, 484–493.
49 C. Wang, *et al.*, BaWO4/g-C3N4 heterostructure with excellent bifunctional photocatalytic performance, *Chem. Eng. J.*, 2020, **385**, 123833.
50 M. B. Tahir, M. Sagir and K. Shahzad, Removal of acetylsalicylate and methyl-theobromine from aqueous environment using nano-photocatalyst WO3-TiO2@ g-C3N4 composite, *J. Hazard. Mater.*, 2019, **363**, 205–213.
51 S. Li, *et al.*, In situ construction of a C 3 N 5 nanosheet/Bi 2 WO 6 nanodot S-scheme heterojunction with enhanced structural defects for the efficient photocatalytic removal of tetracycline and Cr (vi), *Inorg. Chem. Front.*, 2022, **9**(11), 2479–2497.
52 L. Jiang, *et al.*, Doping of graphitic carbon nitride for photocatalysis: A reveiw, *Appl. Catal., B*, 2017, **217**, 388–406.
53 C. Dong, *et al.*, A review on WO3 based gas sensors: Morphology control and enhanced sensing properties, *J. Alloys Compd.*, 2020, **820**, 153194.
54 M. G. Peleyeju and E. L. Viljoen, WO3-based catalysts for photocatalytic and photoelectrocatalytic removal of organic pollutants from water–A review, *J. Water Process. Eng.*, 2021, **40**, 101930.
55 B. S. Kalanoor, H. Seo and S. S. Kalanur, Recent developments in photoelectrochemical water-splitting using WO3/BiVO4 heterojunction photoanode: A review, *Mater. Sci. Energy Technol.*, 2018, **1**(1), 49–62.
56 J. Yao, *et al.*, Improved photocatalytic activity of WO3/C3N4: By constructing an anchoring morphology with a Z-scheme band structure, *Solid State Sci.*, 2019, **95**, 105926.
57 O. Ola, *et al.*, Pseudocapacitive Performance of WO 3/gC 3 N 4 Nanocomposites, in *2021 IEEE 11th International Conference Nanomaterials: Applications & Properties (NAP)*, IEEE, 2021.
58 H. Qian, *et al.*, One-Pot Construction of Porous WO3/g-C3N4 Nanotubes of Photocatalyst for Fast and Boosted Photodegradation of Rhodamine B and Tetracycline, *J. Electron. Mater.*, 2023, 1–16.
59 X. Zhang and S. He, WOx/g-C3N4 layered heterostructures with controlled crystallinity towards superior photocatalytic degradation and H2 generation, *Carbon*, 2020, **156**, 488–498.
60 J. Liebig, *Annalen*, 1834, **10**, 10.
61 E. C. Franklin, The ammono-carbonic acids, *J. Am. Chem. Soc.*, 1922, **44**(3), 486–509.
62 W. K. Darkwah, *et al*, Mini review on the structure and properties (photocatalysis), and preparation techniques of

graphitic carbon nitride nano-based particle, and its applications, *Nanoscale Res. Lett.*, 2018, **13**(1), 1–15.

63 K. Qi, S.-y. Liu and A. Zada, Graphitic carbon nitride, a polymer photocatalyst, *J. Taiwan Inst. Chem. Eng.*, 2020, **109**, 111–123.

64 A. O. Idris, *et al.*, Graphitic carbon nitride: a highly electroactive nanomaterial for environmental and clinical sensing, *Sensors*, 2020, **20**(20), 5743.

65 V. Battula, *et al.*, A true oxygen-linked heptazine based polymer for efficient hydrogen evolution, *Appl. Catal., B*, 2019, **244**, 313–319.

66 A. Wang, *et al.*, Recent advances of graphitic carbon nitride-based structures and applications in catalyst, sensing, imaging, and LEDs, *Nano-Micro Lett.*, 2017, **9**(4), 1–21.

67 M. Y. Chen, D. Li, X. Lin, V. P. Dravid, Y. W. Chung, M. S. Wong and W. D. Sproul, Analytical electron microscopy and Raman spectroscopy studies of carbon nitride thin films, *J. Vac. Sci. Technol., A*, 1993, **11**(3), 521–524.

68 J. L. Corkill and M. L. Cohen, Calculated quasiparticle band gap of β-C_3N_4, *Phys. Rev. B: Condens. Matter Mater. Phys.*, 1993, **48**(23), 17622.

69 M. F. R. Samsudin, N. Bacho, and S. Sufian, Recent development of graphitic carbon nitride-based photocatalyst for environmental pollution remediation, in *Nanocatalysts*, IntechOpen. 2018.

70 D. Wei, *et al.*, In situ construction of interconnected SnO2/nitrogen-doped Carbon@ TiO2 networks for lithium-ion half/full cells, *Electrochim. Acta*, 2018, **290**, 312–321.

71 Q. Hao, *et al.*, Graphitic carbon nitride with different dimensionalities for energy and environmental applications, *Nano Res.*, 2020, **13**(1), 18–37.

72 B. Zhu, *et al.*, First-principle calculation study of tri-s-triazine-based g-C3N4: a review, *Appl. Catal., B*, 2018, **224**, 983–999.

73 W.-J. Ong, *et al.*, Graphitic carbon nitride (g-C3N4)-based photocatalysts for artificial photosynthesis and environmental remediation: are we a step closer to achieving sustainability?, *Chem. Rev.*, 2016, **116**(12), 7159–7329.

74 H.-W. ZUO, *et al.*, Pt4 clusters supported on monolayer graphitic carbon nitride sheets for oxygen adsorption: a first-principles study, *Acta Phys.-Chim. Sin.*, 2016, **32**(5), 1183–1190.

75 B. Zhu, Review on DFT calculation of s-triazine-based carbon nitride, *Carbon Energy*, 2019, **1**(1), 32–56.

76 B. Zhu, *et al.*, First principle investigation of halogen-doped monolayer g-C3N4 photocatalyst, *Appl. Catal., B*, 2017, **207**, 27–34.

77 B. Zhu, *et al.*, First-principle calculation study of tri-s-triazine-based g-C3N4: a review, *Appl. Catal., B*, 2018, **224**, 983–999.

78 J. Kim, *et al.*, Platinized WO3 as an environmental photocatalyst that generates OH radicals under visible light, *Environ. Sci. Technol.*, 2010, **44**(17), 6849–6854.

79 D. Migas, *et al.*, Tungsten oxides. I. Effects of oxygen vacancies and doping on electronic and optical properties of different phases of WO 3, *J. Appl. Phys.*, 2010, **108**(9), 093713.

80 S. S. Kalanur, L. T. Duy and H. Seo, Recent progress in photoelectrochemical water splitting activity of WO3 photoanodes, *Top. Catal.*, 2018, **61**(9), 1043–1076.

81 F. Wang, C. Di Valentin and G. Pacchioni, Electronic and structural properties of WO3: a systematic hybrid DFT study, *J. Phys. Chem. C*, 2011, **115**(16), 8345–8353.

82 J. Fu, *et al.*, Ultrathin 2D/2D WO3/g-C3N4 step-scheme H2-production photocatalyst, *Appl. Catal., B*, 2019, **243**, 556–565.

83 P. Praus, *et al.*, Synthesis and properties of nanocomposites of WO3 and exfoliated g-C3N4, *Ceram. Int.*, 2017, **43**(16), 13581–13591.

84 X. Han, *et al.*, WO3/g-C3N4 two-dimensional composites for visible-light driven photocatalytic hydrogen production, *Int. J. Hydrogen Energy*, 2018, **43**(10), 4845–4855.

85 H. Zhuang, *et al.*, *In situ* construction of WO 3/gC 3 N 4 composite photocatalyst with 2D–2D heterostructure for enhanced visible light photocatalytic performance, *New J. Chem.*, 2019, **43**(44), 17416–17422.

86 T. Pan, *et al.*, Anionic polyacrylamide-assisted construction of thin 2D-2D WO3/g-C3N4 Step-scheme heterojunction for enhanced tetracycline degradation under visible light irradiation, *J. Hazard. Mater.*, 2020, **393**, 122366.

87 J. Chen, *et al.*, Fabrication of hierarchical sheet-on-sheet WO3/g-C3N4 composites with enhanced photocatalytic activity, *J. Alloys Compd.*, 2019, **777**, 325–334.

88 Y. Li, *et al.*, Construction of inorganic–organic 2D/2D WO 3/gC 3 N 4 nanosheet arrays toward efficient photoelectrochemical splitting of natural seawater, *Phys. Chem. Chem. Phys.*, 2016, **18**(15), 10255–10261.

89 C. Cheng, *et al.*, WO3/g-C3N4 composites: one-pot preparation and enhanced photocatalytic H2 production under visible-light irradiation, *Nanotechnology*, 2017, **28**(16), 164002.

90 T. Xiao, *et al.*, In situ construction of hierarchical WO3/g-C3N4 composite hollow microspheres as a Z-scheme photocatalyst for the degradation of antibiotics, *Appl. Catal., B*, 2018, **220**, 417–428.

91 M.-H. Pham, *et al.*, Visible light induced hydrogen generation using a hollow photocatalyst with two cocatalysts separated on two surface sides, *Phys. Chem. Chem. Phys.*, 2014, **16**(13), 5937–5941.

92 J. Yuan, *et al.*, TiO2/SnO2 double-shelled hollow spheres-highly efficient photocatalyst for the degradation of rhodamine B, *Catal. Commun.*, 2015, **60**, 129–133.

93 S. L. Prabavathi, *et al.*, Construction of heterostructure CoWO4/g-C3N4 nanocomposite as an efficient visible-light photocatalyst for norfloxacin degradation, *J. Ind. Eng. Chem.*, 2019, **80**, 558–567.

94 X. Xing, *et al.*, CoWO4 nanoparticles prepared by two methods displaying different structures and supercapacitive performances, *Electrochim. Acta*, 2015, **157**, 15–22.

95 K. Liu, *et al.*, Synthesis of direct Z-scheme MnWO4/g-C3N4 photocatalyst with enhanced visible light photocatalytic activity, *Nano*, 2017, **12**(10), 1750129.

96 J. Low, *et al.*, A review of direct Z-scheme photocatalysts, *Small Methods*, 2017, **1**(5), 1700080.

97 R. Dadigala, *et al.*, Construction of *in situ* self-assembled FeWO 4/gC 3 N 4 nanosheet heterostructured Z-scheme photocatalysts for enhanced photocatalytic degradation of rhodamine B and tetracycline, *Nanoscale Adv.*, 2019, **1**(1), 322–333.

98 X. Zhang, X. Zhang and P. Yang, Transition metals decorated g-C3N4/N-doped carbon nanotube catalysts for water splitting: A review, *J. Electroanal. Chem.*, 2021, **895**, 115510.

99 H. Jiang, *et al.*, Recent advances in heteroatom doped graphitic carbon nitride (g-C3N4) and g-C3N4/metal oxide composite photocatalysts, *Curr. Org. Chem.*, 2020, **24**(6), 673–693.

100 M. W. Kadi and R. M. Mohamed, Increasing visible light water splitting efficiency through synthesis route and charge separation in measoporous g-C3N4 decorated with WO3 nanoparticles, *Ceram. Int.*, 2019, **45**(3), 3886–3893.

101 L. Huang, *et al.*, Visible-light-induced WO 3/gC 3 N 4 composites with enhanced photocatalytic activity, *Dalton Trans.*, 2013, **42**(24), 8606–8616.

102 W. Yang, *et al.*, Hierarchical NiCo 2 O 4@ NiO core–shell hetero-structured nanowire arrays on carbon cloth for a high-performance flexible all-solid-state electrochemical capacitor, *J. Mater. Chem. A*, 2014, **2**(5), 1448–1457.

103 L. Huang, *et al.*, Visible-light-induced WO 3/gC 3 N 4 composites with enhanced photocatalytic activity, *Dalton Trans.*, 2013, **42**(24), 8606–8616.

104 S. Chen, *et al.*, Study on the separation mechanisms of photogenerated electrons and holes for composite photocatalysts g-C3N4-WO3, *Appl. Catal., B*, 2014, **150**, 564–573.

105 A. T. Doan, *et al.*, Graphitic gC 3 N 4-WO 3 composite: synthesis and photocatalytic properties, *Bull. Korean Chem. Soc.*, 2014, **35**(6), 1794–1798.

106 H. Zhang, *et al.*, Photocatalytic selective oxidation of biomass-derived 5-hydroxymethylfurfural to 2, 5-diformylfuran on WO3/g-C3N4 composite under irradiation of visible light, *J. Photochem. Photobiol., A*, 2019, **371**, 1–9.

107 H. Yan, *et al.*, Single-source-precursor-assisted synthesis of porous WO3/g-C3N4 with enhanced photocatalytic property, *Colloids Surf., A*, 2019, **582**, 123857.

108 F. Chang, *et al.*, Binary composites WO3/g-C3N4 in porous morphology: Facile construction, characterization, and reinforced visible light photocatalytic activity, *Colloids Surf., A*, 2019, **563**, 11–21.

109 R. Ma, Preparation of highly dispersed WO_3/few layer g-C_3N_4 and its enhancement of catalytic oxidative desulfurization activity, *Colloids Surf., A*, 2019, **572**, 250–258.

110 A. Priya, *et al.*, A study of photocatalytic and photoelectrochemical activity of as-synthesized WO3/g-C3N4 composite photocatalysts for AO7 degradation, *Mater. Sci. Energy Technol.*, 2020, **3**, 43–50.

111 R. Zhao, *et al.*, Preparation of WO3/g-C3N4 composites and their application in oxidative desulfurization, *Appl. Surf. Sci.*, 2017, **392**, 810–816.

112 A. Navarro-Aguilar, *et al.*, An efficient and stable WO3/g-C3N4 photocatalyst for ciprofloxacin and orange G degradation, *J. Photochem. Photobiol., A*, 2019, **384**, 112010.

113 I. Aslam, *et al.*, The synergistic effect between WO 3 and gC 3 N 4 towards efficient visible-light-driven photocatalytic performance, *New J. Chem.*, 2014, **38**(11), 5462–5469.

114 H. Katsumata, *et al.*, Z-scheme photocatalytic hydrogen production over WO 3/gC 3 N 4 composite photocatalysts, *RSC Adv.*, 2014, **4**(41), 21405–21409.

115 M. Gondal, *et al.*, Preparation of WO 3/gC 3 N 4 composites and their enhanced photodegradation of contaminants in aqueous solution under visible light irradiation, *React. Kinet., Mech. Catal.*, 2015, **114**(1), 357–367.

116 S. Chen, *et al.*, Study on the separation mechanisms of photogenerated electrons and holes for composite photocatalysts g-C3N4-WO3, *Appl. Catal., B*, 2014, **150**, 564–573.

117 K.-i. Katsumata, *et al.*, Preparation of graphitic carbon nitride (g-C3N4)/WO3 composites and enhanced visible-light-driven photodegradation of acetaldehyde gas, *J. Hazard. Mater.*, 2013, **260**, 475–482.

118 Y. Zang, *et al.*, Facile synthesis of composite g-C 3 N 4/WO 3: a nontoxic photocatalyst with excellent catalytic activity under visible light, *RSC Adv.*, 2013, **3**(33), 13646–13650.

119 J. Singh, *et al.*, Synthesis of coral like WO3/g-C3N4 nanocomposites for the removal of hazardous dyes under visible light, *J. Alloys Compd.*, 2019, **808**, 151734.

120 J. Singh, A. Arora and S. Basu, Synthesis of coral like WO3/g-C3N4 nanocomposites for the removal of hazardous dyes under visible light, *J. Alloys Compd.*, 2019, **808**, 151734.

121 Z. Lou and C. J. C. Xue, In situ growth of WO 3− x nanowires on gC 3 N 4 nanosheets: 1D/2D heterostructures with enhanced photocatalytic activity, *CrystEngComm*, 2016, **18**(43), 8406–8410.

122 T. Pan, *et al.*, Anionic polyacrylamide-assisted construction of thin 2D-2D WO3/g-C3N4 Step-scheme heterojunction for enhanced tetracycline degradation under visible light irradiation, *J. Hazard. Mater.*, 2020, **393**, 122366.

123 F. Zhang, *et al.*, One-step oxygen vacancy engineering of WO3-x/2D g-C3N4 heterostructure: Triple effects for sustaining photoactivity, *J. Alloys Compd.*, 2019, **795**, 426–435.

124 M. Antoniadou, *et al.*, Bifunctional g-C3N4/WO3 thin films for photocatalytic water purification, *Water*, 2019, **11**(12), 2439.

125 C. Xu, *et al.*, Facile construction of leaf-like WO 3 nanoflakes decorated on gC 3 N 4 towards efficient oxidation of alcohols under mild conditions, *New J. Chem.*, 2018, **42**(20), 16523–16532.

126 T. Xiao, *et al.*, In situ construction of hierarchical WO3/g-C3N4 composite hollow microspheres as a Z-scheme

photocatalyst for the degradation of antibiotics, *Appl. Catal., B*, 2018, **220**, 417–428.

127 F. Xu, *et al.*, Step-by-step mechanism insights into the TiO2/Ce2S3 S-scheme photocatalyst for enhanced aniline production with water as a proton source, *ACS Catal.*, 2021, **12**(1), 164–172.

128 W. Wang, *et al.*, Efficient degradation of tetracycline *via* coupling of photocatalysis and photo-fenton processes over a 2D/2D α-Fe2O3/g-C3N4 S-scheme heterojunction catalyst, *Acta Phys.-Chim. Sin.*, 2022, **38**(7), 2201008.

129 S. Deng, *et al.*, WO 3 nanosheets/gC 3 N 4 nanosheets' nanocomposite as an effective photocatalyst for degradation of rhodamine B, *Appl. Phys. A: Mater. Sci. Process.*, 2019, **125**(1), 44.

130 J. Chen, *et al.*, Fabrication of hierarchical sheet-on-sheet WO3/g-C3N4 composites with enhanced photocatalytic activity, *J. Alloys Compd.*, 2019, **777**, 325–334.

131 J. Chen, *et al.*, Ag nanoparticles decorated WO3/g-C3N4 2D/2D heterostructure with enhanced photocatalytic activity for organic pollutants degradation, *Appl. Surf. Sci.*, 2019, **467**, 1000–1010.

132 S. M. Hashmi, *et al.*, Enhancement of mechanical properties of epoxy/halloysite nanotube (HNT) nanocomposites, *SN Appl. Sci.*, 2019, **1**(4), 296.

133 Y. Li, *et al.*, In situ loading of Ag2WO4 on ultrathin g-C3N4 nanosheets with highly enhanced photocatalytic performance, *J. Hazard. Mater.*, 2016, **313**, 219–228.

134 J. Huang, *et al.*, Ultrathin Ag2WO4-coated P-doped g-C3N4 nanosheets with remarkable photocatalytic performance for indomethacin degradation, *J. Hazard. Mater.*, 2020, **392**, 122355.

135 N. Tian, H. Huang and Y. Zhang, Mixed-calcination synthesis of CdWO4/g-C3N4 heterojunction with enhanced visible-light-driven photocatalytic activity, *Appl. Surf. Sci.*, 2015, **358**, 343–349.

136 A. Maavia, *et al.*, Facile synthesis of g-C3N4/CdWO4 with excellent photocatalytic performance for the degradation of Minocycline, *Mater. Sci. Energy Technol.*, 2019, **2**(2), 258–266.

137 P. Xing, *et al.*, Preparation of CoWO4/g-C3N4 and its Ultra-Deep Desulfurization Property, *Aust. J. Chem.*, 2016, **70**(3), 271–279.

138 S. L. Prabavathi, *et al.*, Construction of heterostructure CoWO4/g-C3N4 nanocomposite as an efficient visible-light photocatalyst for norfloxacin degradation, *J. Ind. Eng. Chem.*, 2019, **80**, 558–567.

139 S. Sahoo, *et al.*, Facile construction of CoWO4 modified g-C3N4 nanocomposites with enhanced photocatalytic activity under visible light irradiation, *Mater. Today: Proc.*, 2021, **35**, 193–197.

140 D. P. Ojha, *et al.*, Decoration of g-C3N4 with hydrothermally synthesized FeWO4 nanorods as the high-performance supercapacitors, *Chem. Phys. Lett.*, 2018, **712**, 83–88.

141 R. Dadigala, *et al.*, Construction of *in situ* self-assembled FeWO 4/gC 3 N 4 nanosheet heterostructured Z-scheme photocatalysts for enhanced photocatalytic degradation of rhodamine B and tetracycline, *Nanoscale Adv.*, 2019, **1**(1), 322–333.

142 A. Rashidizadeh, *et al.*, Graphitic Carbon Nitride Nanosheet/FeWO4 Nanoparticle Composite for Tandem Photooxidation/Knoevenagel Condensation, *ACS Appl. Nano Mater.*, 2020, **3**(7), 7057–7065.

143 J. U. Choi and W.-K. Jo, FeWO4/g-C3N4 heterostructures decorated with N-doped graphene quantum dots prepared under various sonication conditions for efficient removal of noxious vapors, *Ceram. Int.*, 2020, **46**(8), 11346–11356.

144 R. Bhosale, *et al.*, Direct Z-scheme g-C3N4/FeWO4 nanocomposite for enhanced and selective photocatalytic CO2 reduction under visible light, *ACS Appl. Mater. Interfaces*, 2019, **11**(6), 6174–6183.

145 L. Zhang, *et al.*, In situ growth of g-C3N4 on hexangular flowerlike FeWO4 microcrystals: highly efficient catalyst and the crucial roles of Fe3+/Fe2+ couple in the photoassisted oxidation and reduction reactions, *J. Phys. Chem. C*, 2018, **122**(24), 12900–12912.

146 R. Huang, *et al.*, In situ synthesis of Cu+ self-doped CuWO4/g-C3N4 heterogeneous Fenton-like catalysts: the key role of Cu+ in enhancing catalytic performance, *Sep. Purif. Technol.*, 2020, **250**, 117174.

147 S. Zhou, *et al.*, Enhanced visible light photocatalytic degradation of rhodamine B by Z-scheme CuWO 4/gC 3 N 4 heterojunction, *J. Mater. Sci.: Mater. Electron.*, 2021, **32**(3), 2731–2743.

148 K. Liu, *et al.*, Synthesis of direct Z-scheme MnWO4/g-C3N4 photocatalyst with enhanced visible light photocatalytic activity, *Nano*, 2017, **12**(10), 1750129.

149 K. Saravanakumar, *et al.*, 1D/2D MnWO4 nanorods anchored on g-C3N4 nanosheets for enhanced photocatalytic degradation ofloxacin under visible light irradiation, *Colloids Surf., A*, 2019, **581**, 123845.

150 V. Rathi, A. Panneerselvam and R. J. Sathiyapriya, Surface decoration of MnWO 4 nanoparticles with gC 3 N 4 nanosheets to build hetero-structure and its structural, optical and enhanced visible light photocatalytic activity, *J. Mater. Sci.: Mater. Electron.*, 2020, **31**(17), 14823–14837.

151 V. J. C. Muthuraj, *et al*, Superior visible light driven photocatalytic degradation of fluoroquinolone drug norfloxacin over novel NiWO4 nanorods anchored on g-C3N4 nanosheets, *Colloids Surf., A*, 2019, **567**, 43–54.

152 V. Muthuraj, Superior visible light driven photocatalytic degradation of fluoroquinolone drug norfloxacin over novel NiWO4 nanorods anchored on g-C3N4 nanosheets, *Colloids Surf., A*, 2019, **567**, 43–54.

153 V.-D. Dao, *et al.*, Superior visible light photocatalytic activity of g-C3N4/NiWO4 direct Z system for degradation of gaseous toluene, *J. Solid State Chem.*, 2019, **272**, 62–68.

154 R. Koutavarapu, *et al.*, A novel one-pot approach of ZnWO 4 nanorods decorated onto gC 3 N 4 nanosheets: 1D/2D heterojunction for enhanced solar-light-driven photocatalytic activity, *J. Mater. Sci.*, 2020, **55**(3), 1170–1183.

155 S. Zhan, *et al.*, g-C3N4/ZnWO4 films: preparation and its enhanced photocatalytic decomposition of phenol in UV, *Appl. Surf. Sci.*, 2015, **358**, 328–335.

156 Z. Bian, *et al.*, Plant uptake-assisted round-the-clock photocatalysis for complete purification of aquaculture wastewater using sunlight, *Environ. Sci. Technol.*, 2015, **49**(4), 2418–2424.

157 J. Zheng and L. J. C. E. J. Zhang, Designing 3D magnetic peony flower-like cobalt oxides/g-C3N4 dual Z-scheme photocatalyst for remarkably enhanced sunlight driven photocatalytic redox activity, *Chem. Eng. J.*, 2019, **369**, 947–956.

158 M. Tang, Facile synthesis of dual Z-scheme g-C_3N_4/Ag_3PO_4/AgI composite photocatalysts with enhanced performance for the degradation of a typical neonicotinoid pesticide, *Appl. Catal., B*, 2020, **268**, 118395.

159 M. Tang, *et al.*, Rationally constructing of a novel dual Z-scheme composite photocatalyst with significantly enhanced performance for neonicotinoid degradation under visible light irradiation, *Appl. Catal., B*, 2020, **270**, 118918.

160 Y. Guo, *et al.*, Mediator-free direct dual-Z-scheme Bi2S3/BiVO4/MgIn2S4 composite photocatalysts with enhanced visible-light-driven performance towards carbamazepine degradation, *Appl. Catal., B*, 2019, **254**, 479–490.

161 H. Yin, *et al.*, Construction of AgBr/β-Ag2WO4/g-C3N4 ternary composites with dual Z-scheme band alignment for efficient organic pollutants removal, *Sep. Purif. Technol.*, 2021, **272**, 118251.

162 L. Jiang, *et al.*, In-situ synthesis of direct solid-state dual Z-scheme WO3/g-C3N4/Bi2O3 photocatalyst for the degradation of refractory pollutant, *Appl. Catal., B*, 2018, **227**, 376–385.

163 N. T. T. Truc, *et al.*, Superior activity of Cu-NiWO4/g-C3N4 Z direct system for photocatalytic decomposition of VOCs in aerosol under visible light, *J. Alloys Compd.*, 2019, **798**, 12–18.

164 Y. O. Ibrahim and M. Gondal, Visible-light-driven photocatalytic performance of a Z-scheme based TiO2/WO3/g-C3N4 ternary heterojunctions, *Mol. Catal.*, 2021, **505**, 111494.

165 T. Yu, L. Liu and F. Yang, Heterojunction between anodic TiO2/g-C3N4 and cathodic WO3/W nano-catalysts for coupled pollutant removal in a self-biased system, *Chin. J. Catal.*, 2017, **38**(2), 270–277.

166 T. Yu, L. Liu and F. Yang, Heterojunction between anodic TiO2/g-C3N4 and cathodic WO3/W nano-catalysts for coupled pollutant removal in a self-biased system, *Chin. J. Catal.*, 2017, **38**(2), 270–277.

167 N. Lu, *et al.*, Construction of Z-Scheme g-C3N4/RGO/WO3 with *in situ* photoreduced graphene oxide as electron mediator for efficient photocatalytic degradation of ciprofloxacin, *Chemosphere*, 2019, **215**, 444–453.

168 Y. Bao, *et al.*, Heterostructured WO3/RGO/protonated g-C3N4 three-layer nanosheets for enhanced visible-light photocatalytic activity, *Appl. Surf. Sci.*, 2019, **496**, 143639.

169 H. Che, *et al.*, NGQD active sites as effective collectors of charge carriers for improving the photocatalytic performance of Z-scheme gC 3 N 4/Bi 2 WO 6 heterojunctions, *Catal. Sci. Technol.*, 2018, **8**(2), 622–631.

170 M. G. Kim and W.-K. Jo, Visible-light-activated N-doped CQDs/g-C3N4/Bi2WO6 nanocomposites with different component arrangements for the promoted degradation of hazardous vapors, *J. Mater. Sci. Technol.*, 2020, **40**, 168–175.

171 M. G. Kim and W.-K. Jo, Visible-light-activated N-doped CQDs/g-C3N4/Bi2WO6 nanocomposites with different component arrangements for the promoted degradation of hazardous vapors, *J. Mater. Sci. Technol.*, 2020, **40**, 168–175.

172 J. U. Choi and W.-K. Jo, FeWO4/g-C3N4 heterostructures decorated with N-doped graphene quantum dots prepared under various sonication conditions for efficient removal of noxious vapors, *Ceram. Int.*, 2020, **46**(8), 11346–11356.

173 K. Mallikarjuna, *et al.*, Synthesis of oxygen-doped-g-C3N4/WO3 porous structures for visible driven photocatalytic H2 production, *Phys. E*, 2021, **126**, 114428.

174 C. Cheng, *et al.*, WO3/g-C3N4 composites: one-pot preparation and enhanced photocatalytic H2 production under visible-light irradiation, *Nanotechnology*, 2017, **28**(16), 164002.

175 Y. Li, *et al.*, Construction of inorganic–organic 2D/2D WO 3/gC 3 N 4 nanosheet arrays toward efficient photoelectrochemical splitting of natural seawater, *Phys. Chem. Chem. Phys.*, 2016, **18**(15), 10255–10261.

176 B.-C. CHEN, *et al.*, Research progress on g-C3N4-based Z-scheme photocatalytic system, *Acta Phys.-Chim. Sin.*, 2016, **32**(6), 1371–1382.